Title
Inelastic X-ray Scattering Measurements of Ionization in Warm, Dense Matter

Author
Davis, Paul

Publication Date
2012

Peer reviewed|Thesis/dissertation

Inelastic X-ray Scattering Measurements of Ionization in Warm, Dense Matter

by

Paul F. Davis

A dissertation submitted in partial satisfaction of the
requirements for the degree of
Doctor of Philosophy

in

Applied Science and Technology

in the

Graduate Division

of the

University of California, Berkeley

Committee in charge:

Professor Roger W. Falcone, Chair
Professor Raymond Jeanloz
Professor David T. Attwood

Fall 2012

Inelastic X-ray Scattering Measurements of Ionization in Warm, Dense Matter

Abstract

Inelastic X-ray Scattering Measurements of Ionization in Warm, Dense Matter

by

Paul F. Davis

Doctor of Philosophy in Applied Science and Technology

University of California, Berkeley

Professor Roger W. Falcone, Chair

In this work we demonstrate spectrally resolved x-ray scattering from electron-plasma waves in shock-compressed deuterium and proton-heated matter. Because the spectral signature of inelastic x-ray scattering is strongly dependent on the free electron density of the system, it is used to infer ionization in dynamically heated samples. Using 2-6 ns, 500 J laser pulses from LLNL's Janus laser, we shocked liquid deuterium to pressures approaching 50 GPa, reaching compressions of 4 times liquid density. A second laser produced intense 2 keV x-rays. By collecting and spectrally dispersing forward scattered photons at 45°, the onset of ionization was detected at compressions of about 3 times in the form of plasmon oscillations. Backscattered x-rays bolstered this observation by measuring the free electron distribution through Compton scattering. Comparison with simulations shows very close agreement between the pressure dependence of ionization and molecular dissociation in dynamically compressed deuterium.

In a second set of experiments, a 10 ps, 200 J Titan laser pulse was split into two beams. One created a stream of MeV protons to heat samples of boron and boron-nitride and the other pumped 4.5 keV K-α radiation in a titanium foil to probe the hot target. We observed scattered x-rays 300 ps after heating, noting a strong difference in average ionization between the two target materials at temperatures of 16 eV and very similar mass densities. Comparison with electron structure calculations suggests that this difference is due to a persistence of long-range ion structure in BN resulting in high-temperature band structure.

These results underscore the importance of understanding the complex electron structure of materials even at electron-volt temperatures and gigapascal pressures. Our results provide new data to guide the theoretical modeling of warm, dense matter important to understanding giant planets and inertial fusion targets.

To Anne

and

To My Parents

Contents

List of Figures

List of Tables

Acknowledgments

I'm happy to acknowledge the support of the Stockpile Stewardship Graduate Fellowship and its excellent administrator Lucille Kilmer, who made the PhD funding process as painless as I imagine is possible. At Berkeley, Pat Berumen in the AS&T office did the same for the University's bureaucratic maze. Thanks to the Jupiter Laser Facility technical staff and target fabrication team for keeping the experiments running, often under less than perfect circumstances. Walt Unites deserves special appreciation for his deep experience engineering cryogenic target platforms, as well as his patient late-night explanations of them to an amateur.

I'm very grateful to all of the group members that contributed to one or both of these studies. I especially owe a big debt to Tilo Döppner and Sebastien LePape at LLNL for their advice and long lab hours working on the experiments presented in Chapters 4 and 5 respectively; their contributions to my multilingual cursing abilities will go unacknowledged. Many thanks to Laurent Divol, Carsten Fortmann, Brian Wilson and the Redmer group for theoretical and computational support. Particular thanks to Mike Desjarlais at Sandia not only for running QMD calculations for me but teaching me the basics of the process during my SSGF practicum there.

I have deep appreciation for Siegfried Glenzer's scientific insight, support and motivation, which was instrumental to every step of the process; he has been responsible for much of my development as a professional scientist since my undergraduate days. My Berkeley advisor Roger Falcone has been a consistent and seemingly effortless source of wisdom and guidance throughout. I suspect I will continue to ask him for favors and advice long after I've left the group.

Finally, thanks to my family. Meeting my wife Anne halfway through grad school probably added a year to the process, but the time could not have been better spent. Thank you for your constant support, encouragement and general disinterest in physics. My parents, who made my education possible in big ways and small, are as responsible for any of my success as I am. *Deo gratias.*

Chapter 1

Introduction

1.1 Warm, dense matter

The quest to achieve controlled thermonuclear fusion has led to the development of laser systems of unprecedented energy and intensity, making it possible to create material conditions previously unavailable in the laboratory. It has simultaneously made an understanding of the detailed behavior of matter in these regimes highly important. In particular, while the fields of plasma physics and condensed matter physics are well established, there is a large parameter space between them that has received much less attention. This regime, often labeled warm, dense matter (WDM) [1], shares some of the characteristics of each of its neighbors. Its mass density is approximately solid density and its temperature on the order of an eV. Therefore, it is generally characterized by thermal energies of the same order as the Fermi energy so it contains a hot, partially degenerate electron system. Often quite structurally disordered, it possesses temperatures sufficiently high that they cannot be treated as a perturbation to a ground state, as is often the case in solid-state physics. However, unlike traditional plasma physics, it possesses very strong interparticle forces, and thus likewise cannot be treated with statistical or fluid theories of hot plasma physics.

As illustrated in Figure 1.1, fuel capsules in inertial fusion traverse directly through the (ρ, T) region of WDM, making an understanding of its equation of state, optical and transport properties crucial to fusion design. Further, as illustrated, stellar matter and the cores of giant planets are also composed of WDM; indeed, laboratory experiments are critical to understanding the structure of planets like Jupiter [2]. On a more fundamental level, time resolved studies of these highly excited states of matter

illuminate the important problems of the dynamics of phase transitions and energy relaxation.

Unfortunately, this regime presents unique experimental challenges. Reaching the temperatures and densities of interest necessitates dynamic heating, limiting measurement integration times to less than a microsecond. Combined with the energetic photons and particles that are a byproduct of dynamic heating, reaching robust signal-to-noise ratios is a challenge. Also, unlike many high temperature and under-dense plasmas, WDM is opaque to visible light, limiting optical observations to surface measurements. This has motivated the development of x-ray diagnostics that can directly probe the electron and ion structure of these systems [3].

1.2 X-ray Thomson scattering

The use of spectrally resolved x-ray scattering dates at least as far back as 1929, when Compton scattering - an effect itself first observed a few years earlier [4] - was used to verify that electrons in solids obey Fermi statistics [5]. Inelastic x-ray scattering has become highly sophisticated in the intervening century and is now a regular tool for investigating a wide variety of phenomena in chemical and condensed matter physics (see [6] for a comprehensive overview).

Because of the inherent limitation of the small Thomson cross section, these experiments rely on long integration times at synchrotron sources to reach sufficient signal-to-noise ratios, performing data scans on the order of minutes or hours long. To put the scale in context, the Raleigh scattering cross-section from a single atom by a 2 keV photon by a single atom is about two orders of magnitude higher than the inelastic cross section that carries much of the interesting spectral information. The dominant photon interaction, two orders of magnitude higher still, is x-ray photoionization [7]. Thus, measuring inelastic scattering is searching for a dim signal amid many stronger ones. Synchrotron x-ray sources, generally optimized for high brightness and integrated measurements, provide less than 10^{10} photons in a single pulse a few tens of picoseconds long - not quite sufficient to measure scattering from short-lived dense plasma samples.

It was not until about a decade ago that it was demonstrated that high-energy laser pulses could generate x-rays bright enough to perform similar measurements on the nanosecond time scale [12], making them possible in dynamically heated targets. Such a laser plasma x-ray source, created by irradiating a solid target with sufficient

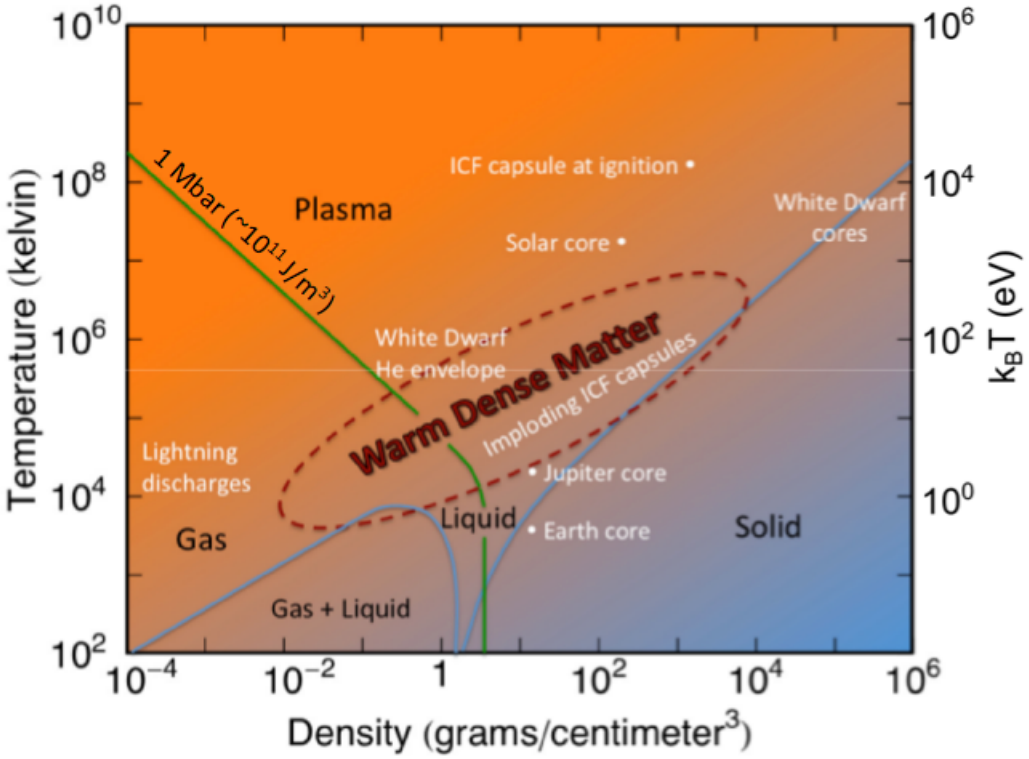

Figure 1.1: The warm, dense regime lies between high temperature plasmas and condensed solids and liquids. Not only does inertially confined fusion fuel traverse this space during compression but astrophysical bodies like planetary cores and white dwarfs are partially composed of WDM. Image from [9].

energy to generate atomic emission, can convert a fraction of a percentage of laser energy into a specific atomic line. By placing this source millimeters from a plasma target and using a kilo-joule class laser, 10^{12} photons of a few keV can be scattered from a sample, enough for scattering to be measured above the background created by the heating process. While these thermal sources have nanosecond lifetimes, they are short enough to measure hydrodynamic phenomena occurring on the same timescale, particularly when paired with gated x-ray detectors.

This development led to a series of X-ray Thomson Scattering (XRTS) experiments demonstrating the viability of Compton scattering [10] and scattering from plasmon oscillations [13] in targets shocked by the Omega laser. These were followed by demonstrations of scattering on shocked targets at the Titan laser using picosecond long K-α x-ray sources produced with short-pulse lasers. The temporal resolution of these probes made it possible to test dense matter models of equation of state and electron correlation [14, 15].

Building on these successes, the goal of this dissertation is to use the XRTS technique to study two applications of great current interest in the WDM regime. Because of its central important in fusion and planetary science, hydrogen has been a canonical system to experimentalists and theoreticians studying warm, dense matter. Unfortunately, owing of its low density it is a poor x-ray scatterer. The experimental complications of cryogenic cooling and complex targets make it even more difficult to work with in the lab. The first goal of this dissertation is to demonstrate the viability of x-ray scattering as a probe of shocked hydrogen. By measuring its ionization as it is compressed, we add an important new constraint on theoretical models of high pressure hydrogen.

The second goal is to demonstrate the feasibility of the diagnostic at the high temperature limit of the WDM regime. Proton-heating has become a key subject of interest in high-energy-density physics. However, because of the extreme noise involved with particle production, the only x-ray scattering measurements to date have been spectrally integrated [16, 17]. Here, we perform spectrally resolved scattering in proton-heated matter for the first time. Beyond demonstrating the technique, we use a short-pulse x-ray source to observe free electron populations shortly after heating. The observed variation in measured signal with target material has important implications for our understanding of the dynamics and long-range structure of multi-eV matter.

1.3 Hydrogen at high pressure

The study of high-pressure hydrogen dates to the 1930s, when Wigner first proposed a stable metallic phase of hydrogen at high pressure [18]. While this is of considerable interest from the perspective of basic science, attention to hydrogens high-pressure properties has since grown as it its role in the structure of giant planets has become clear. Jupiter is an excellent example, since it is composed mostly of hydrogen, with a denser core that includes Helium and small amounts of heavier elements. As shown in Figure 1.2, the outer region of the planet is relatively low pressure, low density hydrogen. As one travels toward the core, the pressure increases. At some point helium begins to mix with the hydrogen. Deeper still, a very dense, high pressure solid core is found. Of course, our knowledge of details of this structure rely on calculations, which in turn need equation of state information to describe the relationship between thermodynamic variables at these high pressure [19]. For example, at some point hydrogen transitions from an insulating liquid to a conductive one. What is the pressure and depth at which that occurs? How does hydrogen mix with helium at MBar pressure? Are there multiple liquid phases at these pressures? Experiments must provide that information.

Studies of high-pressure hydrogen have advanced rapidly as methods of statically compressed samples with diamond-anvil cells have improved. In these experiments, hydrogen samples are kept at low temperature and interrogated with x-ray or laser probes. Although there has been some recent controversy [20], it appears that even at 300 GPa - the highest pressure currently available - hydrogen does not become a metal [21, 22].

A parallel track of research creates high sample pressures by launching a shock wave into a target. The first of these experiments on hydrogen were performed using the gas gun facility at Lawrence Livermore National Laboratory. These studies directly measured the conductivity in compressed deuterium and made explicit connection to the layered structure of Jupiter [23]. Subsequent work using lasers as shock-drivers of cryogenic targets pioneered velocity interferometry on laser platforms [24, 25]. Early results suggested that the compressibility of hydrogen at high pressure was significantly higher than previously believed, calling into question hydrogens Equation of State (EOS). Equally interesting, these experiments made possible the unequivocal observation of metallization of hydrogen at high temperature [26], an measurement made by tracking the change in optical reflectivity of the target during compression.

Research has continued using shocks from Z-pinches [27, 28], lasers [29] and other

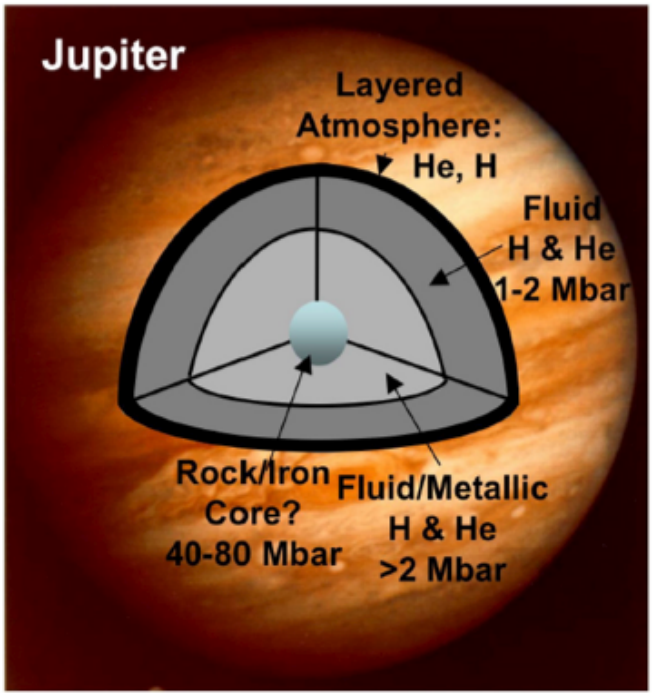

Figure 1.2: Cross section of Jupiter, showing the range of hydrogen pressures found in the planets as a function of depth. Image from [30].

energy sources. A proliferation of equation of state theories have appeared, including state of the art computational methods [34, 35], simpler chemical picture [31, 32] and hybrid models [33] to address continuing uncertainty about the hydrogen's high pressure behavior. Nevertheless, a great deal of uncertainty still exists, in part because of the experimental error bars inherent in the measurements techniques often used. Moreover, many of the biggest questions about hydrogen's high-pressure phase diagram remain open, not least the liquid-liquid phase transition [35, 36].

X-ray scattering offers a complementary diagnostic to the well established workhorse of velocity interferometry. XRTS offers a microscopic probe that is sensitive to the electron and ion structure in the system, while VISAR constrains the thermodynamic parameters of a shocked target. This dissertation combines these methods to offer new information on the physics of shocked hydrogen.

1.4 Proton-heated matter

While shock physics has progressed on large lasers producing nanosecond length pulses, ultra-high intensity lasers have revolutionized studies of short pulse interactions. Particularly important was the discovery that high-intensity laser pulses incident on thin solid foil targets produced high energy, directional proton beams [37]. Research pursuing applications from fusion to cancer treatment have made progress engineering the beam properties [38, 39]. These beams make very effective energy sources for target heating [40]. Indeed, they provide near-instantaneous energy to the electron subsystem isochorically and thus allow for the study of warm dense matter without any pressure effects or initial perturbations to the ions.

This property of isochoric heating has been exploited by recent studies of very thin laser-heated foils [41, 42, 43]. Proton heating allows that principle to be extended to temperatures of tens of eV in bulk targets. Recent experiments using spectrally integrated scattering measurements have used this platform to study thermal melting [16] and electron-ion dynamics [17] in carbon. Spectrally resolved x-ray scattering offers a critical piece of information lacking in those experiments by directly measuring the electron structure of the hot sample. Previous work suggests the presence band structure in warm metals [44] and unexpectedly long electron-ion equilibration times [45]. By observing the free electron population in isochorically heated samples of different initial band structure, we conclude that long-range order is indeed apparent several hundred picoseconds after heating.

1.5 Outline of Dissertation

Moderately compressed hydrogen is well below solid density and 1 eV tempreature. On the other side of the WDM temperature range, particle-heated solids can reach tens of eV, yet experience none of the pressure effects of shocked matter. While these studies fall on opposite sides of the WDM phase space and use different heating techniques, they are unified by the use of x-ray scattering from electron plasma waves. By measuring ionization, we are able to better understand the behavior of electrons in these complex environments. In each case, our results suggest complex electron structure and offer a motivation to continue to improve the theoretical treatment of warm, dense matter. The remainder of the dissertation is organized as follows.

Chapter 2 outlines the theoretical basis of the laser-target interactions involved in

x-ray production, proton acceleration and target heating. It then describes the essential physics of the x-ray scattering process, focusing particularly on the electron-electron behavior that is critical to interpreting ionization measurements. Finally, it summarizes several computational models used to simulate plasmas at our experimental conditions.

Chapter 3 describes the laser systems used in this study. It then outlines the design and calibration of our proton, shock velocity and x-ray scattering diagnostics.

Chapter 4 presents the x-ray scattering studies of shocked deuterium. The cryogenic target platform is summarized and the characterization of the x-ray source developed to observe plasmons in D2 is explained. X-ray scattering results are then shown and compared with preliminary theoretical calculations.

Chapter 5 describes x-ray scattering experiments in proton-heated systems. It summarizes the target platform, laser configuration and characterization of the proton beam produced for our conditions. It then presents experimental data of x-ray scattering measurements of both temperature and ionization. Finally, it compares these observations with preliminary calculations.

Chapter 6 concludes by summarizing our results and suggesting avenues for further research.

Chapter 2

Theoretical Background

2.1 Materials in the warm, dense regime

Electron coupling and degeneracy

The warm, dense material (WDM) regime occupies the parameter space between hot plasmas and condensed matter, exhibiting some of the properties of both states of matter. Typical temperatures are $\sim$ 0.1-10 eV and density on order of that of solids. Since thermal melting generally occurs at sub-electron volt temperatures, this regime is characterized by disordered but strongly interacting ions (often only partially ionized) and an electron gas with density near that of solid metals. Thus, unlike weakly coupled plasmas, electrons are often degenerate. That is, they have a degeneracy parameter of $\Theta < 1$

$$\Theta = \frac{k_B T_e}{\epsilon_F}, \epsilon_F = \frac{\hbar^2}{2m_e}\left(3\pi^2 n_e\right)^{2/3} \tag{2.1}$$

where k_B is the Boltzmann constant and T_e, n_e and m_e are electron temperature, density and mass respectively. The Fermi energy, ϵ_F represents the energy of the highest occupied quantum state of the electron system. Thus Θ, the ratio of thermal to Fermi energies, gauges the effect of Fermi statistics on the electrons in the system; $\Theta < 1$ indicates that quantum mechanical effects play a significant role in the electron gas. As illustrated in Fig 2.1, experiments in this work access a parameter space of partially to highly degenerate electrons.

While electrons in a classical plasma are distributed according to Boltzmann statis-

tics,

$$f(E) = \sqrt{\frac{E}{\pi k_B T_e}} \exp\left(\frac{-E}{k_B T_e}\right) \tag{2.2}$$

for electron energy E, degenerate electrons obey the Fermi-Dirac distribution,

$$f(E) = \frac{1}{1 + e^{\beta(E_i - \mu)}} \tag{2.3}$$

where μ is the chemical potential and $\beta = 1/k_B T_e$. A step function at zero temperature, the Fermi distribution spreads out considerably at finite temperature, and electrons fractionally occupy states far above the Fermi energy.

The electron coupling parameter is defined as

$$\Gamma_{ee} = \frac{e^2}{4\pi\epsilon_o \tilde{d} k_B T_e}, \tilde{d} = \left(\frac{4\pi n_e}{3}\right)^{-1/3} \tag{2.4}$$

where $\tilde{d}$ is the Wigner-Seitz radius, the scale length corresponding to the volume occupied by a single electron in the plasma. Similar definitions can be made for the ions in the system. In an ideal plasma, $\Gamma \ll 1$; for increasing Γ, correlations become increasingly important. Experiments here access $\Gamma \geq 1$, and our analysis must take account of electron correlations.

The plasmon resonance

The experiments in Chapters 4 and 5 exploit the dependence of electron-electron resonances on plasma parameters to determine ionization in a variety of extreme conditions. Here, following [46], we sketch a derivation of this dispersion relation. These oscillations, sometimes called Langmuir waves or plasmons, exist as electrostatic resonances between particles of like charge. Writing the equations of continuity and momentum conservation for an electron fluid,

$$\frac{\partial n_e}{\partial t} + \nabla \cdot (n_e \mathbf{v}) = 0 \tag{2.5}$$

$$m\left(\frac{\partial}{\partial t} + \mathbf{v} \cdot \nabla\right)\mathbf{v} = -\frac{1}{n_e}\nabla P_e - e\left(\mathbf{E} + \mathbf{v} \times \mathbf{B}\right) \tag{2.6}$$

Gauss's Law for this sytem is

$$\nabla \cdot \mathbf{E} = \frac{-e n_e}{\epsilon_0} \tag{2.7}$$

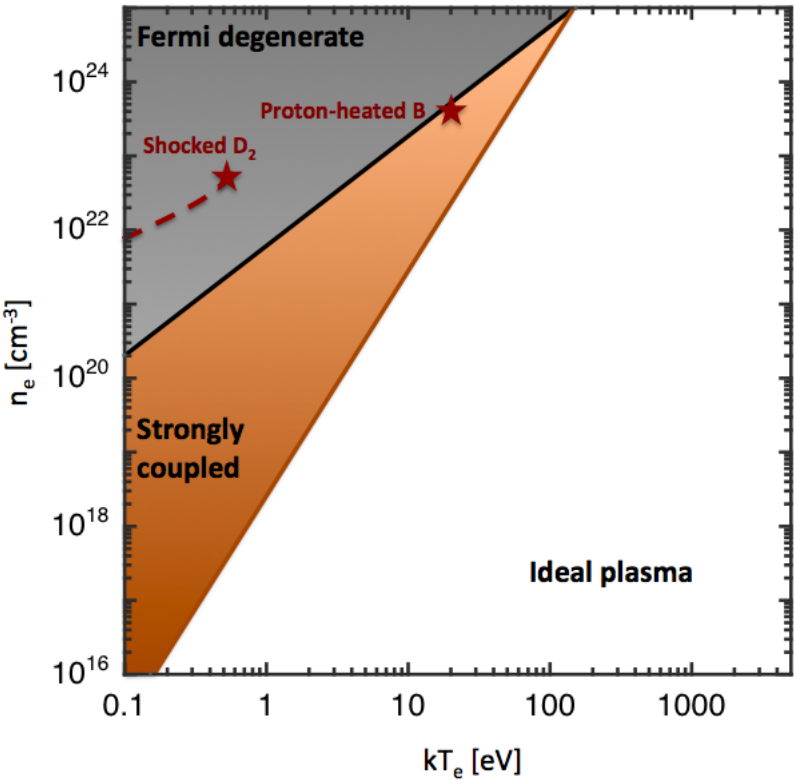

Figure 2.1: Regions of plasma coupling constant as a function of temperature and density. The red stars indicate the approximate regions probed in these experiments, where electrons are partially degenerate and moderately to strongly coupled.

Assuming a small perturbation (subscript 1) to a background value (subscript 0) for electron density, velocity and electric field,

$$n_e = n_{e0} + n_{e1}, \mathbf{v} = \mathbf{v}_0 + \mathbf{v}_1, \mathbf{E} = \mathbf{E}_0 + \mathbf{E}_1 \tag{2.8}$$

which we can substitute into our original equations and linearize by dropping products of perturbation terms. Then

$$\frac{\partial n_{e1}}{\partial t} + n_{e0}\nabla \cdot \mathbf{v}_1 + \mathbf{v}_0 \cdot \nabla n_{e0} = 0 \tag{2.9}$$

$$m\frac{\partial \mathbf{v_{e1}}}{\partial t} = \frac{1}{n_{e0}}\gamma k T_e \nabla n_{e1} - e\mathbf{E}_1 \tag{2.10}$$

$$\nabla \cdot \mathbf{E}_1 = -\frac{en_{e1}}{\epsilon_0} \tag{2.11}$$

where we have introduced the adiabatic index, or ratio of specific heats $\gamma = C_P/C_V$, to write the pressure gradient in the plasma. Now, taking $\partial/\partial t$ of 2.9 and $\nabla\cdot$ of 2.10 and combining them (dropping the subscripts), we get

$$\frac{\partial^2 n_e}{\partial t} - \frac{\gamma k T_e}{m}\nabla^2 n_e - \frac{en_0}{m}\nabla \cdot \mathbf{E} = 0 \tag{2.12}$$

which is rearranged, using Gauss's law, into

$$\left[\frac{\partial^2}{\partial t^2} + \omega_p^2 - a_e^2\nabla^2\right] n_e(\mathbf{r}, t) = 0 \tag{2.13}$$

We recognize this as a wave equation with a propagation speed

$$a_e = \left(\frac{\gamma k T_e}{m}\right)^{1/2} \tag{2.14}$$

and, the plasma frequency $\omega_p = (e^2 n_0/\epsilon_0 m)^{1/2}$. We can find the dispersion relation with an ansatz for the electron density, $n_e(\mathbf{r}, t) \sim e^{-i(\omega t - \mathbf{k}\cdot\mathbf{r})}$, to give the derivatives

$$\frac{\partial}{\partial t} \rightarrow -i\omega, \nabla \rightarrow i\mathbf{k} \tag{2.15}$$

Applying these identities, we get the classical Bohm-Gross dispersion relation [47],

$$\omega^2 = \omega_p^2 + \frac{3k_B T_e}{m_e}k^2 \tag{2.16}$$

for electron-electron resonances in a plasma. At the relatively high densities and low temperatures of interest here, it is possible to make a more accurate calculation of dispersion. Recent work [48] has found an analytical approximation by expanding the zero of the real part of the dielectric function

$$\mathrm{Re}\left[\epsilon(k, \omega)\right]_{\omega=\omega_0(k)} = 0 \tag{2.17}$$

as a function of Fermi integrals. Assuming a weakly degenerate system ($\Theta \approx 1$) leads to the corrected dispersion relation for a dense plasma

$$\omega_{pl}^2 = \omega_p^2 + 3k^2 v_{th}^2(1 + 0.088 n_e \Lambda_3^3) + (\frac{\hbar k^2}{2m_e})^2 \tag{2.18}$$

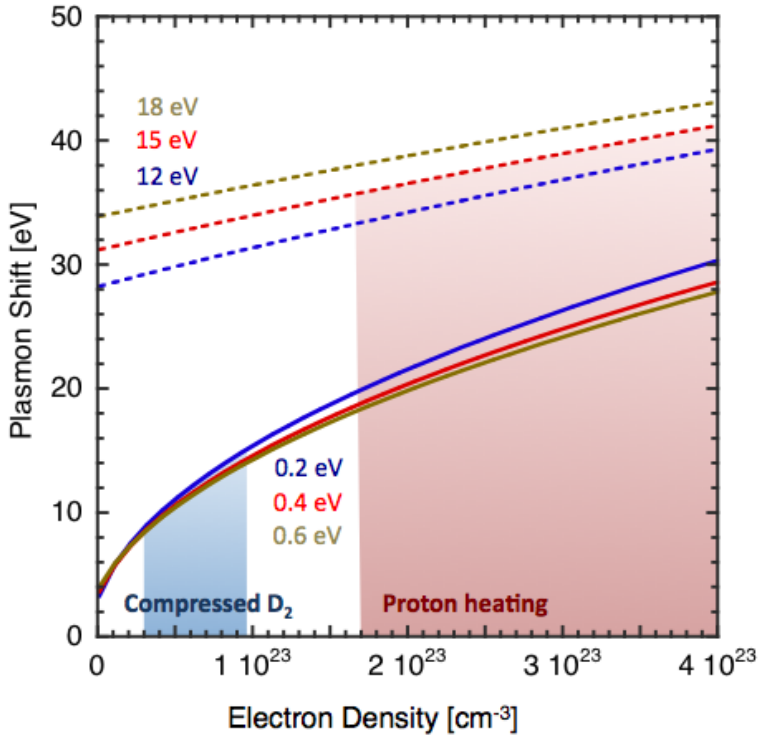

Figure 2.2: Dispersion curves calculated from equation 2.18 for the range of conditions measured in this paper, showing the variation of plasmon spectral position for various temperatures and densities.

where $v_{th} = \sqrt{k_B T/m_e}$ denotes the thermal velocity and $\Lambda_e = h/\sqrt{2\pi m_e k_B T_e}$ is the thermal wavelength. In this equation, the plasma frequency ω_p represents electron oscillations while the second term describes the effect of thermal pressure on wave propagation and the last term is a temperature-independent quantum correction. In the regime of interest here, the temperature dependence is a small one, and the position of the plasmon peak is a sensitive function of electron density. This is illustrated in Fig 2.2, showing plasmon dispersion curves for the regimes relevant to the experiments of Chapters 4 and 5. In practice, although these analytical dispersion curves are of interest in understanding the behavior of the plasmon resonance, the spectral shape and position of this feature are computed numerically as described in Sec 2.3.1.

2.2 Laser-target interaction

Electromagnetic waves in a plasma

In the experiments that follow, both target heating and x-ray source creation are accomplished with laser irradiation. Many of the important features of the laser-target interaction process are illustrated with a simple model of an electromagnetic wave in a simple plasma. The Maxwell equations for this system are

$$\nabla \times \mathbf{H} = \epsilon_0 \frac{\partial \mathbf{E}}{\partial t} - e n_0 \mathbf{v} \tag{2.19}$$

$$\nabla \times \mathbf{E} = -\mu_0 \frac{\partial \mathbf{H}}{\partial t} \tag{2.20}$$

for magnetic and electric fields $\mathbf{H}$ and $\mathbf{E}$. The current term $\mathbf{J} = -en_0\mathbf{v}$ represents electron particle motion; the much heavier ions are assumed to be immobile [46]. We treat the plasma in the fluid approximation, writing continuity and momentum conservation as

$$\frac{\partial n}{\partial t} + \nabla \cdot (n\mathbf{v}) = 0$$
$$m\left(\frac{\partial}{\partial t} + v \cdot \nabla\right) v = -\frac{1}{n}\nabla P + q\left(\mathbf{E} + \mathbf{v} \times \mathbf{B}\right)$$

for any charge species. These relations can be considerably simplified for transverse electromagnetic waves by retaining only linear terms and noting that derivatives like $\nabla \to i\mathbf{k}$ are solely longitudinal, and thus do not affect transverse motion. The electric field thus drives the electrons according to the equation of motion

$$m\frac{\partial \mathbf{v}}{\partial t} = -e\mathbf{E} \tag{2.21}$$

Taking the time derivative of 2.19 and inserting it into the curl of 2.20

$$\nabla \times (\nabla \times \mathbf{E}) = -\mu_0 \nabla \times \frac{\partial \mathbf{H}}{\partial t} = -\mu_0 \epsilon_0 \frac{\partial^2 \mathbf{E}}{\partial t^2} + \mu_0 e n_0 \frac{\partial \mathbf{v}}{\partial t} \tag{2.22}$$

which can be rearrange using vector identities into the wave equation for a transverse electromagnetic wave in a plasma

$$\left(\frac{\partial^2}{\partial t^2} + \omega_p^2 - c^2\nabla^2\right)\mathbf{E}(\mathbf{r}, t) = 0 \tag{2.23}$$

where the the speed of light $c = 1/\epsilon_0\mu_0$ and the plasma frequency is

$$\omega_p^2 = \frac{e^2 n_0}{\epsilon_0 m} \tag{2.24}$$

The dispersion for this wave can again be found by assuming a plane wave ansatz for the electric field of $\mathbf{E}(\mathbf{r}, t) \sim \exp -i(\omega t - \mathbf{k} \cdot \mathbf{r})$ to find

$$\omega^2 = \omega_p^2 + k^2 c^2 \tag{2.25}$$

The plasma has caused the plasma frequency ω_p to be added to the result for vacuum. For $\omega < \omega_p$, the result is that the electromagnetic wave cannot propagate; it decays exponentially. This defines a critical density above which light of a given frequency cannot propagate:

$$\omega = \omega_p \rightarrow n_{crit} = \frac{\omega_L \epsilon_0 m}{e^2} \tag{2.26}$$

In real experiments with high power lasers, this idealization becomes much more complicated. The laser-solid interaction causes a blow-off plasma that has gradients in electron density and interacts with the laser in complex ways. The physics of this interaction depends on the specific material, the laser wavelength and the laser intensity. However, for the purposes of this study, the two most important absorption mechanisms can be illustrated with reference to the simple dispersion relation Equation 2.25.

Inverse Bremsstrahlung

The treatment of the previous section can be improved by adding a collision term $-m\nu_{ei}\mathbf{v}$ to the right hand side of equation 2.21. Going through a similar solution process, this results in an electron velocity

$$\mathbf{v} = -\frac{ie}{m(\omega + i\nu_{ei})}\mathbf{E} \tag{2.27}$$

and a dispersion

$$\omega^2 = \omega_p^2 \left(1 - i\frac{\nu_{ei}}{\omega}\right) + k^2 c^2 \tag{2.28}$$

Here the added term denotes a damping process through which the incident field accelerates plasma electrons that then collide with ions, transferring their motion into thermal energy. This inverse bremsstrahlung process is, as the name suggests, the inverse of the process whereby an electron accelerated in an ion-field emits radiation.

In a laser-solid experiment, it is the dominant absorption mechanism in the underdense region of the blow-off plasma, and particularly at moderate (nonrelativistic) intensities, it accounts for much of the heating process.

Rigorous calculations of energy transfer rates require detailed models of electron interactions with the electromagnetic field and atomic potentials, but an approximate result for the absorbed fraction of energy into Maxwell distributed electrons in a linear density profile of scale length L_n is

$$f_{\mathrm{IB}} = 1 - \exp\left(-\frac{32}{15}\frac{\nu_{ei}(n_{cr})}{c}L_n\right) \tag{2.29}$$

where the electron-ion collision frequency in the plasma has the approximate dependence $\nu_{ei} \sim n_{cr}Z/T_e^{3/2}$ [49].

Resonance Absorption

Resonance absorption also occurs at sub relativistic intensities. The electric field must satisfy the interface condition $\nabla \cdot (\epsilon \mathbf{E}) = 0$. We can readily find the index of refraction for the plasma from Equation 2.25,

$$n \approx \frac{c}{v_\phi} = c\frac{\omega}{k} = c\frac{\sqrt{1-\omega_p^2/\omega^2}}{c} = \sqrt{1-\frac{n_e}{n_c}} \tag{2.30}$$

where n_c is the critical density. Then, a p-polarized incident wave has $\epsilon_0\nabla\cdot[(1-n_e/n_c)\mathbf{E}] = 0$, which has a resonant solution at $\omega = \omega_p$. Thus, the incident laser is absorbed at the critical surface, heating electrons by driving plasma oscillations at $\omega = \omega_p$. This can result in efficient supra-thermal electron production at relatively modest laser intensities. For instance, for a laser of frequency ω_0 incident at angle θ on a density of scale length L_n defining the parameter $\tau = (\omega_0 L_n/c)^{1/3}\sin(\theta)$, an approximate analysis gives the absorbed fraction

$$f_{\mathrm{RA}} \approx \frac{\phi^2(\tau)}{2} \tag{2.31}$$

where $\phi(\tau) = 2.3\tau\exp(-2\tau^3/3)$ [50]. This process received a great deal of attention from the laser-fusion community when it was realized that these suprathermal electrons could significantly degrade implosion performance by preheating the fuel [51]. From extensive particle-in-cell (PIC) simulations simulations and measurements, the characteristic hot electron temperature was found to scale with laser wavelength and incident intensity. Precise calculations of hot electron temperature incorporate further

absorption mechanisms such as vacuum heating, which becomes important in very short density gradients [52], and $\mathbf{J} \times \mathbf{B}$ ponderomotive heating [53]. At laser intensities of $I\lambda_\mu^2 \geq 10^{18}$ W μm/cm^2, energy transfer is some mix of these and possibly other processes. Here, the laser wavelength λ_μ is given in μm. In general, the hot electron temperature is found to scale with $I\lambda^2$ with an exponent of between 1/3 and 1/2 [50] and as much as 50 % of laser energy being converted into hot electrons. Because of the strong role laser wavelength plays in electron acceleration, in Chapter 5 we take pains to ensure that the 1ω drive laser did not create sufficient electron energy to significantly preheat the liquid deuterium in our shock measurements. Since those experiments occurred at more modest intensities, we have used the hot electron temperature estimated from pure resonance absorption [54],

$$T_{hot} \approx 10 \left[T_{keV} I_{15} \lambda_\mu^2\right]^{1/3} \text{keV} \tag{2.32}$$

where T_{keV} is the thermal electron temperature and I_{15} is the laser intensity in units of 10^{15} W/cm^2.

2.3 X-ray scattering

Our principal diagnostic tool is spectrally resolved x-ray scattering. Interpreting a measured spectrum requires an understanding of each spectral component of the signal. We fit our data with a model outlined in this section.

X-ray scattering is a photon-in, photon-out process; the goal is to determine the physics of the sample material by measuring the properties of the scattered photons. For incoming and outgoing x-rays of subscript 0 and 1 respectively, conservation of momentum and energy are written

$$\hbar\mathbf{k} = \hbar\mathbf{k}_0 - \hbar\mathbf{k}_1 \tag{2.33}$$

$$\hbar\omega = \hbar\omega_0 - \hbar\omega_1 \tag{2.34}$$

The momentum relation is a trigonometric one. Observing photons scattered at an angle θ relative to the probe defines the wavevector probed according to

$$k = |\mathbf{k}| = 4\pi \frac{E_0}{hc} \sin(\theta/2) \tag{2.35}$$

where E_0 is the x-ray source energy, h is Planck's constant and c is the speed of light. The power scattered into a given solid angle $d\Omega$ and frequency interval ω at this angle

is given by

$$P_S(\mathbf{R},\omega)d\Omega\omega = \frac{P_0 r_0^2 d\Omega}{2\pi A} N S(\mathbf{k},\omega)d\omega \times \left|\hat{\mathbf{k}}_S \times (\hat{\mathbf{k}}_S \times \hat{\mathbf{E}}_S)\right|^2 \tag{2.36}$$

where the classical electron radius $r_0 = 2.8 \times 10^{-15}$ m, P_0 is the incident x-ray power and A is the target area irradiated by the source x-rays. The polarization term $\left|\hat{\mathbf{k}}_S \times (\hat{\mathbf{k}}_S \times \hat{\mathbf{E}}_S)\right|^2 = \frac{1}{2}(1+\cos^2\theta)$ for the unpolarized x-ray sources relevant to this study. It is the dynamic structure factor $S(\mathbf{k},\omega)$ describing the spatial and temporal correlations in the sample that is responsible for the $\mathbf{k}$ and ω variation in the observed spectrum.

More compactly, the double-differential cross section for the scattering process is

$$\frac{d^2\sigma}{d\Omega d\omega} = \sigma_T \frac{k_1}{k_0} S(k,\omega) \tag{2.37}$$

where $\sigma_{Th} = \frac{8\pi}{3} r_0^2 = 0.655 \times 10^{-24}\text{cm}^2$ is the classical Thomson cross section. This makes sense: the radiation is scattered from all electrons in the system and therefore scales with the Thomson cross section, modulated by target-dependent correlations contained in the structure factor. Formally, the dynamic structure factor of all electrons in the system can be written

$$S(k,\omega) = \frac{1}{2\pi N} \int e^{i\omega t} \langle \rho_e(\mathbf{k},t)\rho_e(-\mathbf{k},t)\rangle dt \tag{2.38}$$

where $\langle ... \rangle$ indicates the ensemble average. Given the time-dependent position of the sth electron $\mathbf{r}_s(t)$,

$$\rho_e(\mathbf{k},t) = \sum_{s=1}^{Z_A N} \exp\left[i\mathbf{k}\cdot\mathbf{r}_s(t)\right] \tag{2.39}$$

is the Fourier transform of the total electron density distribution. For dense plasmas, it is usually assumed that the system is isotropic, so that the structure factor is independent of direction depends only on the magnitude of k.

In the case of dense plasmas, this is generally simplified by breaking the $S(k,\omega)$ into several distinct contributions, following Chihara's treatment of liquid metals [55, 56, 57]. The result is

$$S_{ee}(k,\omega) = |f_l(k) + q(k)|^2 S_{ii}(k,\omega) + Z_f S^0_{ee}(k,\omega) + Z_b \int d\omega' \tilde{S}_{ce}(k,\omega-\omega') S_S(k,\omega') \tag{2.40}$$

where the three right-hand-side terms correspond to contributions to the spectrum from ions, free electrons and weakly bounds electrons in the plasma. $f_I(k)$ describes the form factor of electrons tightly bound to ions; $q(k)$ refers to the electron screening cloud that follows the ion motion; Z_f is the average ionization state of the system; Z_b is the number of weakly bound electrons that are freed in the scattering process. The remaining terms describe the dynamic structure of ions, free electrons and bound electrons respectively. The integral term denotes the bound-Compton process whereby an incoming photon transfers sufficient energy and momentum to free a bound electron; the resulting spectral feature involves a convolution with the ion motion to describe the starting state. The calculation of each of these features is described in the following sections.

Qualitatively, the spectrum can be divided into three distinct features as explained above, illustrated in Figure 2.3. The elastic portion of the spectrum sits at the x-ray probe energy and results from scattering from the ions, which are nearly motionless. Scattering from the electrons is governed by the Compton and Doppler effects: the scattered radiation is red-shifted from the probe by the Compton energy and broadened by the distribution function of the electrons, resulting in a frequency shift of

$$\omega = -\hbar k^2/2m_e \pm \mathbf{k}\cdot\mathbf{v} \tag{2.41}$$

where $\mathbf{v}$ is the electron velocity. Depending on the plasma conditions, that distribution can be a classical Maxwellian or degenerate Fermi function. The third component, a the long-tailed bound-free feature, is also redshifted by the Compton energy to sit under the free-free feature.

The resulting spectrum depends on the relationship between the probe wavevector and the screening length of the system. In classical plasmas the ions are screened by electrons attracted to their Coulomb potential to produce the Debye length

$$\lambda_D = \sqrt{\frac{\epsilon_0 k_B T_e}{n_e e^2}} \tag{2.42}$$

In degenerate systems, the screening cloud is modified to obey Fermi statistics, and becomes approximately

$$\lambda_{TF} = \sqrt{\frac{\pi\epsilon_0\hbar^2}{m_e e^2}\left(\frac{\pi}{3n_e}\right)^{1/3}} \tag{2.43}$$

In practice, the screening length is calculated for any degeneracy according to the more rigorous expression

$$\lambda_S^2 = \frac{\epsilon_0 k_B T}{n_e e^2}\frac{F_{1/2}(\eta_e)}{F_{-1/2}(\eta_e)} \tag{2.44}$$

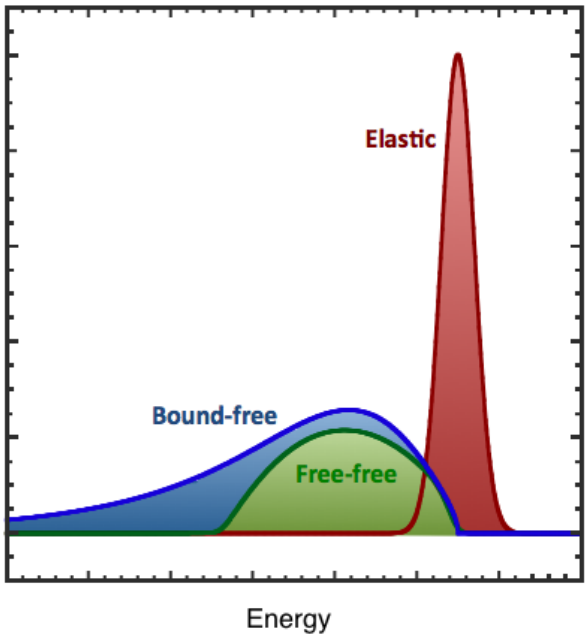

Figure 2.3: An idealized x-ray scattering spectrum divided into three spectral components in the same way as equation 2.40.

where the Fermi integral

$$F_j(y) = \frac{1}{\Gamma(\mathrm{J}+1)} \int_0^\infty \frac{dx x^j}{\exp(x-y)+1} \tag{2.45}$$

The plasma is probed at a scale length dependent on the wavevector k, $\lambda^* \approx 2\pi/k$. This defines a scattering parameter

$$\alpha = \frac{1}{k\lambda_S} \tag{2.46}$$

so that $\alpha > 1$ denotes probing outside the plasma screening length and $\alpha < 1$ probes inside the screening length. As a result, by performing scattering in the small-k limit, we can observe collective plasma effects like the electron-plasma wave resonance. At large k, we probe individual electron motion and measure its distribution function. Since these processes have different dependencies on the plasma parameters, this allows us to diagnose different quantities at different scattering angles.

Electron Response

The free electron feature of the spectrum requires an accurate treatment of the dynamic electron interactions described with the dielectric function of the system, $\epsilon(k,\omega)$. This can be directly related to measured quantities in a scattering experiment through the fluctuation dissipation theorem

$$S_{ee}(\mathbf{k},\omega) = -\frac{\epsilon_0 \hbar k^2}{\pi e^2 n_e} \frac{\mathrm{Im}\left[\epsilon^{-1}(\mathbf{k},\omega)\right]}{1-\exp\left(-\hbar\omega/k_B T_e\right)} \tag{2.47}$$

and the imaginary and real parts of $\epsilon(\mathbf{k},\omega)$ are connected through the Kramers-Kronig relations [citation]. The dielectric function is connected to the polarization function $\Pi(\mathbf{k},\omega)$ through the equation

$$\epsilon(\mathbf{k},\omega) = 1 - \frac{1}{\epsilon_0 k^2}\Pi_(\mathbf{k},\omega) \tag{2.48}$$

As explained above, for warm, dense systems we assume structural disorder, so that the spatial behavior can be expressed in terms of only a scalar value k. (For a review of the theory for solids, see [6]).

The task is then to calculate the polarization function for a dense, finite temperature electron gas. The theoretical basis for this analysis borrow heavily from its roots in solid state physics. A typical starting point is the random-phase-approximation that accounts for the response of the individual particles of an electron gas and the resulting induced field in a self-consistent way. The derivation is lengthy (see [58]) but the resulting polarization function is

$$\Pi^{RPA}(k,\omega) = \frac{1}{\Omega_0}\sum_p e^2 \frac{f^e_{p+k/2} - f^e_{p-k/2}}{\Delta E^e_{p,k} - \hbar\left(\omega + \mathrm{i}\eta\right)} \tag{2.49}$$

where the limit $\eta \to 0$ is implied and f^e_p denotes the Fermi function. $\Delta E^e_{p,k} = E^e_{p+k/2} - E^e_{p-k/2} = \hbar^2 \mathbf{k}\cdot\mathbf{p}/m_e$.

This result is sufficient to explain many of the properties of dense plasma electrons, but it can be improved by accounting for exchange and correlation effects between electrons. In k-space, this is often accomplished with a correction to the Coulomb potential in the form of a local-field correction function $G(k)$, so that the polarization function becomes

$$\Pi(\mathbf{k},\omega) = \frac{\Pi(\mathbf{k},\omega)}{1 + G(\mathbf{k},\omega)\Pi^{RPA}(\mathbf{k},\omega)/(\epsilon_0 k^2)} \tag{2.50}$$

A finite temperature parameterization for this function in the context of x-ray scattering is discussed in [59].

More attention has been focused on developing a model that includes electron collisional broadening to the electron feature. This treatment relies on the Mermin formulation for a dielectric function that includes a collision term but still obeys low order sum rules [60]. This results in the nonlocal dielectric function

$$\epsilon^M(\mathbf{k},\omega) - 1 = \frac{\left[1 + i\nu(\omega)/\omega\right]\left[\epsilon^{RPA}(\mathbf{k},\omega + i\nu(\omega)) - 1\right]}{1 + i[\nu(\omega)/\omega]\left[\epsilon^{RPA}(\mathbf{k},\omega + i\nu(\omega)) - 1\right]/\left[\epsilon(\mathbf{k},0) - 1\right]} \tag{2.51}$$

The collision frequency for the dense plasma can then be calculated in the Born approximation as

$$\nu^B(\omega) = -i\frac{\epsilon_0\Omega_0^2 n_i}{6\pi^2 e^2 m_e n_e}\int_0^\infty dk k^6 \left[V_{ei}^S(k)\right]^2 S_{ii}(k)\frac{1}{\omega}\left[\epsilon_e^{RPA}(k,\omega) - \epsilon_e^{RPA}(k,0)\right] \tag{2.52}$$

The combined effect of these two changes is most pronounced in the small-k limit, where it broadens and dampens the electron feature, particularly in a moderate density, low temperature regime like the fractionally ionized deuterium. Recent x-ray scattering experiments at Titan have also demonstrated that the plasmon dispersion changes measurably due to electron correlations, an effect that is reproduced with the local-field correction [15]. Because the RPA treatment is only broadened by wave-plasma interactions (Landau damping) it can be difficult to numerically resolve in underdamped conditions. For these reasons, we use this Born-Mermin approximation with an included local-field correction (BMA-LFC) as described in [61] in our analysis of plasmon measurements.

It is also important to note the connection between the plasma collision frequency and its optical properties. In particular, within the Drude theory the dynamic conductivity is

$$\sigma(\omega) = \frac{\epsilon_0\omega_p^2}{i\omega + \nu(\omega)} \tag{2.53}$$

If collisional broadening of the plasmon is sufficient, it is possible to measure the conductivity directly from the plasmon width [3].

Finally, an important feature of the electron structure at small-k is its intensity asymmetry about the source energy, which follows the detailed balance relation

$$\frac{S(\mathbf{k},\omega)}{S(-\mathbf{k},-\omega)} = e^{-\hbar\omega/k_B T_e} \tag{2.54}$$

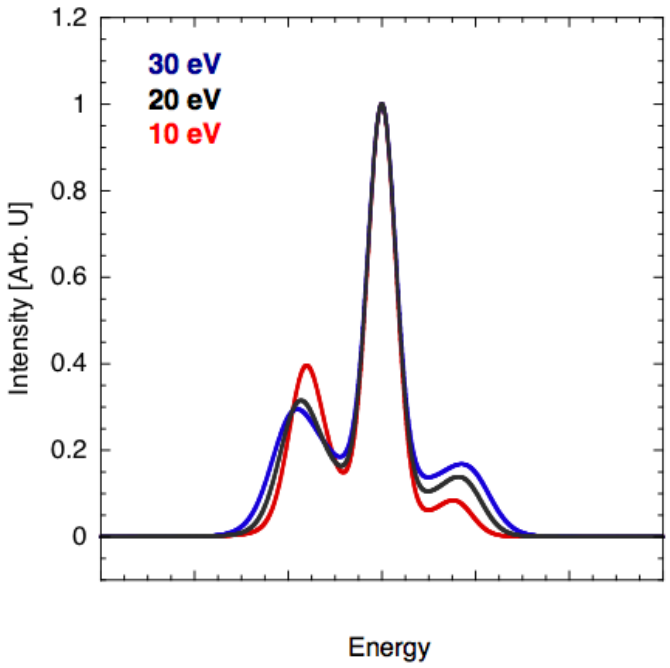

Figure 2.4: Illustrative calculations of synthetic x-ray scattering spectra showing the dependence of the plasmon intensities on temperature. Since most plasmas in this temperature range have significant ionization, in practice the electron feature disperses more broadly and the upshifted feature is too dim to detect.

Although in most cases this results in an upshifted signal of immeasurably small intensity, at relatively high temperature and low density, it can be observed above the noise and provide a first-principles temperature measurement [62]. Synthetic spectra showing the temperature dependence of the plasmon position and intensity are shown in Figure 2.4.

Ion Response

A 'quasi-elastic' spectral feature centered at the x-ray source energy comes about from x-ray scattering off electrons which follow the ion motion, including an ion screening charge and tightly bound electrons. The tightly bound electrons are represented by the ionic form factor $f_I(k)$ - that is, the bound electron density in Fourier space.

The electron screening cloud is $q(k)$, so that the total elastic scattering intensity is $W(k) = [f_I(k) + q(k)]^2 S_{ii}(k)$. Although the ion correlations include thermal motion and ion-acoustic fluctuations, current experiments lack the resolution to detect this low-frequency component. Thus, in practice our calculations make the approximation $S_{ii}(k,\omega) = S_{ii}(k)\delta(\omega)$, where $S_{ii}(k)$ is the static ion structure factor.

Calculations of $S_{ii}(k)$ can be done in several ways. The most robust is to explicitly calculate the ion correlation function from *ab initio* simulations like the MD-DFT model discussed in see Section 2.5.3. In particular, the because the static structure factor is directly linked to the radial correlation function through the relation

$$S(k) = 1 + \rho \int d\mathbf{r} \exp(-i\mathbf{k}\cdot\mathbf{r}) \left[g(r) - 1\right] \tag{2.55}$$

and the correlation function $g(r)$ is directly calculated from the ion positions in the MD output.

While this is a helpful benchmark for simpler theories, it is prohibitively computationally expensive for most data analysis [64]. A second approach is to numerically solve liquid-theory integral equations like the hypernetted-chain equation, which defines the structure of a liquid in terms of molecular interaction potentials [63]. This approach is more tractable but requires a knowledge of interaction potentials in a variety of partially ionized dense plasmas, a subject of ongoing research. The approach used for fitting data here relies on the model one-component plasma (OCP) system, an idealized system of ions embedded in a rigid neutralizing background. The structure of these ions is solely a function of the ion coupling constant Γ_{ii}, so it can be determined for a plasma of arbitrary temperature and density. For computational speed, we use the parameterization of [65] for an OCP system with hard sphere ions of radius σ_c.

Because inter-ionic screening plays an important role in dense plasmas [66], this bare ion potential is modified to accommodate an effective screening charge

$$q_{sc}(k) = Z \frac{k_{De}^2}{k^2} S_{ee}^0(k) \tag{2.56}$$

where the inverse Debye length k_{De} defines the screening scale. Using a pseudopotential of the form

$$f_v(k) = -\frac{k_{Di}^2}{k^2} \cos^2\left(k\sigma_c/2\right) \frac{q_{sc}(k)}{Z} \tag{2.57}$$

this theory allows the screened plasma structure to be computed from the parametrized OCP value $S_{ii}^{OCP}(k)$ as the SOCP value

$$S_{ii}(k) = \frac{S_{ii}^{OCP}(k)}{1 + f_v(k) S_{ii}^{OCP}(k)} \tag{2.58}$$

In dense plasmas, the precise screening behavior is challenging to model well. In some cases the SOCP theory above predicts higher elastic scattering intensities than have been measured in collective scattering experiments. Thus, determining $q(k)$, particularly in the small-k limit, is a matter of ongoing research [67].

Bound-free component

The bound-free component arises from inelastic scattering that involves sufficient energy transfer to free weakly bound electrons and thus only exists at Compton energies greater than the electron binding energies. Accurate calculation of this feature requires a knowledge of the initial electron state and the final state it scatters into. In our analysis, the bound-free structure factor $\tilde{S}_{ce}(k,\omega)$ is computed in the form-factor approximation, an approach that approximates initial and final electron states as Coulomb and plane wave-functions respectively [3]. In the limit of small binding energies, this approach reproduces the impulse approximation of [68], an approach in wide use in the synchrotron community.

Finite density and temperature can change binding energies in the plasma through the continuum lowering process. As atoms are pushed closer together, high-lying electron states overlap multiple ions, and the electron can tunnel out of the ionic potential, effectively becoming a negative energy continuum state. The effect of this is to lower the ionization potential of the electron, and thus shift the onset of bound-free scattering. The theory used to analyze the scattering data computes this continuum lowering using the model due to Stewart and Pyatt [69]. Their approximation gives the lowering of the ionization potential as

$$\Delta E_B = \frac{Z_f e^2}{4\pi\epsilon_0 \lambda_S} \tag{2.59}$$

with an ionization state of Z_f and a screening length of λ_S. Because the bound-Compton spectral component has a strong dependence on continuum lowering and the bound electron momentum distribution, and because it becomes increasingly important in higher-Z systems, a significant amount is energy is being dedicated to developing improved models. Of particular note are the hot plasma average atom approach of Salzmann [70, 71] and Green's function methods based on existing condensed matter techniques [72].

2.4 Shocks and equations of state

Shock heating

Laser energy can generate shocks by ablation of material at the laser-target interface. The absorbed laser energy quickly creates an expanding plasma at the target surface, and the reaction force drives a shock wave into the target. This discontinuity propagates through the target, compressing and heating it, as illustrated in Figure 2.5. The shock front obeys several jump conditions, which can be expressed in a simple one-dimensional approximation using conservation of mass, momentum and energy. Defining the shock velocity as u_s, the particle velocity of shocked matter u_P the unshocked and shocked mass densities ρ_0 and ρ_1, we can express the conservation of mass across the shock front as

$$\rho_0 u_s = \rho_1(u_S - u_p) \tag{2.60}$$

In a time interval of dt we can express pressure as $\rho_0 u_s dt(\frac{u_p}{dt})$ where the first term denotes mass per unit volume in a given area and the term in brackets is acceleration. Thus Newton's second law gives

$$P_1 - P_0 = \rho_0 u_s u_p \tag{2.61}$$

which is an expression of conservation of momentum. The third jump condition follows from conservation of energy. Equating PdV work with the sum of changes in internal and kinetic energy, we can write

$$E_1 - E_0 = \frac{1}{2}(P_1 + P_0)(V_0 - V_1) = \frac{1}{2}(P_1 + P_0)\left(\frac{1}{\rho_0} - \frac{1}{\rho_1}\right) \tag{2.62}$$

These three conservation expressions describe the set of possible states that can be reached with an idealized one-dimensional shock in a sample with the initial conditions (E_0, P_0, ρ_0), and are often labeled the Rankine-Hugoniot relations; a single shock is thus said to traverse the principal Hugoniot of target conditions. Aside from these initial conditions, these three equations contain five variables, related through the material's Equation of State (EOS). In essence, the EOS describes the state of the material under a given set of conditions by relating thermodynamic variables to one another. It is possible to measure the equation of state along the shock Hugoniot by exploiting the above relations. By measuring two of the five variables directly, one closes the system and constrains the rest. This is typically done by measuring shock and particle

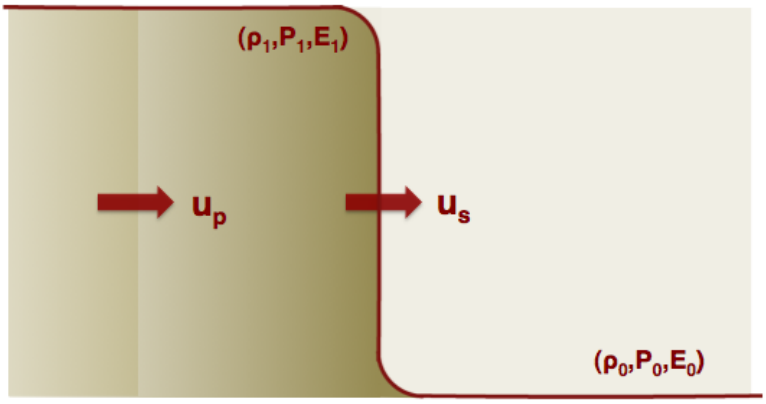

Figure 2.5: Schematic of a one-dimensional shock front.

velocities with interferometry, a trick that typically uses impedance matching to determine the particle velocity in a target by observing the breakout velocity in a second material of known equation of state [73]. This allows an experimentalist to construct a time history of both particle and shock velocities in a dynamic experiment and thus measure the EOS of a material across a variety of conditions along the Hugoniot.

Proton production and heating

The interaction of a high-intensity laser pulse with a solid target can create a beam of protons extending to 10s of MeV in energy. While recent experiments have demonstrated quasi-monoenergetic protons in excess of 50 MeV [38], dynamic heating experiments are best served with a continuum of protons at energies of a few MeV, which can be stopped in a few tens of μm in typical solids.

At laser intensities of $\sim 10^{18}$ W/cm^2, such protons are created through the target normal sheath acceleration (TNSA) mechanism. The protons originate from the back surface of a laser-irradiated foil, largely from the hydrogen atoms in hydrocarbon contamination of the target surface. The laser-solid interaction creates a stream of hot electrons that penetrate the target, leaving the back surface and creating a large electrostatic potential. This expansion front pulls ions from the surface of the foil, accelerating them to MeV energies. Detailed calculations are performed using particle-

in-cell (PIC) simulations, since the beam performance depends both on the subtleties of the high-inensity laser-target interaction and on hot electron transport in the foil. Simulations and experiments suggest an approximate maximum acceleration energy of

$$E_{max} = 2T_{hot}\left[\ln(t_p + t_p^2 + 1)^{1/2})\right]^2 \tag{2.63}$$

where $t_p = \omega_{pe} t_{acc}/(2\exp)^{1/2}$ [39].

In this intensity regime, the hot electron temperature is mainly a function of the ponderamotive potential of the laser, scaling with intensity as

$$T_{hot} = m_e c^2\left[(1 + I\lambda_{\mu m}^2/1.37 \times 10^{18})^{1/2} - 1\right] \tag{2.64}$$

The duration of proton acceleration is $t_{acc} \sim \ 1.3\tau_{laser}$. This is significant, since it means that using a combination of proton heating and K-α probing allows for measurements with an intrinsic time resolution on the order of the laser pulse length - a few picoseconds, in our case.

Protons incident on a solid are decelerated by interactions with the electrons in the material (electron stopping) and by direct collisions with ions. This process is described in the equation for the stopping power

$$S(E) = -\frac{dE}{dx} \tag{2.65}$$

for the quantity the describes the energy lost by a proton dE over a path dx. At proton energies of a few MeV, the electron-proton interactions dominate the process. The stopping power is higher for lower energies, since lower energies have time to interact more strongly with the electron field. Thus, the process of proton stopping has an element of positive feedback - as the proton slows, its rate of slowing increases, until it is suddenly stopped at the so-called Bragg peak, the depth at which most protons deposit their energy. The stopping power of many materials is tabulated in NIST's PSTAR database [74]. An example calculation of the stopping power of nitrogen is shown in Figure 2.6. Although this information is valuable for experimental design, we also perform simulations that self-consistently include proton stopping within the larger LASNEX radiation-hydrodynamic package [75].

Stopping power is quoted in terms of areal density, making it nearly Z-independent. The stopping power of B is thus extremely similar. For the relevant proton energy regime of a few MeV proton stopping is almost completely due to electron-proton interactions, rather than ion collisions. As a result, the protons deposit their energy into the electron subsystem of the target, making it possible to measure electron-ion coupling over the equilibration time of the target.

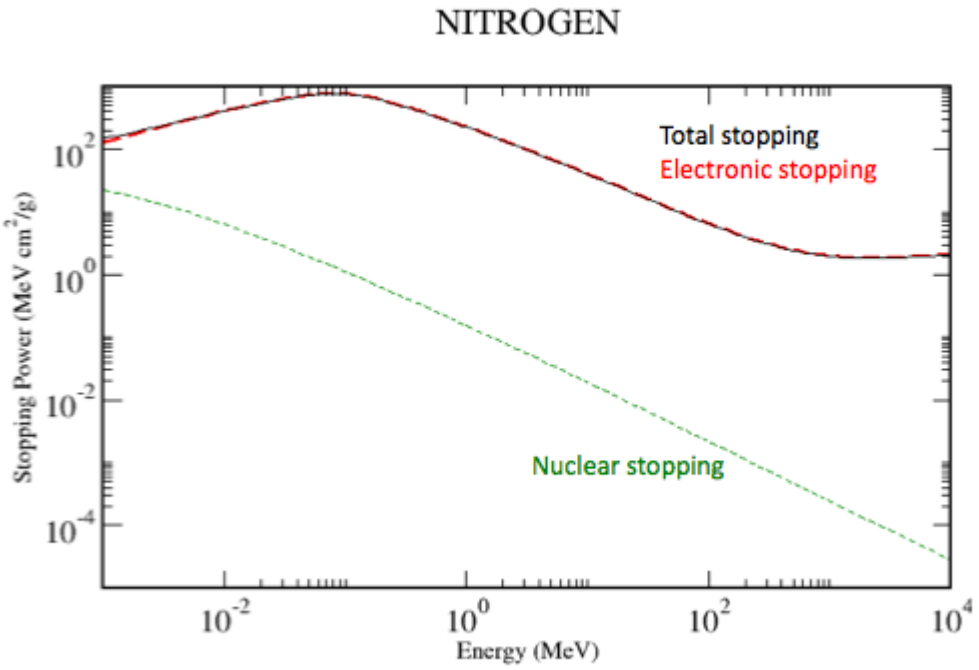

Figure 2.6: The stopping power of Nitrogen, computed from the NIST PSTAR database [74]. At energies of a few MeV the vast majority of proton stopping is due to electron-proton interactions

2.5 Computational modeling of warm, dense matter

Accurately modeling the properties of dense plasmas presents a challenge inherent in the warm, dense regime: particles experience the strong Coulombic interactions and quantum effects of condensed matter, but at much higher temperatures and without the ground state structural symmetry. A complete calculation must therefore account for ionic disorder while preserving an accurate treatment of electron structure. In collaboration with several different research groups, the experimental results of this dissertation have been modeled using three general classes of calculation, ranging from an atom-in-plasma model to high temperature condense matter approaches. The im-

portant features of each of these methods is summarized briefly with reference to more complete explanations in the literature.

Average Atom Models

Purgatorio is an implementation of the Inferno algorithm [76] which uses an ion-in-cell model for a central ion in a spherically symmetric geometry. It numerically solves Dirac equation in terms of its major and minor components of the wave function $P(r)$ and $Q(r)$. The electron density is expressed as a function of these terms for Fermi-weighted bound and free electrons

$$4\pi r^2 \rho_{bound}(r) = \sum_i f(\epsilon_i, \mu) 2 \left|\kappa_i\right| \left\{P_i^2(r) + Q_i^2(r)\right\} \tag{2.66}$$

$$4\pi r^2 \rho_{Continuum}(r) = \int_0^\infty d\epsilon f(\epsilon, \mu) \sum_\kappa 2 \left|\kappa\right| \left\{P_{\kappa,\epsilon}^2(r) + Q_{\kappa,\epsilon}^2(r)\right\} \tag{2.67}$$

where $f(\epsilon, \mu)$ denotes the Fermi function and the chemical potential μ is found by requiring charge neutrality at the Wigner-Seitz radius. Developed for use in equation of state calculations, it provides a view of the physics of an atom in the plasma limit of negligible ion correlations effects on electron structure.

An average-atom model developed by W. Johnson [77] uses a similar approach in the non-relativistic limit, solving the Schrodinger equation for electron wavefunctions in the ion sphere. We use this model in hydrogen calculations where relativistic effects should be negligible.

MECCA

The Multiple-scattering Electronic-structure Code for Complex Applications (MECCA) code was developed by D. D. Johnson and collaborators [78] as a tool for studying electron structure in random alloys. It is an implementation of the Korringa Kohn Rostoker Coherent Potential Approximation (KKR-CPA), a mean-field, ab-initio method of calculating electron wavefunctions in random alloys. Using a multiple scattering approach, it essentially consists in finding the Green's function describing the electron system $G(r, r')$ in a cluster of atoms. This approach has been very successful in calculating x-ray absorption fine structure spectra [79] among other applications.

It is currently being extended to dissordered, finite-temperature systems like dense plasmas by introducing and averaging over a randomized set of ion configurations

computed for a given temperature with self-consistent Fermi-populated electron wavefunctions.

Quantum Molecular Dynamics

Properly treating the disordered ion system requires a finite-temperature calculation of ion dynamics. However, dense plasmas also require a sophisticated treatment of the electron structure. To date, the most well developed and robust theoretical basis for these highly coupled problems is the molecular dynamics density function theory (MD-DFT) framework. DFT describes the many-body electron problem in terms of the total electron density in the system. It has proven to be highly successful in applications from chemistry to materials science, electrical engineering and physics, and earned its discoverers the Nobel prize. DFT consists essentially in solving the Kohn-Sham equations [80],

$$\left[-\frac{\hbar^2}{2m} + V_{\text{eff}}(r)\right]\phi_k(r) = \epsilon_k\phi_k(r)$$

$$V_{\text{eff}}\left[\rho(r)\right] = \int \frac{\rho(\mathbf{r}')e^2}{|\mathbf{r}-\mathbf{r}'|}d\mathbf{r}' - \sum_{k=1}^{N}\frac{Z_k e^2}{|\mathbf{r}-\mathbf{R}_k|} + V_{\text{XC}}\left[\rho(\mathbf{r})\right]$$

where the electron density $\rho(\mathbf{r})$ can be written as a function of the electron wavefunctions $\phi(\mathbf{r})$. Given a known potential for electron exchange and correlation, $V_{\text{XC}}\left[\rho(\mathbf{r})\right]$, the electron wavefunctions are found through an iterative algorithm. Although no closed form is known for this non-local potential, it has been extensively parameterized in a variety of approximations. Developed for T= 0 systems, it was subsequently shown that a similar theory is valid for finite T [81].

The ions are treated using a molecular dynamics approach - that is, by integrating their classical equations of motion. The entire system is iteratively solved by linking the potentials experienced by the ions to the total electron wavefunction, relaxing the electron wavefunction to a given ion configuration, using that electron wavefunction to advance the ions, and solving the electron structure again until equilibrium is reached [82]. This is a computationally expensive technique, particularly at high temperatures where the Fermi-occupied electron states require calculating thousands of fractionally occupied electron bands. However, in test calculations it compares favorably with even more expensive quantum Monte Carlo approaches that cannot treat sub eV temperatures like moderately compressed hydrogen [34].

MD-DFT provides a particularly interesting comparison to x-ray scattering data because the optical properties are available through the Kubo-Greenwood relation [83, 84] for the dynamic conductivity that can be calculated from DFT wavefunctions as

$$\sigma(\omega) = \frac{2\pi e^2\hbar^2}{3m^2\omega\Omega}\sum_{\mathbf{k}} W(\mathbf{k}) \sum_{j=1}^{N}\sum_{i=1}^{N}\sum_{\alpha=1}^{3} [F(\epsilon_{i,\mathbf{k}}) - F(\epsilon_{j,\mathbf{k}})] \times \left|\langle \Psi_{j,\mathbf{k}} |\nabla_\alpha| \Psi_{i,\mathbf{k}}\rangle\right|^2 \delta(\epsilon_{j,\mathbf{k}} - \epsilon_{i,\mathbf{k}} - \hbar\omega) \tag{2.68}$$

where $W(\mathbf{k})$ is sampling weight function in the Brillouin zone, $F(\epsilon_{i,\mathbf{k}})$ is the Fermi weight of the ith band, $\Psi_{i,\mathbf{k}}$ and $\Psi_{j,\mathbf{k}}$ are the initial and final wavefunctions at energies of $\epsilon_{i,\mathbf{k}}$ and the delta function enforces energy conservation. Because of the intimate connection between conductivity and the electron dynamic structure factor, this could be used not only to compare to optical properties extracted from scattering data, but to calculate synthetic spectra directly from many-electron wavefunctions.

Chapter 3

Diagnostics and Instrumentation

3.1 Laser Facilities

The experiments presented here use high energy lasers to heat matter and create x-ray sources to probe the hot targets. We have used two laser systems, both housed at the Jupiter Laser Facility at Lawrence Livermore National Laboratory. Both lasers are based around flashlamp pumped Nd:glass amplifiers. One system, Janus, delivers two beams of near-kJ energies at ns pulse lengths. The second, Titan, is capable of producing close to 500 J of energy at nominally ps pulse durations. These two systems are suited to creating and probing different kinds of physical processes. The nanosecond time-scale corresponds to acoustic velocities at the μm spatial scale. These beams are necessary to create and probe sustained shock waves. Thus, we use Janus to study shock-compressed deuterium. The picosecond time scale of the shorter pulse laser corresponds to electron-ion dynamical time scales; its higher intensities are required to produce particle beams and short-pulse x-ray probes. Thus, we use the Titan laser to study proton-heated matter. The essential features of each facility are outlined below.

Janus laser

The Janus laser is built around a flashlamp pumped Nd:glass amplification system. It produces two identical beams at nominal energies of 1 kJ at the fundamental wavelength of λ_0 =1053 nm. Because of the long-wavelength laser-target interactions discussed in Chapter 2, shock-compression experiments often use the 527 nm second harmonic generated in potassium dihydrogen phosphate (KDP) crystals, at which delivered energies

drop to 400 J in 4 ns. Pulse lengths vary from 0.35-20 ns, with the highest efficiencies coming at 6 ns. The facility can deliver high energy shots at a maximum repetition rate of 30 min - in practice the shot rate in cryogenic experiments is limited by target cooling and warming times.

Both beams allow the insertion of continuous phase plates (CPPs) to produce a smoother, flat-topped density profile. Because shock front planarity is critical to interpreting experimental results, these phase plates allow uniformity of illumination to reduce variations in drive pressure [85].

The Janus experimental hall has a additional 532 nm Nd:YAG beam that produces 50 mJ in 20 ns and is used as a probe beam, usually for the velocity interferometry diagnostic discussed in Section 3.6. Because of these integrated diagnostics, shock physics experiments often can use both high energy lasers to drive the target to the highest possible pressures. In our case, we use one beam to produce a high intensity x-ray source, leaving only one beam to drive the shock. As a result, we are more constrained in maximum the pressures achievable in x-ray scattering experiments.

Titan Laser

Titan is a shorter pulse laser system built around the Nd:glass amplification platform of Janus. Titan combines an ultrahigh-intensity short pulse laser with one of the long-pulse beams of Janus, allowing for a variety of pump-probe experimental configurations. The short pulse system uses an Optical Parametric Chirped Pulse Amplification (OPCPA) approach that allows relatively short pulses to be amplified to peak powers of nearly a petawatt. This design is based on the principle of Chirped Pulse Amplification, the technology that made possible ultrashort pulse, high-peak-power lasers in a very compact footprint.

Laser pulses can only be amplified to the damage threshold of the gain medium, which limits the peak achievable energies. CPA overcomes this limitation by temporally stretching the pulse during the amplification stage and then re-compressing the amplified pulse down to reach high peak powers. In practice, this stretching and compression are often accomplished with optical gratings arranged to introduce different path lengths for different wavelengths of light. The resulting chirped beam has its spectral components spread out in time. After amplification, the beam is compressed with a second grating arrangement to reverse the path length change, resulting in a pulse compressed to nearly its initial length. This approach has been used particularly broadly in Ti:Sapphire laser systems, producing sub-100 fs pulse lengths. However, it

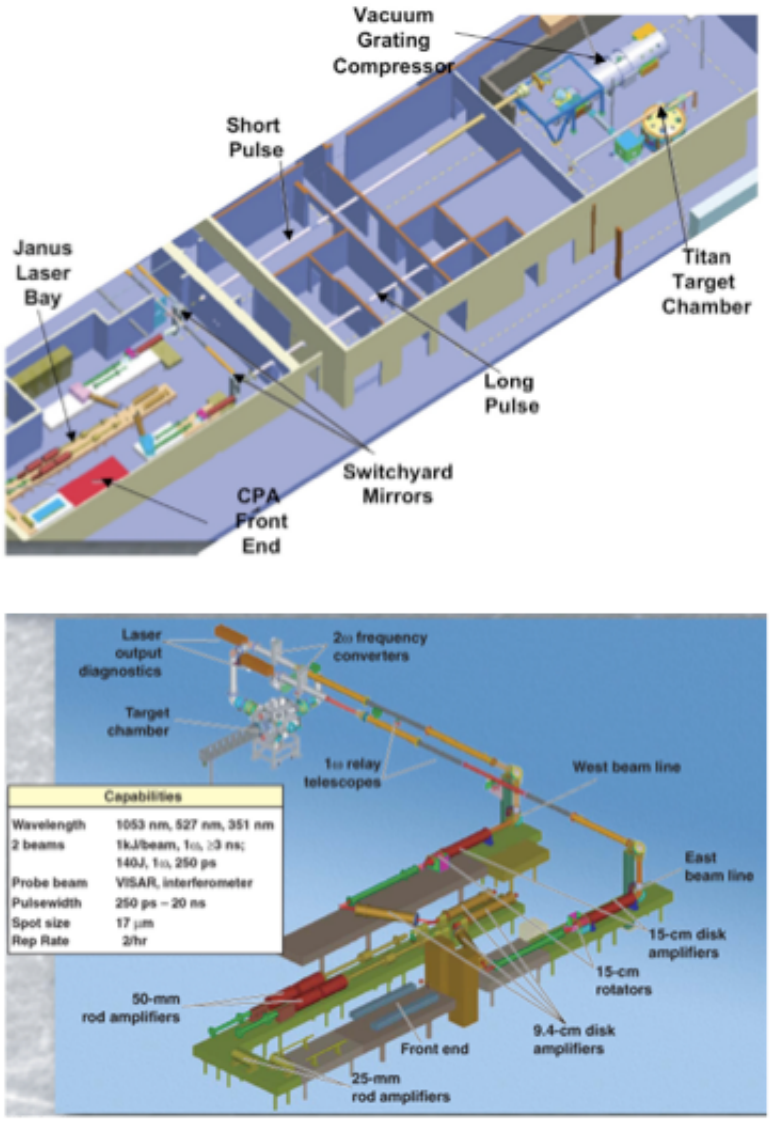

Figure 3.1: Laser systems used in this work. Top: Schematic of the Titan Petawatt laser system used for proton-heating experiments. Bottom: Schematic of the Janus laser used for shock-compression studies. jlf.llnl.gov

is also possible in glass lasers, where very large disk amplifiers have been developed for inertial fusion applications. Combined with a broadband optical parametric amplifier [86] before the final glass amplifiers, this approach can produce peak power of a petawatt in ∼500 ps pulses. At Titan, this design results in a laser that is able to generate up to 350 J at the 1054 nm fundamental in pulse lengths which can be tuned between 0.4-10 ps.

The amplified beam enters the Titan target chamber and is focused by an $F/3$ off-axis parabola (OAP) on target chamber center. Our experiments used a beam-splitting arrangement to spatially divide the short-pulse beam by reflecting a fraction of the incident laser onto a second OAP. This allowed a temporally independent probe pulse to be focused onto an x-ray converter foil, producing a short burst of K-α radiation to probe the proton-heated matter. This arrangement is illustrated in Figure 3.2. By changing the orientation of the pickoff mirror, it is possible to select between 20 and 50% of the total beam, with losses of about 10% of the total beam energy. The relative timing between the two beams was changed by varying the relative position of the splitting mirror and second OAP, within a limit of several hundred picoseconds, owing to the size limitations of the chamber. This configuration allows dynamic experiments to be performed at shorter time scales and higher intensities than can be achieved with the long-pulse laser.

3.2 Laser generated x-ray sources

Ly-α Production

An x-ray source can be produced from thermally ionized atoms by irradiating a solid with an intense laser beam. The heated target emits both continuum x-rays and spectrally narrow radiation from specific transitions. Some of the most efficiently produced of these features are the thermal lines emitted by highly ionized ions. The transitions from quantum states $n = 2$ to $n = 1$ in Helium-like and Hydrogen-like ions, called He-α and Ly-α respectively, have been the most studied for x-ray diagnostics. He-like sources are quite efficient but have more spectral satellites, since more allowed transitions are available. Nevertheless, laser produced He-α sources have been used successfully as x-ray scattering and radiography sources. Ly-α radiation tends to be more spectrally clean, offering an efficiently produced source of x-rays. The Ly-α line is a doublet, since transitions from two spin states from the $n = 2$ state are possible. The

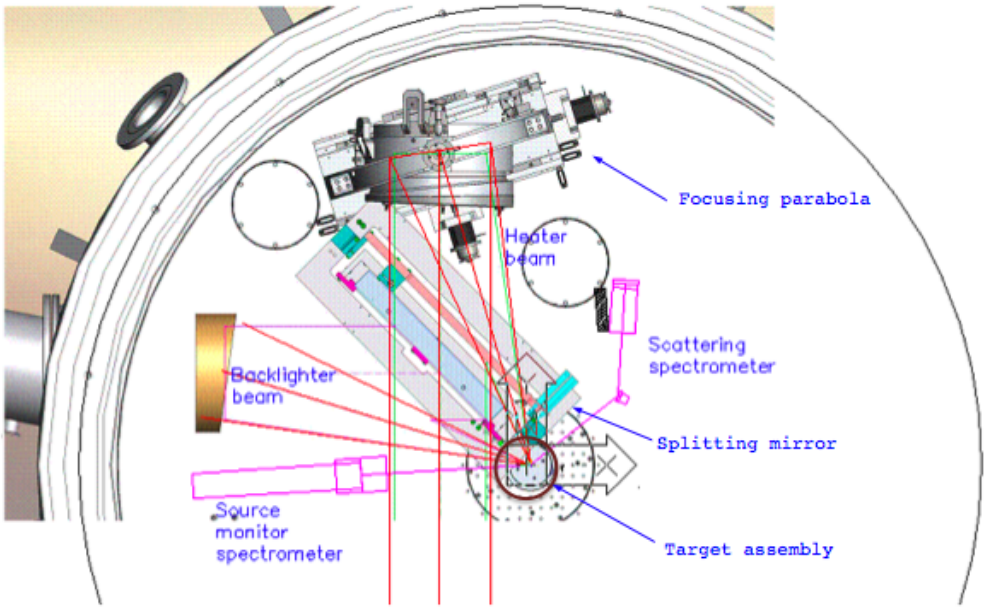

Figure 3.2: Schematic of the Titan target chamber showing the arrangement of beam splitting optics as well as the primary diagnostic spectrometers.

Chlorine Ly-α line at 2.9 keV was extensively used in early XRTS research [10]. Because liquid deuterium is an order of magnitude less dense than solid targets, we developed a new thermal source in Silicon, at 2 keV. As discussed in Chapter 4, this source is produced with comparable efficiency to the Chlorine line, about 0.1-0.2% conversion efficiency from laser energy into x-ray energy. It also has less intense satellites on the red side, making it ideal for observing plasmon oscillations at low electron densities.

Thermal radiation, since it is produced from heated ions, tends to diffuse spatially with the expanding plasma. It also emits at least as long as the nanosecond length pulses that pump it. It is therefore not suited to time-resolved measurements and care must be taken to shield the target and detectors from emission from any point other than the x-ray entrance window.

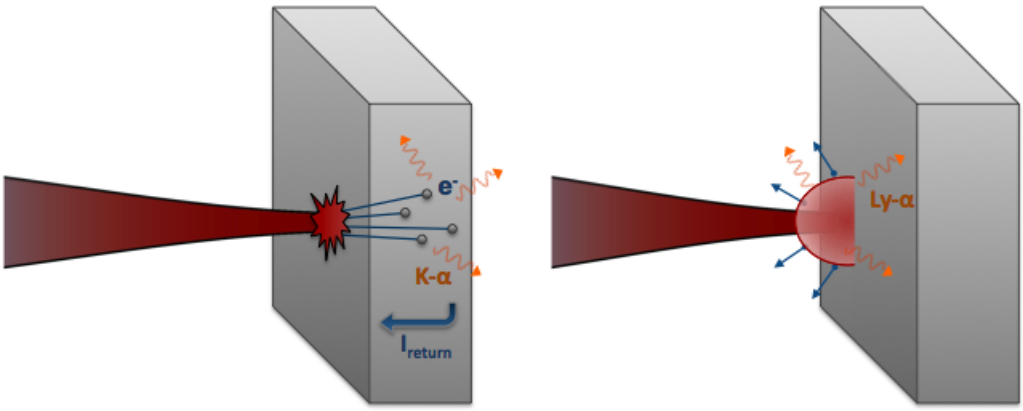

Figure 3.3: Illustration of the K-α and Ly-α production processes. Left: K-α is produced in a foil by fluorescence from an ionization due to hot electrons. Right: Ly-α is produced in the hot blow-off plasma by thermally ionized hydrogen-like ions.

K-α Production

K-α emission is the analogous case to Ly-α in a multi-electron atom. It also originates from the $2p$-$1s$ doublet, a transition that occurs in systems where the $n = 1$ electrons are ionized. Although this cannot occur thermally, it comes about when a solid is bombarded with particles or a hard radiation source. In our case, the hot electrons produced in high-intensity laser-solid interactions stream through the target, ionizing K-shell in electron-electron collisions. The vacancies are filled with transitions from L shell electrons (or M-shell electrons, producing less intense K-β radiation). For moderate-Z elements, this radiation is of multi-keV energy, has picosecond lifetimes and is sufficiently high intensity to use in single-shot experimental measurements.

For x-ray scattering applications, the conversion efficiency (CE) of laser light energy into x-rays is of critical importance to generate a detectable number of scattered photons. A review of K-α studies in [87] showed a weak intensity dependence in the CE until saturation near $I_L \sim 10^{18}$ W/cm^2, with characteristic efficiencies of between 10^{-6} and 10^{-5}, consistent with our measurements summarized in Chapter 5. These experiments also found constant x-ray production across a variety of foil thicknesses but an x-ray emission spot an order of magnitude larger than the incident laser spot size [88].

3.3 X-ray spectrometers

Mosaic crystals

Our primary x-ray scattering measurement tool is the crystal spectrometer. X-rays incident on a crystal undergo diffraction as a result of constructive interference from scattering off discrete lattice sites. As a result, the crystal diffracts incident x-rays at a specific Bragg angle, dependent on the radiation energy and crystal lattice spacing according to the Bragg relation

$$2d\sin(\theta_B) = n\lambda_0 \tag{3.1}$$

where n is the integer order of diffraction, λ_0 is the incident wavelength, d is the crystal lattice spacing and θ_B is the Bragg angle at which diffraction occurs. Since the diffraction angle is wavelength dependent, the crystal is spectrally dispersive. We can determine the approximate dispersion by differentiating the Bragg relation [89],

$$\frac{\Delta\lambda}{\lambda} = -\frac{\Delta E}{E} = \frac{\Delta\theta}{\tan(\theta_B)} \tag{3.2}$$

Noting that a change in angles $\Delta\theta$ resulting in a displacement δx across the image plane located F from the crystal surface must obey the trigonometric relationship $\Delta x = 2F\Delta\theta$, we can express the approximate energy dispersion at the image plane as

$$\frac{\Delta E}{\Delta x} = \frac{E}{2F\tan(\theta_B)} \tag{3.3}$$

At the x-ray energies used in this study, the precise experimental calibration of energy dispersion shown in the next section is quite consistent with this simple estimate.

A central challenge of x-ray scattering, particularly in the high noise environment of high energy density physics experiments, is maximizing the collection of scattered photons and minimizing broadband noise from the bremsstrahlung and high energy particles created in the laser-target interaction process. This is generally achieved by extensive shielding and spectral filtering of the detector and maximizing the efficiency of the x-ray detection system. The use of mosaic crystals can help maximize crystal reflectivity. The experiments in this work use crystal spectrometers made of highly oriented pyrolytic graphite (HOPG). HOPG is a mosaic crystal, a large crystal made up of small microscopic crystallites of nearly parallel orientation, whose slight variations in orientation is characterized by the mosaic spread γ [90]. The HOPG crystals used

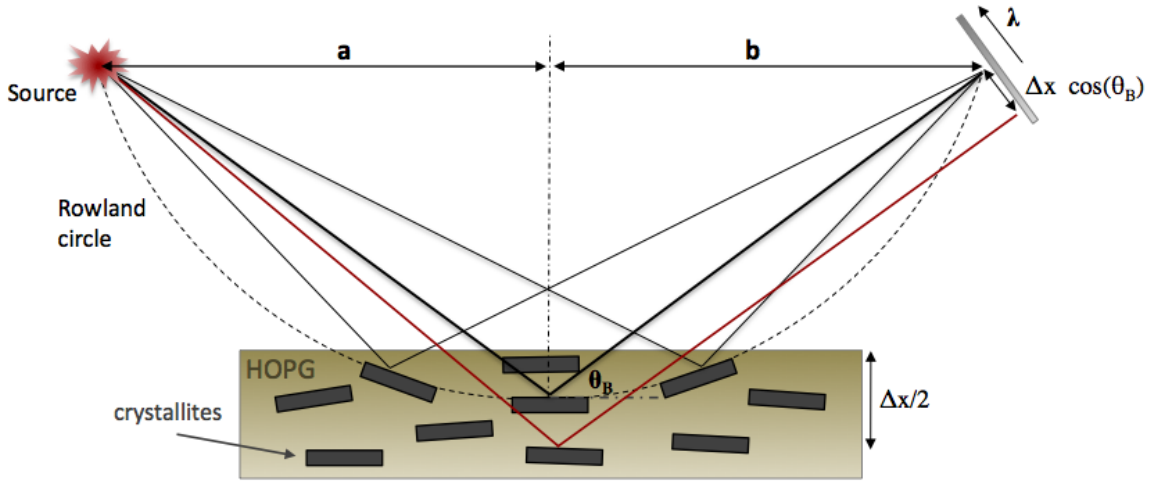

Figure 3.4: The focusing effect in a mosaic crystal. A broader mosaicity allows more crystallites to lie on the Rowland circle and satisfy the Bragg condition. Focusing occurs for $a = b$. Also shown is the depth broadening mechanism in red.

here are of grades ZYA and ZYB which are characterized by nominal mosaic spreads of $\gamma = 0.4°$ and $0.8°$ respectively.

When x-rays near the Bragg angle are incident on the crystal, they penetrate it until they encounter a crystallite with the correct orientation to fulfill the Bragg condition. In the limit of a small crystal penetration depth and footprint relative to the focal length, all incident rays of a given energy are thus diffracted to a common point, producing the so-called parafocusing effect, illustrated in Figure 3.4. This effect can be visualized as a set of crystallites which have the appropriate orientations to lie on the Rowland circle, the locus of points between a point source and point detector satisfying the Bragg condition. Since different incident energies have different Bragg angles, the crystal disperses photon energy at the convergence point. Of course, finite crystal penetration results in smearing at the focal plane, reducing the energy resolution of the instrument but increasing the total number of reflected photons. Thus, crystal mosaicity trades energy resolution for throughput, a desirable trait in HEDP experiments.

The energy resolution of the instrument is limited by several processes. In particular, the finite size and natural linewidth of the source set an upper limit on the energy resolution possible. As discussed in [89], the finite penetration of the crystal by

incident x-rays results in depth broadening. Given an x-ray penetration length in the crystal of λ_{mfp}, the incident radiation penetrates the crystal by $(\lambda_{mfp}/2)\sin(\theta_B)$. At the detector, this results in a broadening of

$$\left(\frac{\Delta E}{E}\right)_{depth} \approx \frac{\lambda_{mfp}}{2F}\cos^2(\theta_B) \tag{3.4}$$

which is the dominant limiting factor in energy resolution for K-α x-ray sources. This effect is illustrated by the red x-ray path in Figure 3.4.

Mosaic crystals have intrinsic geometric aberrations and defocusing effects which are catalogued in [91]. However, Pak and coauthors found that in laser-plasma experiments, these effects are less than linewidth broadening effects, and both are nearly an order of magnitude smaller than depth broadening [89].

Installation, Calibration and Alignment

The Bragg angle at the Ti K-α energy of HOPG at 4.51 keV is 24.2°. With room temperature targets and Titan's large target chamber, it is possible to mount the crystal and detector independently, allowing precise rotational alignment of the crystal to the Bragg angle. In the cryogenic experiments presented in Chapter 5, the target cooling apparatus and very sharp 2 keV Bragg angle of 66° requires very tight diagnostic placement. We developed a spectrometer and detector housing that integrates crystal alignment, image plate shielding and filtering, illustrated in Figure 3.5. As the figure shows, these housings are aligned offline using a HeNe laser in reflection off the HOPG crystal. The laser, crystal and image plane define a triangle which is fixed prior to insertion in the chamber. By aligning the crystal at the focal length from the target, the crystal is ensured to occupy the field of view of the target's x-ray window, and the x-ray probe energy falls in the center of the image plate at best focus. The slanted housing constrains the field of view of the crystal to the space occupied by the crystal to minimize undiffracted broadband noise in the chamber from polluting the scattering spectrum. The MS-type image plate is also shielded by a 6 μm layer of polypropylene sputtered with 10 nm of Al to reduce noise from diffusely reflected optical light without attenuating the scattered signal significantly.

The spectrometers are calibrated by direct exposure to the x-ray source. The spatial position of each spectral feature is mapped to its energy taken from the Kelly tables [92], giving the experimental dispersion for the detector. As shown in Figure 3.6, the dispersion is quite linear for both x-ray sources used in this study.

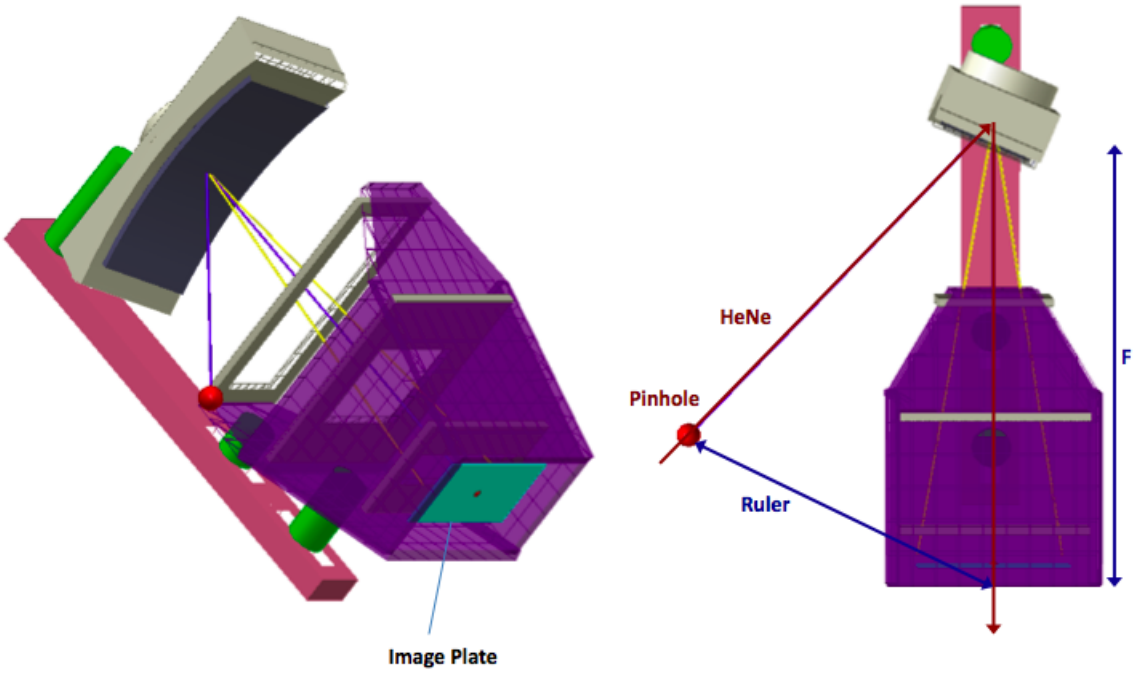

Figure 3.5: Spectrometer design used in Chapter 4 scattering studies. Left: Schematic of the spectrometer housing and crystal alignment hardware. Right: Schematic of laser alignment of the spectrometer before insertion into the chamber.

3.4 Image plates

The experiments in this work use imaging plates (IPs) to record measurements of x-ray and proton spectra. Although CCD detectors present an efficient and time-resolved alternative for x-ray detection, their cooling systems make them difficult to use in the cryogenic experimental environment of the deuterium study. Early experiments showed that the cooling system outgassed under vacuum conditions enough to cause premature ice buildup on cryogenic targets. In the high-intensity environment of the proton-heating experiments, CCDs and computer controllers are susceptible to interference from the electro-magnetic pulse (EMP) present in ultra-high-intensity laser-matter interaction studies. The choice of IPs avoids these problems altogether. In addition, they provide a dynamic range of $> 10^5$.

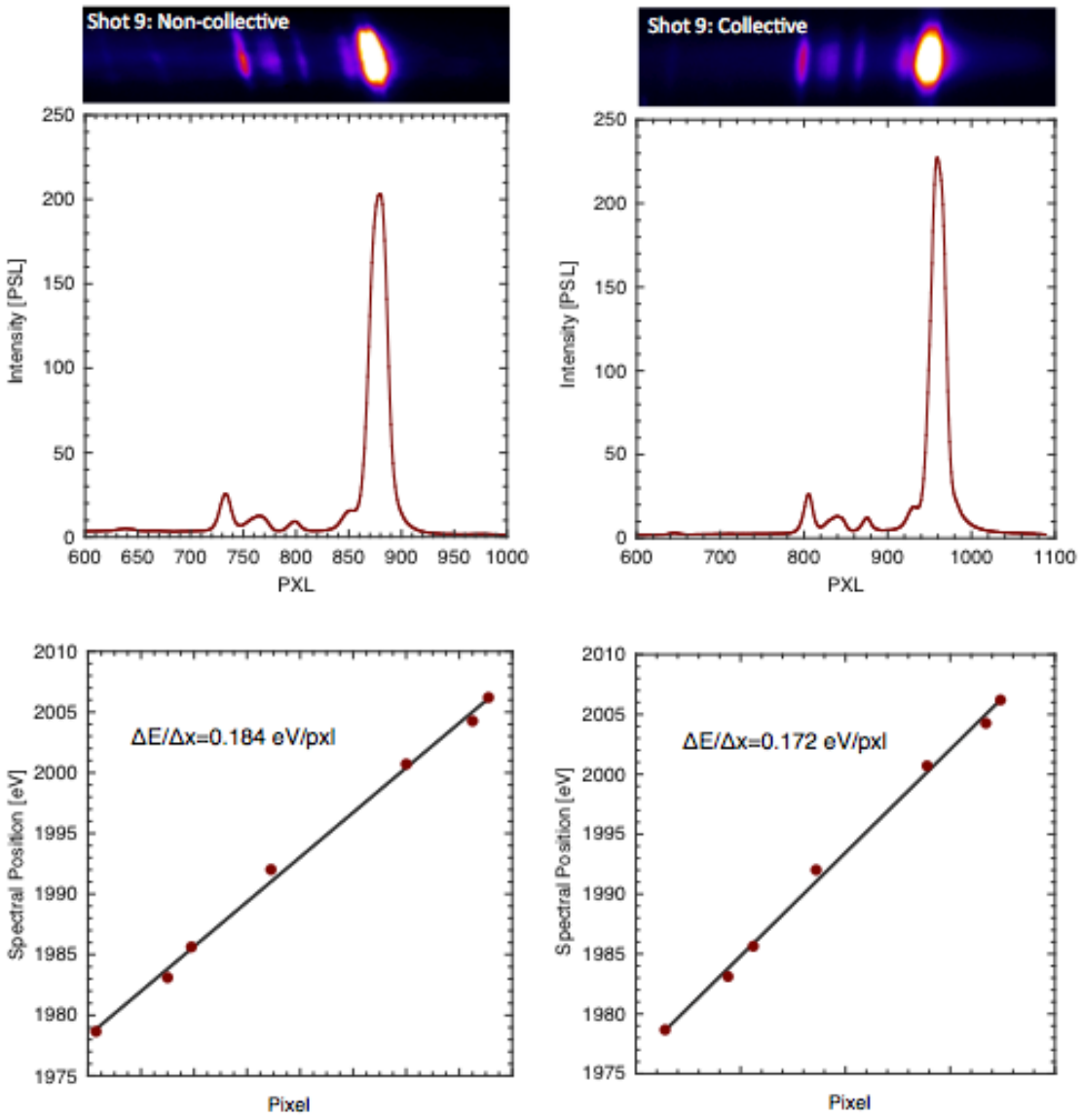

Figure 3.6: Energy calibration of forward and back-scattering spectrometers for the Silicon Ly-α line at 2005 eV. Each spectrometer is exposed to the x-ray source at the target position, establishing the position of the source line and allowing the dispersion to be calculated from the energy of the lower intensities satellites.

Image Plate	A	B	τ	m	C
TR	0.347 ±0.022	0.693 ±0.011	35.5± 5.3	0.54 ± 0.05	0.02 ± 0.002
MS	0.231±0.015	0.779 ±0.017	107 ± 19	1.07 ± 0.07	-0.51 ± 0.03

Table 3.1: Energy calibration and fade characteristics for the image plates used in this study, from [93].

The Fujifilm imaging plate technology is essentially a photostimulable phosphor layer mounted on a metal substrate. Some IPs have a protective plastic layer of $\sim$ 10 μm thickness. The phosphor layer is BaF(Br0.85,I0.15):Eu^{2+}. Ionizing radiation excites electron-ion hole pairs in the phosphor; while some immediately recombine, others are trapped in a metastable lattice defect called an F-center. The signal is stored in the image plate until thermal decay occurs over time, or the photoelectron is stimulated from the metastable state by optical light, allowing it to decay. It is read out in a scanning system that stimulates excited pixels with a He-Ne laser at 632.8 nm and detects the resulting recombination signal at 390 nm in a process known as photostimulated luminescence (PSL). The plates can then be erased with a few minutes exposure to an intense white light source, in this case a halogen lamp. Obviously, this system requires light-tight removal and transport from experimental diagnostics to the scanning apparatus.

The decay of the signal over time has been characterized in the context of laser-plasma experiments in [93]. It was found that various IP types followed an exponential decay behavior with

$$I(t) = A \exp\left(-t/\tau\right) + B \tag{3.5}$$

where A, B and τ are constants that depend on the specific IP type. The energy deposited in a given signal was calibrated to photon energy, and found to obey the equation

$$\psi = \eta\left(m\mathrm{E} + C\right) \tag{3.6}$$

where η is the absorption efficiency of the detector, given by the material composition of the detector and protective layer. The linear fit for energies below 6 keV for the two types of IPs used here is also given in Table 3.1.

The TR and MS image plates used here are very similar, using the same phosphor layer. The primary differences are that the TR active layer is 60 μm thick while in MS it is 124 μm thick. MS also has a 9 μm protective mylar layer on its front surface

while TR is uniquely designed with no protective coating. As a result, TR is more efficient for detecting softer radiation absorbed in this layer (up to about 2 keV); it is also more fragile and damages easily. Because the TR type is directly exposed to thermal radiation, it fades the most quickly.

3.5 Magnetic proton spectrometer

This study made use of a magnetic proton spectrometer whose design and calibration is explained in detail in [94]. It is particularly useful in these experiments because the radiochromic film (RCF) often used to detect MeV protons is not sensitive to low energy ions; the spectrometer, however, has a maximum energy cutoff of about 5 MeV. It operates by using permanent magnets to apply a magnetic field in the horizontal plane. Incoming protons with velocity $\mathbf{v}$ are constrained by a slit in the dispersion dimension, and subject to a Lorentz force $\mathbf{F} = e\mathbf{v} \times \mathbf{B}$. The protons are curved toward the top of the instrument, where they deposit their energy on an image plate; the spatial position of the signal on the image plate is thus a function of proton energy and magnetic field strength. The protons approximately follow the gyroradius of a charged particle in a magnetic field. However, because $\mathbf{B}$ is not spatially uniform, the precise dispersion properties of the spectrometer are determined by numerically simulating the magnetic field variation in the instrument. The instrument is experimentally calibrated by using a BAS-MS-2040 image plate whose 9 μm PET top layer acts as a range filter and introduces a low-energy cutoff in the spectrum. This is shown schematically with a sample image in Figure 3.7.

3.6 Velocity interferometry

The VISAR (Velocity Interferometer System for Any Reflector) [95] diagnostic provides a time history of the velocity of a target using interferometry and an optical probe beam. At the Janus laser facility, the VISAR diagnostic is based on the design of the instrument at Omega, described in detail in [96]. A 532 nm probe laser is reflected from a moving target, passes through collection optics and is routed to two interferometer stages. Each interferometer is arranged in a Mach-Zender configuration with an etalon of precisely known thickness placed in one leg to act as a delay element. An etalon of

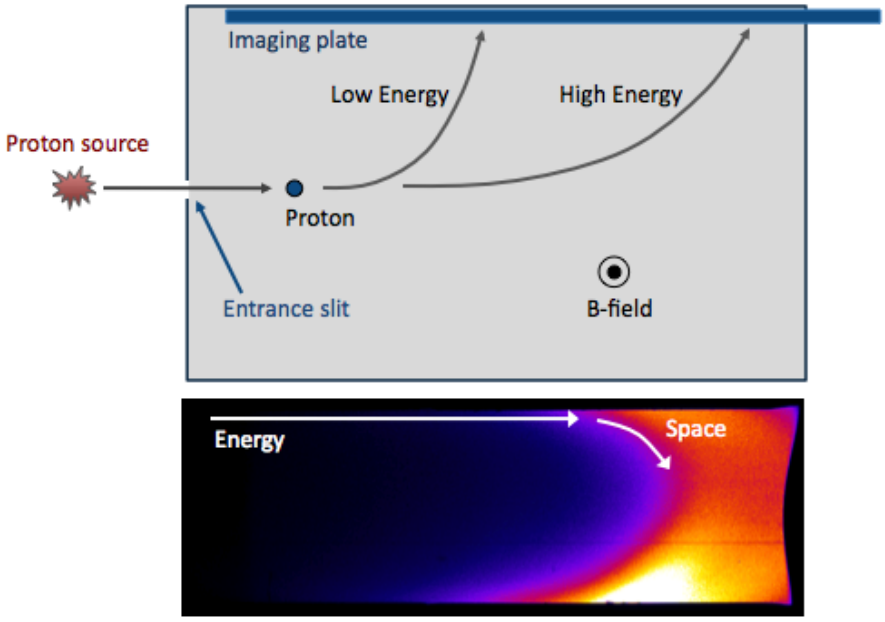

Figure 3.7: The magnetic proton spectrometer. Top: Schematic of the spectrometer operation. Bottom: Sample proton spectrum.

thickness h and index of refraction n results in a time delay of

$$\tau = \frac{2h}{c}(n - 1/n) \tag{3.7}$$

where c is the speed of light and n is the index of refraction in the etalon. This results in an interference pattern formed where the two interferometer legs recombine. This fringe pattern is imaged onto a streak camera with the slit perpendicular to the fringes. A streaked image therefore provides a record of the phase ϕ as a function of time. In cases were the shock itself is reflecting, the phase can be directly mapped to shock velocity via the equation [24]

$$\frac{\lambda\phi}{4\pi\tau(1+\delta)} = u_S \tag{3.8}$$

Where ϕ is the fringe position, λ is the probe beam wavelength, $(1+\delta)$ is a correction for optical dispersion. For shocks, which produce phase discontinuities in time, absolute velocity cannot be determined from a single interferometer, since phase is only

known to a multiple of 2π. For this reason, two interferometers are used with different etalon thicknesses (and therefore different velocity sensitivities). This makes it possible to unambiguously determine the $\phi(t)$ and therefore the velocity. Good quality interferograms carry a fringe shift uncertainty of a fraction of a fringe shift, leading to errors on the order of a percentage point in shock velocity [29]. Thus, most of the error in an equation of state measurement, particularly in a low density liquid like deuterium, enters in the impedance matching stage.

In order to reach such low systematic uncertainties, the effect of the system optics must be carefully accounted for. The velocity sensitivity is given in velocity per fringe,

$$\mathrm{VPF}_0 = \frac{\lambda}{2\tau(1+\delta)} \tag{3.9}$$

where δ is a correction term for dispersion in the delay element, typically a few percent at optical wavelengths [96]. Corrections are made for the optical properties of the target. In particular, if the signal passes through a transparent dielectric with unshocked index of refraction n_S, the VPF becomes $\mathrm{VPF}_S = \mathrm{VPF}_0 n_S^{-1}$. Further corrections are also made to account for the various specific optical elements in the collected beam path.

As seen in Figure 3.8, the VISAR diagnostic includes pick-off paths that send the reflected signal to a streaked optical pyrometer (SOP) [97] and inject an intensity monitor into the streaked spectrum. The SOP diagnostic records the optical emission of the target as function of time; by applying a grey-body emissivity, it infers the target temperature as a function of time. Doing so requires careful optical calibration; although we did not run the diagnostic for rigorous temperature measurements, we did take streaked measurements, as the broadband emission of the target provides rudimentary shock breakout and timing information to verify interferometric measurements.

The record of the probe laser intensity allows any laser variations to be divided out of the signal, providing information on the optical reflectivity of the target as it is shocked. Since reflectivity is related to the free electron population in the target, this method allowed for the observation of the finite temperature hydrogen insulator metal transition [26].

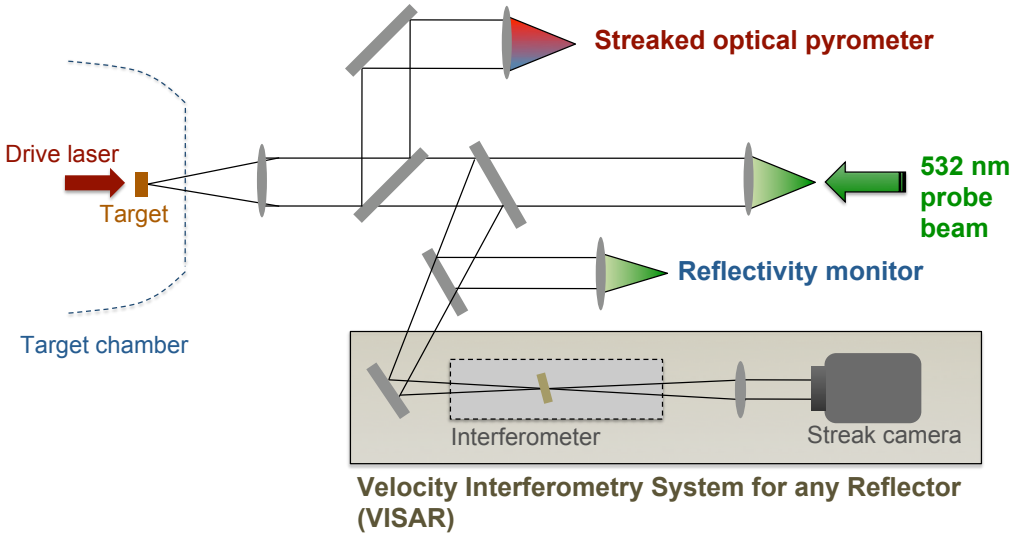

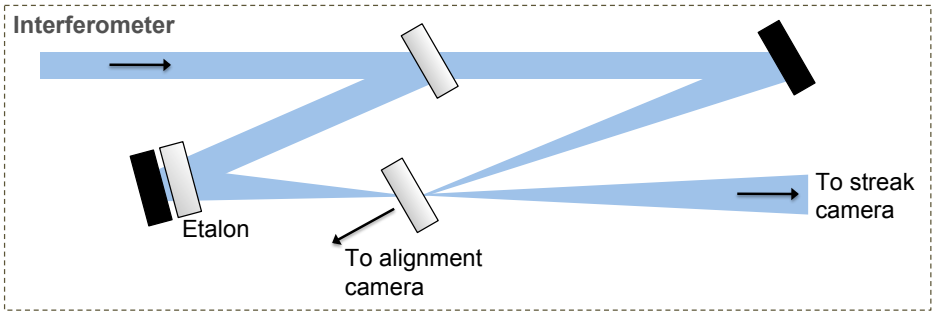

Figure 3.8: The Janus optical diagnostics for shock compression. Top: Schematic of the diagnostic layout. Bottom: Details of one interferometer stage; the full VISAR diagnostic incorporates two identical interferometers. Adapted from [96].

Chapter 4

X-ray scattering from shocked cryogenic D_2

In this chapter I present the results of x-ray scattering measurements on cryogenic deuterium shock-compressed with laser irradiation. Because of its fundamental importance as a fusion fuel, its central role in the structure of giant planets and its surprisingly complex phase diagram, hydrogen and its isotopes have been one of the canonical systems in both theoretical and experimental studies of shocked matter. A great deal of progress has been made in understanding high pressure hydrogen using velocity interferometry to measure equation of state and reflectivity [26, 25, 29]. However, the transition from insulating liquid to metal remains of central interest [98]. The measurements presented here were fielded with two goals. The first was demonstration of the feasibility of performing XRTS from cryogenic targets. The second was to apply the diagnostic to a problem of broad interest to the field by directly measuring the ionization as a function of compression. Since accurately determining ionization requires an accurate knowledge of mass density, we performed simultaneous VISAR measurements to determine the shock velocity in the target. Thus, this is also one of the first experiments to combine VISAR with XRTS on a single shot.

The experiments were performed at the Janus laser at Lawrence Livermore National Laboratory for three reasons. Shock-compression requires nanosecond length pulses, which Janus provides. Experiments in hydrogen require cryogenic targets, greatly reducing the shot rate and requiring more hands-on engineering in the chamber. Janus, a moderately sized facility, allows for day-to-day experimental changes based on results of early measurements. Finally, unlike the Titan laser, it is also home to an existing

cryostat designed for the target chamber.

Performing XRTS measurements on cryogenic liquid targets required developing a new thermal x-ray source and target platform as well as the spectrometer housing explained in Chapter 3. Those designs are outlined in the following sections. Then I present velocity measurements and x-ray scattering results. Finally I discuss the measurements in the context of several theoretical models.

Like most studies of high pressure hydrogen, we perform experiments on the heavier isotope deuterium. The physics of deuterium is essentially identical to hydrogen but it can be shocked to higher pressure thanks to its higher mass density, since its shock impedance is closer to the solid density pushers that the shock is launched through. Since the shock dynamics depend on the initial target state, comparison to pure hydrogen is made by scaling the initial density.

4.1 Target design

X-ray source

[1]Accurate measurements using x-ray scattering impose stringent requirements on the radiation source. In particular, for plasmon measurements, probe bandwidths must be $dE/E < 3 \times 10^{-3}$ and have peak to satellite ratios better than 10, particularly on the low energy wing [12]. This is necessary to descriminate elastic and inelastic components and accurately fit the downshifted plasmon feature. In the Compton regime, $dE/E \sim 10^{-2}$ and $E_{Compton} \sim E^2 \sin^2(\theta/2) > E_0 - E_{sat}$ is needed to differentiate between inelastic scattering and satellites located at E_{sat}. Previous experiments using long-pulse laser pumped backlighters have employed the Chlorine Ly-α transition at 2.9 keV [13]. However, weakly shocked deuterium has mass densities several times smaller than the solid density targets studied in previous experiments with Chlorine. At fractional ionizations, the plasmon shift is smaller and the screening lengtn iIn order to achieve collective conditions at fractional ionizations, we have developed the 2005 eV Si Ly-α resonance line as our x-ray probe. For typical conditions of 3× compression and average ionization of 0.2, scattering angles of 45° and 135° produce scattering parameters of $\alpha = 1.6$ and $\alpha = 0.65$. Thus, this 2 keV probe allows electron plasma waves to be observed at the low electron densities characteristic of the early stages of pressure

[1]Material in this section reprinted with permission from P. Davis *et al.*, Journal of Instrumentation **7**, P02004 (2012).

ionization. In addition, we observe fewer low-energy spectral features compared to the Chlorine line, which is advantageous for accurate determination of the inelastic feature.

Experimental design and source shielding is greatly simplified if the x-ray probe foil is transparent to the source radiation, since using the x-rays in transmission lets the foil act as a natural barrier between the emitting plasma and the target, helping to localize the radiation. Pure crystal silicon has an attenuation length of 1.56 μm at 2 keV, and is difficult to produce at micron scale thicknesses, making it challenging to use in transmission. Instead, we employ Si_3N_4 film, which is commercially available in sub-micron thicknesses. The 1 μm thick, 500 μm square film window is mounted in a 3 mm frame of pure silicon.

We characterize the Si Ly-α $2p-1s$ line using a similar approach as in [99], where a frequency doubled pump laser was shown to give optimally efficient x-ray production. In our case, a 1 ns, 527 nm, 200 J laser pulse irradiated the free standing silicon nitride film; by defocusing and using a 300 μm phase plate, nominal spot sizes between 100 and 500 μm were produced. A flat, 24mm square, ZYB grade highly oriented pyrolytic graphite (HOPG) (General Ceramics) crystal was used in mosaic focusing mode [91] to spectrally disperse the resulting x-ray emission. The detector was a Fuji BAS-TR025 image plate (IP). We tested x-ray production in both forward and backscattering modes, finding little variation in emission when a moderate laser spot size was focused on the center of the target.

The digitization process for these image plates results in photon intensity given in units of photostimulated luminenscence (PSL), which is calibrated to incident photon energy. We compute the conversion efficiency of laser energy into the Ly-α line as

$$\eta_{Ly-\alpha} = \frac{h \int I(\omega) d\omega}{\psi_{TR} \Omega_{det} E_{laser}}$$

where the integral covers the spectral width of the probe line, $I(\omega)$ is the intensity profile in the dispersive direction, h is the spatial extent of the signal in the non-dispersive direction, ψ_{TR} is the energy-PSL calibration factor and E_{laser} is the incident laser energy. $\Omega_{det} = \frac{rh}{4\pi d}$ is the solid angle of the detector, where d is the source-crystal distance and r, the integrated reflectivity of the HOPG crystal, has been previously characterized [89]. For energy conversion, we use the IP response outlines in Equation 3.6 and Table 3.1.

Measured conversion efficiencies are plotted in Figure 4.1 along with conversion efficiency measurements previously made using a Chlorine probe [99]; photon production compares favorably with these values. The trend toward lower efficiency at higher

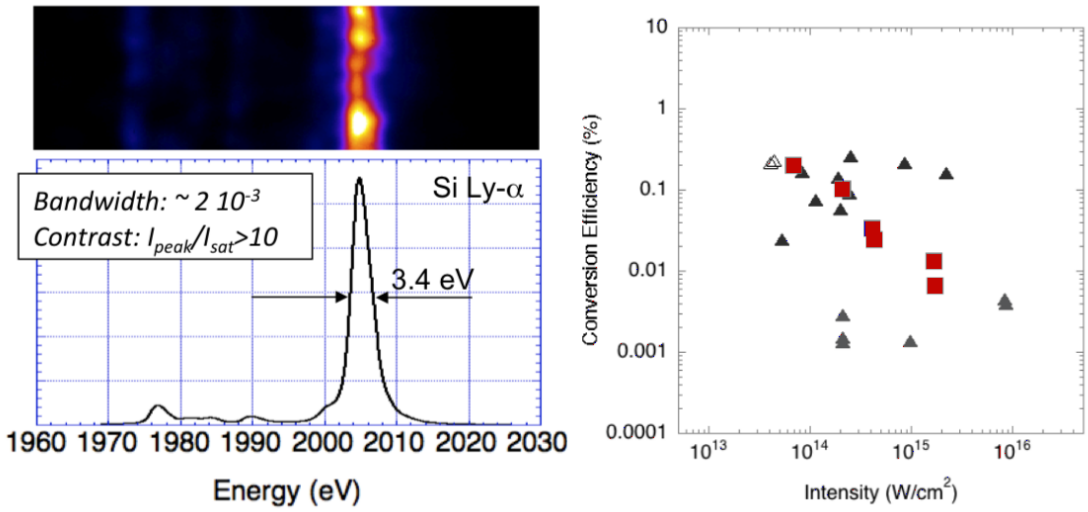

Figure 4.1: The Si Si Ly-α x-ray source. Left: Experimental backlighter spectrum and lineout. Right: Conversion efficiency for Si Ly-α (red squares) plotted with previous measurements of Cl Ly-α at 1ω (light triangles) and 2ω (dark triangles) reported in [99]

intensities is due to burn-through of the Si_3N_4 window. At larger spot sizes, x-ray production is enhanced by additional Ly-α emission from the Si window frame. Peak x-ray production into the Ly-α line is about 0.2 %, which is comparable to previous measurements. The bandwidth of the resonance is 2×10^{-3}; peak-to-satellite ratios are about 11:1. The two most prominent satellites on the low-energy side of the resonance are located 5 and 28 eV below the primary line whereas expected plasmon shifts for this system range between 5 and 20 eV, depending on compression and ionization. At 135 degree backscatter, the Compton shift is 13.3 eV. Thus, this line is well suited as an x-ray Thomson scattering probe for both collective and non-collective measurements.

Deuterium Vessel

The target consists of a 2 mm diameter cylindrical reservoir bored into a copper block, mounted in a configuration illustrated in Figure 4.2. The target block is fixed to a copper mount which is connected by a copper braid to a cryostat mounted on a vacuum flange on the top of the target chamber. Liquid helium flow at the cryostat

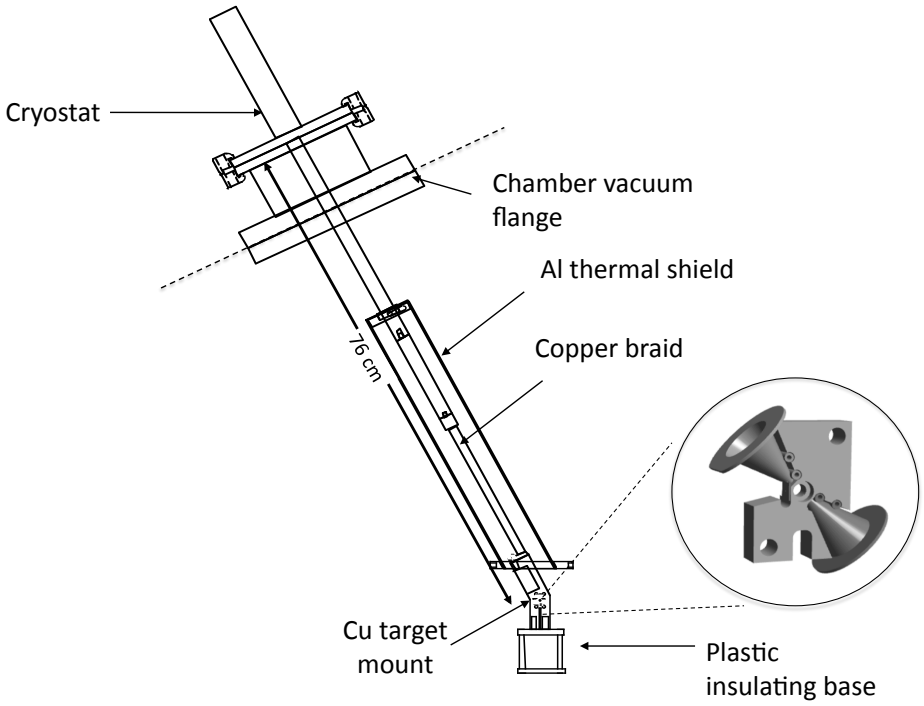

Figure 4.2: Schematic of target mounting apparatus as it sits in the vacuum chamber. The target detailed in Figure 4.3 is mounted to an insulated copper assembly, which is cooled by a cryostat fixed to the chamber.

cools the target conductively through the braid. The copper braid is shielded with an aluminum casing and several layers of insulation to minimize radiative heating. It is mounted to an optical positioning stage through an insulating plastic base, allowing fine translation and rotational alignment without significant additional heat sinks.

The target is designed for a shock to be launched along the axis of the cylinder, then probed perpendicularly with x-ray scattering and from the back with velocimetry. The front opening of the target, seen in Figure 4.3, is sealed with a pusher consisting

of a 40 μm Al disk coated with 12 μm of CH. The drive beam is incident on the CH surface of this pusher, launching a shock into the aluminum that releases into the deuterium bulk, compressing it to several times liquid density. The aluminum layer prevents x-ray radiation produced by the ablated plastic from reaching and pre-heating the deuterium. The opposite end of the cylinder is sealed with 130 μm thick quartz; this transparent window allows the VISAR probe to enter the target. It is tilted slightly to avoid unwanted reflections interfering with those from the shock itself. Three 400 μm holes are bored perpendicular to the cylindrical axis. These act as x-ray entrance and exit windows. They are covered with 1.5 μm mylar layers to vacuum seal the target. The window in the horizontal plane is additionally covered with a 500 nm Si_3N_4 x-ray source foil. The incident source beam creates a hot Si blowoff plasma, and the resulting Ly-α radiation travels through the mylar window, scattering from the shocked deuterium volume. The windows at 45° (forward scattering) and 135° (backward scattering) to the source are apertures for scattering diagnostics that probe collective and non-collective conditions respectively. $F/0.8$ plastic cones coated with 50 μm of Nickel are mounted on these x-ray exit ports to provide a shield from direct line-of-sight from background noise produced by blow-off plasmas from both drive and source beams. By collecting scattered x-rays from both ports as well as VISAR data on a single shot, this platform can provide a simultaneous single-shot measurement of density, temperature and shock velocity.

The deuterium gas is fed into the target through a 500 μm diameter tube. A Cernox CX-1070 temperature sensor is located in the base of the target mount assembly adjacent to the deuterium cell. This provides an indication of when the phase transition has been reached and also serves as the temperature monitor for the thermal control loop. As the target cools below the liquid transition point, the target reservoir fills with liquid and the remaining gas bubbles out. Since the VISAR diagnostic also provides a real-time view of the target volume through the rear window, this transition can be clearly observed, and confirmed by a rapid drop in pressure.

The gas-liquid transition in deuterium occurs at 20 K and the liquid-solid transition at about 17.5 K at typical backing pressures of 220 Torr. A time history of the target cooling cycle is shown in Figure 4.4, which shows that a temperature gradient of about 7K exists between the cryostat and the target volume at equilibrium. The sharp change in cooling rate is due to the thermal variation in the heat capacity of the copper: below the Debye temperature, the system cools much more quickly. The target is maintained at a temperature above the oxygen melt point until shot time, to minimize ice buildup on the target. Proportional-integral-derivative (PID) control is used to maintain the

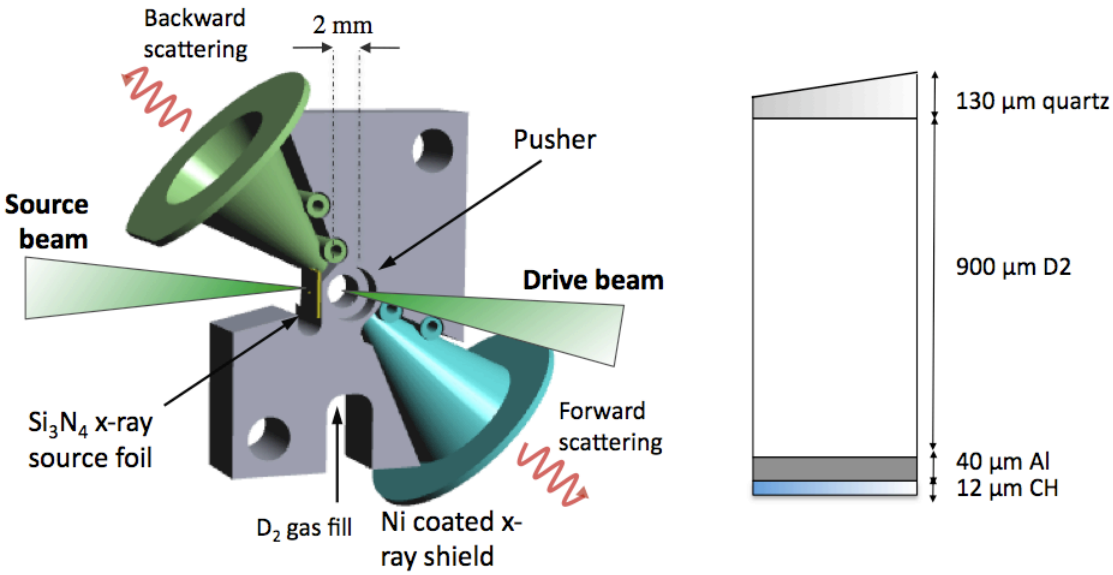

Figure 4.3: Deuterium target, showing backlighter and drive beam positions and x-ray access ports. This target is mounted to the assembly shown in Figure 4.2. On the right, a schematic cross section shows pusher, liquid deuterium and rear diagnostic window.

target at liquid conditions prior to a laser shot; gains are tuned to maintain target temperature to within 0.1 K at shot time. A Firerod cartridge heater installed in the base of the target is operated at 5W to provide the necessary temperature source to complete the control loop. Additionally, at higher power settings this heater can be used to heat the target to room temperature after the shot, minimizing condensation during target chamber venting. With this system in place, a two hour shot cycle can be achieved.

System characterization

The throughput of the system was tested by scattering from a liquid target. In this case, we used one arm of the frequency doubled Janus laser to pump the x-ray source at 2005 eV; the beam was defocused to a 400 μm spot size, resulting in an intensity of 1×10^{14} W/cm^2 and producing about 10^{15} 2 keV photons at the foil. We observed

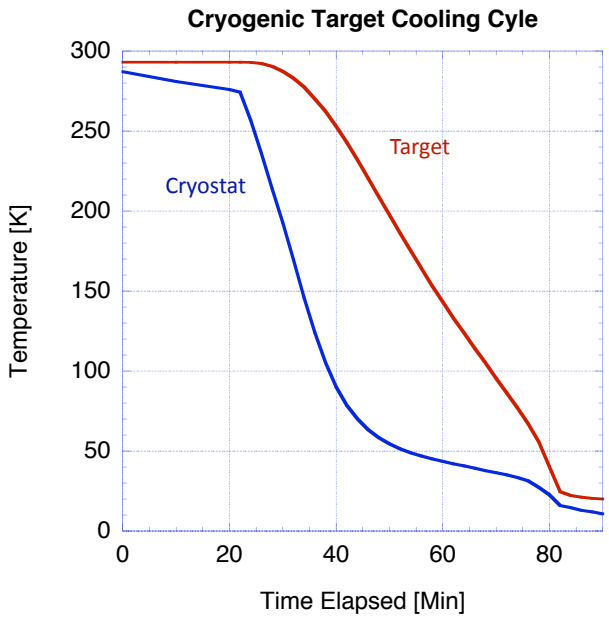

Figure 4.4: Evolution of cryostat and target temperatures during the cooling cycle.

scattering using the x-ray window and spectrometer at 45° in the forward direction. The raw spectrum is shown in Figure 4.5. This raw scattering signal shows a continuum background level of about 0.15 PSL with RMS noise of 0.03 PSL, largely due to leakage of undiffracted radiation. The intensity of the elastically scattered signal registers as 0.14 PSL, providing a clearly detectable and easily fit feature.

We can estimate the number of photons at the detector, $N_{ph,d}$ by accounting for the efficiency at each phase of the scattering process [3]:

$$N_{ph,d} = \left(\frac{E_L}{h\nu}\eta_x\right)\left(\frac{\Omega_{Tar}}{4\pi}\eta_{att}\right)\left(\frac{n_e\sigma_{Th}x}{(1+\alpha)^2}\right)\left(\frac{\Omega_{Det}}{4\pi}R_{xtal}\eta_d\right) \tag{4.1}$$

where E_L is the incident laser energy, Ω_{Tar} and Ω_{det} are the solid angle subtended by the target with the x-ray probe and by the detector with the target, respectively. η_x is the conversion efficiency of laser energy into x-rays; η_{att} corresponds to x-ray

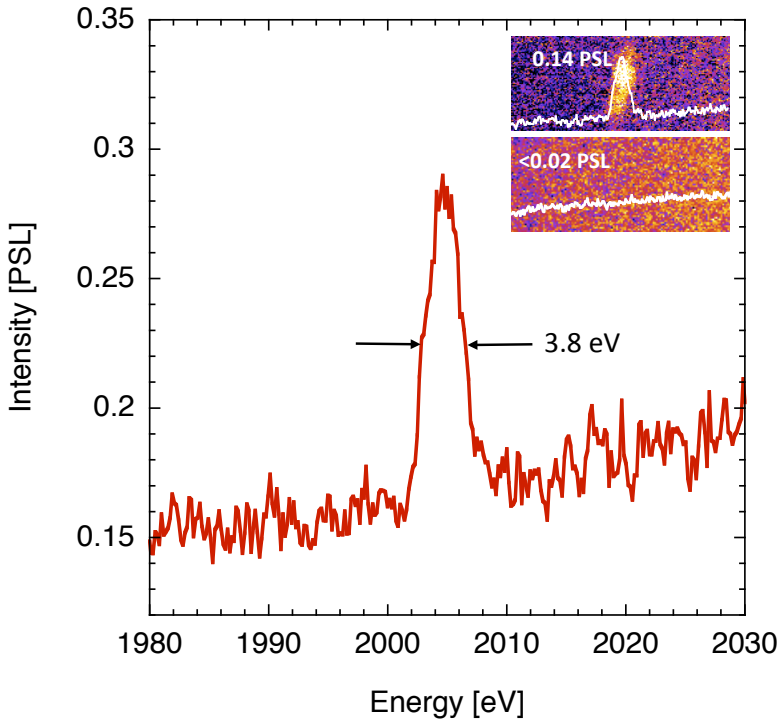

Figure 4.5: Measured 2005 eV x-rays forward scattered from cryogenic liquid deuterium. Instrument resolution is less than 4 eV, and throughput is sufficient for accurate inelastic scattering measurements. Also shown are raw images corresponding to the scattering measurement from deuterium (upper inset) and an identical measurement from an empty target (lower inset), which confirms the lack of a spurious scattering signal.

absorption by the target; η_d is the detector efficiency and R_{xtal} is the integrated crystal reflectivity. The term $(1+\alpha)^{-2}$ applies for inelastic scattering, and $n_e\sigma_{th}l$ is the total scattering fraction from the target, given the Thomson cross section σ_{Th} and a target scale length x.

Assuming liquid density and a 1 mm deep scattering length, we expect a scattering fraction of approximately $n_e\sigma_{Th}x = 5\times10^{-3}$, where x is the scale length over which scattering occurs. The composite detector solid angle and integrated crystal reflectivity $\Omega_{Det}R_{xtal} = 1\times10^{-5}$ and the source-target solid angle is $\Omega_{Tar} = 0.03$. This translates into an expected signal of 3×10^4 photons, or about 0.16 PSL, consistent with our observation. Repeating the scattering shot with an empty cell shows only continuum noise (shown in the inset), confirming that we do not detect stray light scattered from the target itself.

The spectral resolution of the forward scattering spectrometer and source line is measured to be a gaussian profile of 3.8 eV at FWHM. This is sufficiently high to allow precise measurements of plasmon positions at even low ionization fractions of 0.1 in weakly compressed hydrogen.

4.2 Experiment

Scattering measurements on shocked deuterium proceeded with a similar chamber layout. A single laser beam drove a shock into the deuterium with intensities of up to 4×10^{13} W/cm^2 at the target in 2-6 ns long pulses. In one set of experiments, a 527 nm, 2 ns pulse was used with forward scattering to observe low ionizations. To reach higher targets pressures, a 1054 nm drive beam was used at 4 and 6 ns pulse lengths, shorter probe delay times and thinner pushers. The laser was incident on a CH-coated aluminum pusher ranging from 12-40 μm, which coupled the shock into the D_2 but shielded the target from x-rays and energetic electrons produced by the laser-target interactions discussed in Chapter 2.

A second 527 nm beam was propagated at 90° to the drive beam, incident on the Si_3N_4 foil. The probe pulse was delayed 10-20 ns after the rise of the drive beam, allowing the shock to traverse a distance of 350 μm to reach the volume accessed by the x-ray diagnostic port. A schematic of the timing arrangement is shown in Figure 4.7 with traces taken from optical diodes monitoring the beams as they enter the chamber. Figure 4.7 shows a 2D hydrodynamic calculation from the HYDRA code illustrating the shock front propagation as a function of time. As the lineout suggests, one advantage

of probing at least 10 ns after the drive beam is that the pusher separates from the D_2 shock over time, reducing the likelihood of scattering from the much higher density aluminum.

We measured the shock velocity with VISAR simultaneously with x-ray scattering. Given the observed shock velocity, we can extract a continuous history of compression ρ/ρ_0 using a deuterium equation of state. While the EOS of hydrogen has been extensively studied, there is still considerable uncertainty, particularly at maximum compression. The experimental data points and several theoretical treatments are summarized in [29]. While disagreement between EOS models is relatively small where we observe the onset of ionization in the pressure regime below 30 GPa, we note that the widely used stiff Sesame tables and softer quantum molecular dynamics models generally bound the results in the pressure regime of interest here. The quotidian equation of state (qEOS) model of More et al [100] falls between these limiting cases, and we use it here in our hydrodynamic simulations and, for consistency, to extract pressure and mass density from the VISAR measurements.

Figure 4.8 shows a VISAR streak record along with the extracted shock velocities and pressures. Radiation-hydrodynamic simulation results from the HYDRA code [101] are also shown, accurately reproducing the measured shock velocity. Stray light from the drive beam is visible for 2 ns early in the streak. Shock breakout from Al into D_2 occurs near the end of the drive beam where a discontinuous fringe shift is visible. As the shock decays, a drop in signal amplitude is visible in the raw data, since reflectivity falls as shock pressure and ionization decrease. The peak velocity immediately following shock breakout from the pusher is 22 km/s with pressures near 50 GPa, which decays to 13.8±1 km/s and 26.5+3.5/-4.5 GPa at 21 ns, the center of the 2 ns long x-ray probe.

One of the primary problems in simulating laser-produced shocks is knowing precisely the spot size and intensity profile incident on the target. That problem is mitigated here by varying the incident pulse profile to match the velocity history produced in the measured VISAR data. Then, on shots where no VISAR data were taken, the same profile can be used to extrapolate the shock performance by scaling hydrodynamic simulations to the relevant laser energy and pulse length. Two examples of this are shown in Figure 4.9 for two shots made at 1ω with pulse lengths of 4 ns and 6 ns respectively. The mass density is shown as a function of space for a series of times slices in 1 ns increments. We note that although the 6 ns case produces significantly higher compressions early in time, by 15 ns after the drive beam, the two shots have decayed to very similar mass densities. This late time decay trend means that the primary way

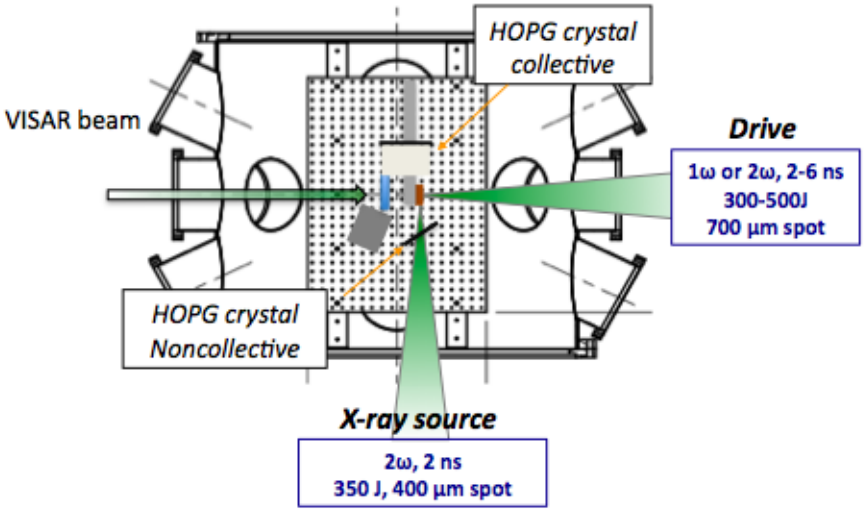

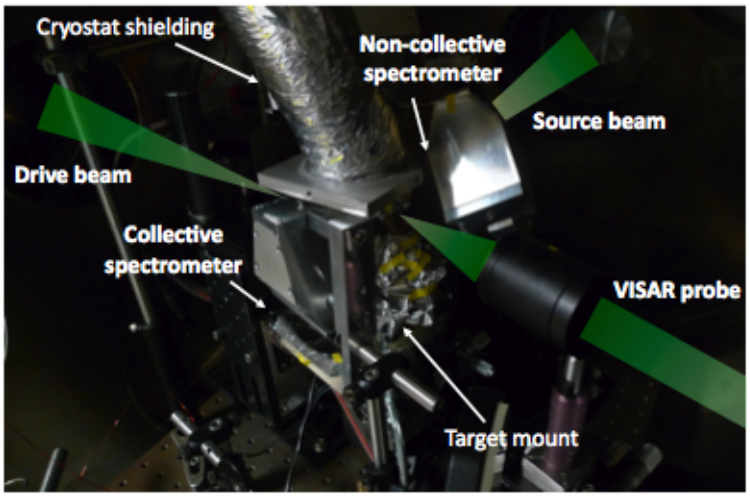

Figure 4.6: Chamber configuration. Top: A schematic layout of the target chamber for cryogenic scattering experiments. Bottom: A photograph showing the inside of the chamber.

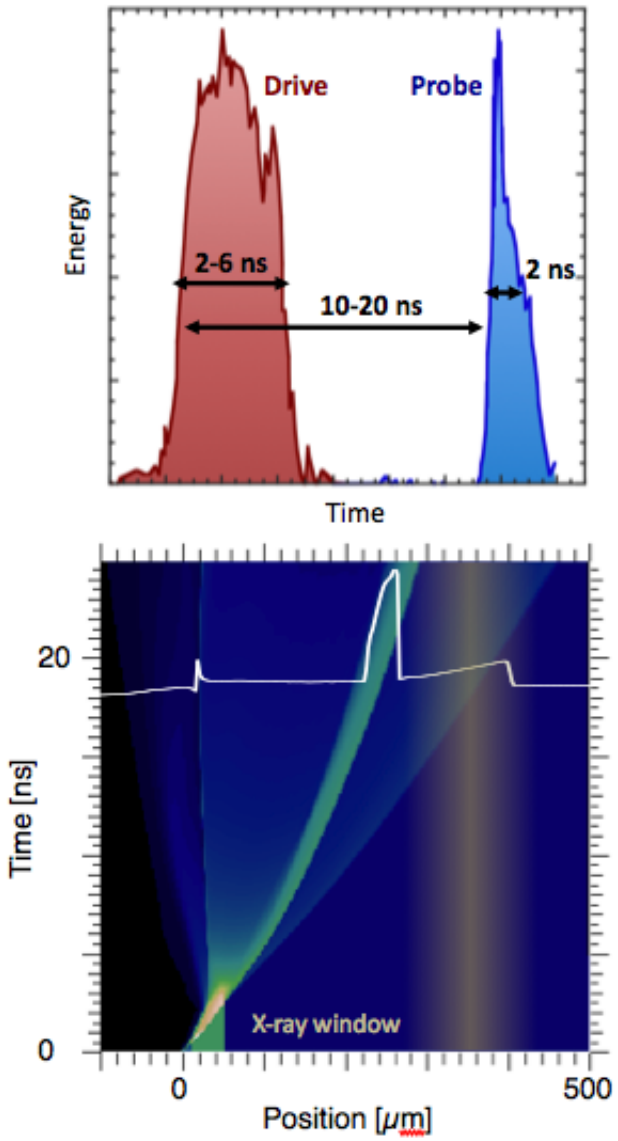

Figure 4.7: The experiment is timed to allow the shock front to reach the x-ray probe window. Top: Photodiode traces of the shock and probe pulses illustrating their temporal relationship. Bottom: A two dimensional hydrodynamic calculation of the deuterium shock propagation using the code HYDRA. The x-ray probe window is overlaid. The lineout corresponds to the 20 ns probe delay. The higher density profile behind the deuterium shock is the remnant of the Al pusher, effectively shielded from x-rays.

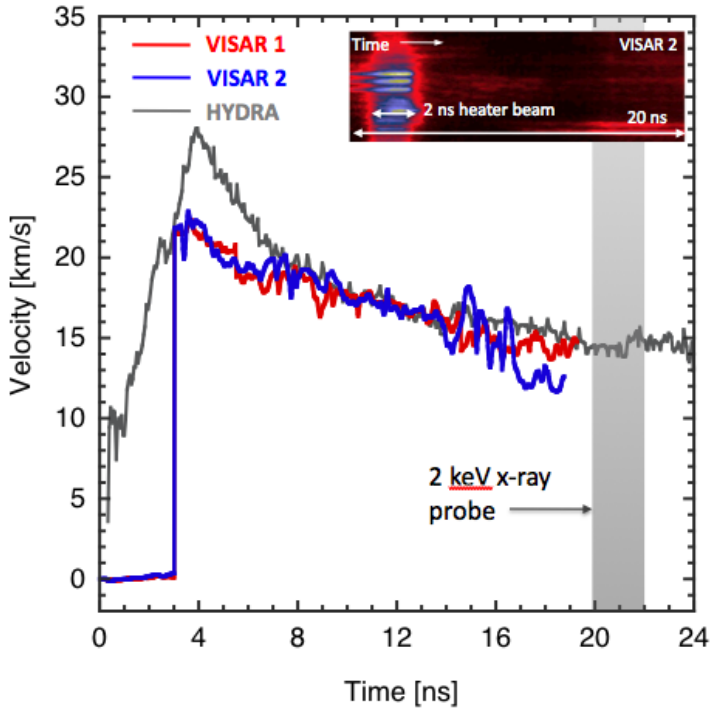

Figure 4.8: VISAR time history of shock velocity for the same shot as the plasmon measurement. Two curves are measured at different sensitivities to unfold the 2π phase uncertainty. A calculation of the shock velocity using the HYDRA code is also shown. Inset: One of the streak images.

of making high pressure measurements on this target platform is by using long drive pulses to create fast shocks and measuring as early in time as possible, provided the shock front has reached the x-ray diagnostic window. This was the approach to the highest compression measurement made. However, it also suffers from greater signal to noise, since less of the shock is available to scatter from.

We perform x-ray scattering at two angles, observing the electron-electron (plasmon) resonances in the ionized system at a small angle and probe the electron distribution at a larger angle. For this Fermi-degenerate system, this produces two independent measurements of free electron density as well as providing an indication of electron temperature in the long-k limit where it is possible to accurately compute the

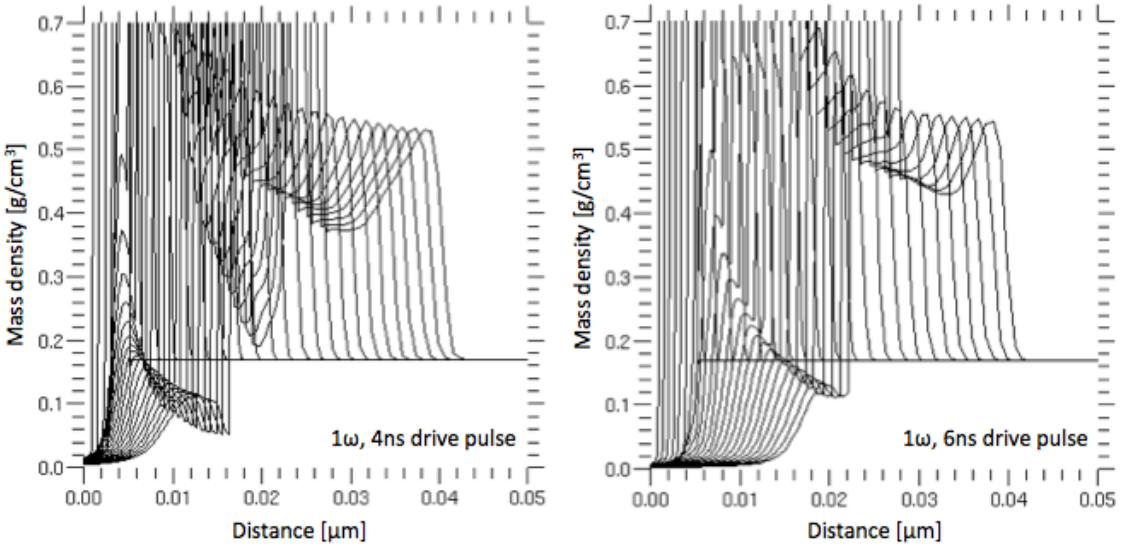

Figure 4.9: Hydrodynamic calculations of mass density from HYDRA for 1 ns time slices up to 25 ns after the start of the drive beam. Two 1ω pulse lengths are shown - the shock decays to very similar mass densities late in term regardless of early time pulse length.

ion structure at low ionization. The probe energy and experimental geometry define the probed k-vector according to $k = |\mathbf{k}| = 4\pi\frac{E_0}{hc}\sin(\theta/2)$. Our experiments probe density fluctuations at scale lengths of $k = 7.78 \times 10^9$ m^{-1} in the forward direction and 1.88×10^{10} m^{-1} in the backward direction, leading to scattering parameters of $\alpha = 1/k\lambda_S = 1.52$ and $\alpha = 0.7$ respectively for the x-ray spectra shown. Here, λ_S represents the screening length in the plasma; the forward scattering vector extends over several screening lengths and thus provides collective scattering conditions at even small ionization fractions, while the backward scattering vector is sufficiently long to probe at a scale length smaller than the screening length of the plasma at moderate ionization, observing the individual particle motion of the electrons.

Figure 4.10 shows x-ray scattering spectra from two forward scattering shots; the upper spectrum is taken from the same shot as Figure 4.8, with shock pressures of 26.5 GPa and a compression of 3.18 at the time of x-ray probing. The downshifted plasmon is centered at 1998 eV below the probe energy of E_0=2005 eV. The plasmon reso-

nance in this low-temperature regime experiences very little Landau damping, and is therefore quite narrow. The fits shown include broadening due to collisional effects calculated in the local-field-corrected Born-Mermin approximation and convolution with the instrument function introduced by the HOPG crystal and detector. The measured electron density corresponds to a Fermi temperature of T_F=3.1 eV. At temperatures of less than an electron volt, the plasma screening length is the Thomas-Fermi length, and the scattering parameter is $\alpha = 1/k\lambda_S \approx 1/k\lambda_{TF} = 1.5$. A best fit to the data indicate a free electron density of $n_e = 2.5 \pm 0.38 \times 10^{22}$ cm^{-3}, where the uncertainty is due mostly to noise. Combined with a mass density from the velocity interferometry, this corresponds to an average ionization state of $Z = 0.15$.

The lower spectrum is from a slightly lower compression shot. In this case the shock pressure was low enough that the target never became reflective and a VISAR measurement was not possible. It is not surprising that no plasmon resonance is visible in this shot - it has not reached sufficient compression for electrons to become free. The compression for this shot was determined to be ρ/ρ_0 =2.8 from hydrodynamic calculations, although we note that a very similar number is obtained using the ablation pressure scaling in [73]. The upper limit on ionization comes from the level of background noise and the finite resolution of the spectrometer as Z $\leq$ 0.04.

Subsequent shots measured backscattering at 135°, an example of which is shown in Figures 4.11 and 4.12. This target was compressed with a 4 ns, 1054 nm pulse and probed at 15 ns delay. HYDRA calculations predict pressures of 28 GPa and compressions of 3.24. A best fit to the data gives electron densities of $n_e = 4.7 \times 10^{22} \pm$ 1.5 cm^{-3}, corresponding to an ionization state of Z=0.28. Fitting the intensity of the elastic feature with a screened one-component-plasma model [59] gives a temperature of T_e=0.4 eV. This doesn't provide a precise temperature value because the elastic scattering model is not sensitive to temperatures in excess of this one; however, it is consistent with quantum molecular dynamics simulations [102].

The broad low-energy tail of this spectrum is due to bound-free transitions, whose fit includes density and temperature dependent continuum lowering. With a backscattering Compton energy of 13.3 eV, most of the bound electrons in the D_2 liquid become available for bound-Compton scattering. The inelastic spectrum is therefore a Fermi distribution from the free electron superimposed on top of a bound-free feature. For the spectrum shown in Figure 4.11, the bound-free component makes up roughly half the total inelastic scattering intensity. This is illustrated, overlaid with the total scattering spectrum, in Figure 4.13.

In Figure 4.14, we summarize measurements of ionization across several shock-drive

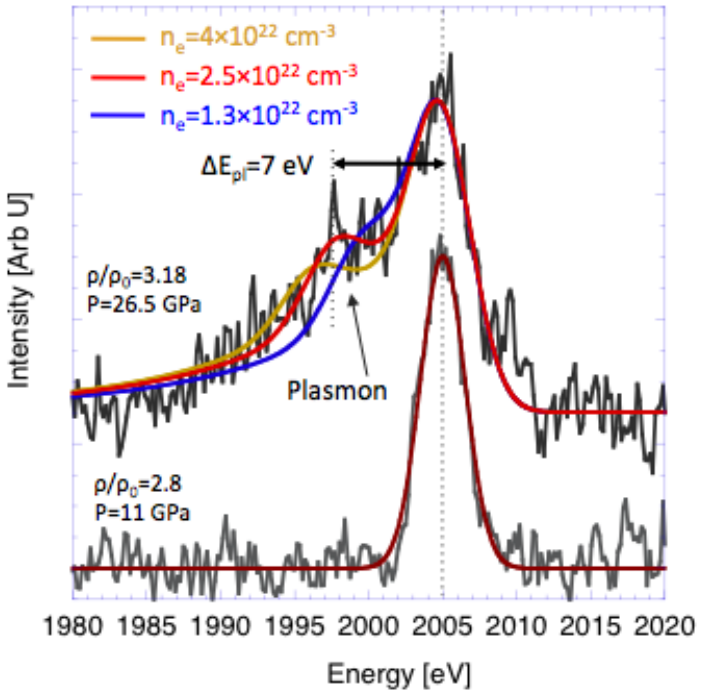

Figure 4.10: Plasmon spectrum for high and low compression. The presence of free electrons is apparent in the redshifted plasmon feature at compressions of 3.18 but not in the spectra measured for a compression of 2.8.

and probe delay conditions. The data are taken at compressions between 2.8 and 4.05. Measured ionization for both forward and backscattered configurations is shown as a function of compression, along with predicted ionizations from several models. Here the values of compression plotted for mass density of the backscattering measurements are determined using hydrodynamic calculations benchmarked to VISAR measurements.

There are two major sources of uncertainty in the compression values assigned to the data points. Except for the high compression plasmon measurement, the mass density is inferred from hydrodynamic calculations. We include an uncertainty in the laser spot profile by propagating a 20% uncertainty in drive intensity through test calculations to determine its effect on compression. However, most of the uncertainty comes from variation in possible choices of equation of state. Particularly at the highest compressions measured, there is disagreement on the hydrogen compressibility. This is

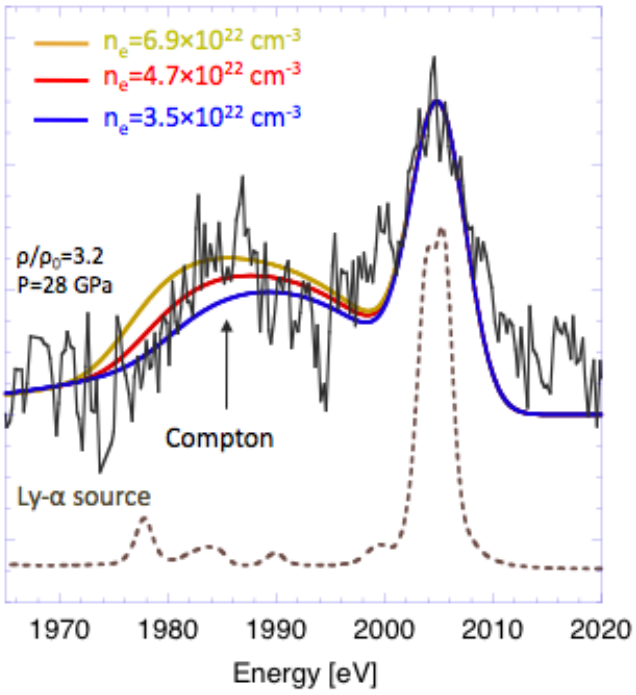

Figure 4.11: A backscattered spectrum showing the density dependence of the ratio of inelastic to elastic features, including several theoretical fits. Below the scattering data, the spectrum of the source is illustrated.

dealt with by including variation in mass density at a given pressure bounded by the hybrid EOS of Kerley[33] on the stiff side and the DFT-MD Hugoniot of [35] on the soft side. These two values added in quadrature determine the error bars along the compression axis. For the shot where shot velocity was measured directly, we combine the RMS noise in the late time data with the EOS uncertainty at the relevant pressure.

The data indicate a sharp onset of ionization between 3 and 3.5 times compression. Predictions from a Thomas-Fermi model shown in orange exhibit very little of the density dependence apparent in the data at low compression. In yellow we also show several points from the code FVT+, a chemical picture model used in planetary structure calculations [31] that predicts very low values of ionization for all pressures measured. Calculations using the model of an average atom embedded in a plasma

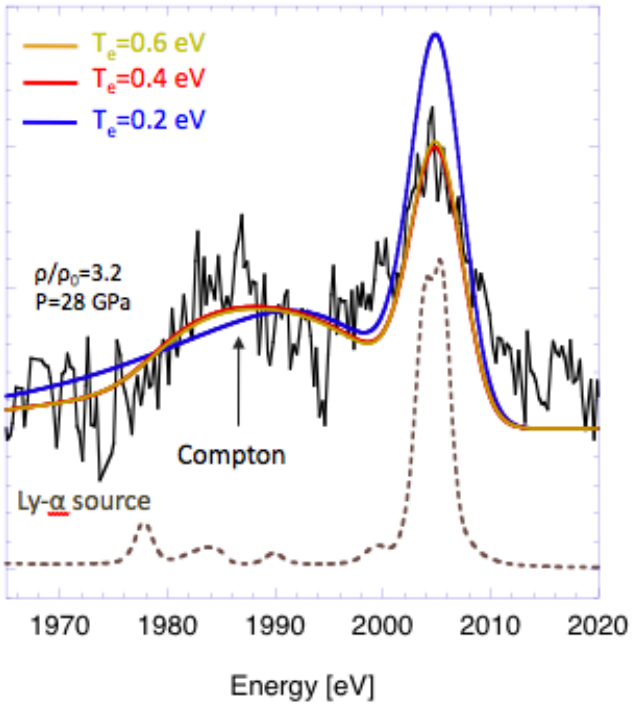

Figure 4.12: A backscattered spectrum showing the temperature dependence of the ratio of inelastic to elastic features, including several theoretical fits. As T_e increases, the data become less sensitive to temperature. Below, the source spectrum is shown again.

background [77] reproduce the shape of the ionization curve at a somewhat lower magnitude. Temperature variations in this calculation have little effect on the total ionized fraction in the target because pressure is the primary cause of ionization at these densities and temperatures. It is significant that this more sophisticated treatment of electrons captures more of the physics at work here. At the cusp of ionization, electrons are becoming delocalized from individual deuterium dimers. They may not properly be called free yet, but neither do they behave as fully bound. Of course, a chemical picture calculation that divides particles discretely into atoms and electrons is unable to treat this process continuously.

Finally, calculations of the fraction of dissociated D_2 dimers using an MD-DFT

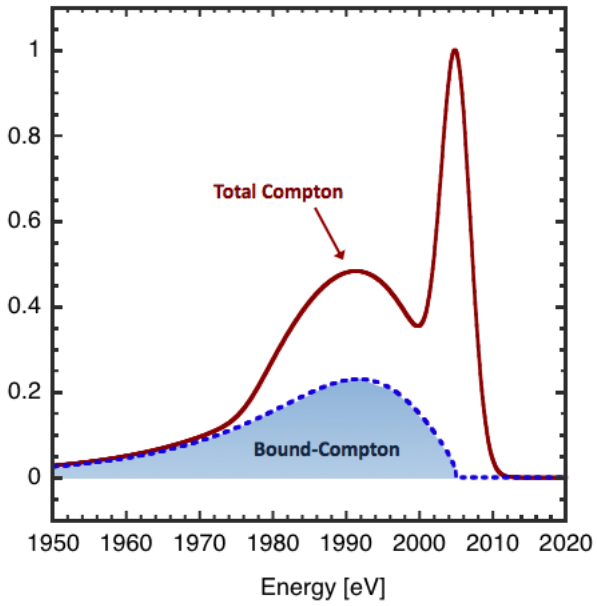

Figure 4.13: A simulated spectrum corresponding to the best fit shown for the backscattering data above with the component due to bound-free scattering highlighted.

model are shown in red on the same axis as the ionization data. These calculations were made by tracking neighboring ions through several vibron periods of a simulation. Ions remaining nearest neighbors past a threshold time were labeled molecules, while those that moved apart were labeled atoms. Beyond the approximate treatment of dissociation, these calculations are results scaled in mass from hydrogen to deuterium assuming identical physics between the two isotopes. Nevertheless, the dissociation curve agrees very well with the measured ionization values.

It therefore appears that as deuterium is compressed the processes of dissociation and ionization occur nearly simultaneously. This is intuitive, since as electrons become delocalized across many ions, they are no longer available for binding individual molecules. Moreover, these processes play a vital role in determining the path of the Hugoniot at moderate pressures where models currently disagree most strongly. By motivating and discriminating between theoretical models, these results will help provide for a more robust understanding of the behavior of compressed matter.

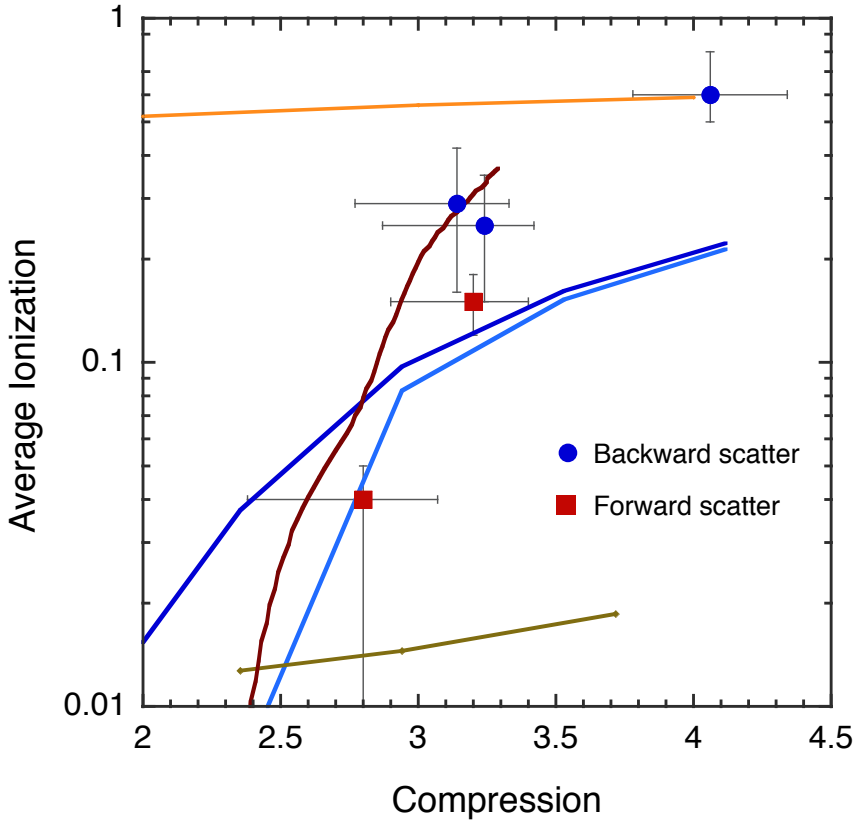

Figure 4.14: Ionization measured with x-ray scattering as a function of compression using both forward and backscattering. Theoretical calculations along the Hugoniot using the Thomas Fermi (orange), FVT+ (brown) show very little of the data's variation with pressure. Also shown are average atom calculations of ionization at temperatures of 0.5 eV (dark blue) and 0.1 eV (light blue). The dark red curve is the fraction of molecular dissociation calculated with density functional molecular dynamics, coinciding almost exactly with ionization.

Chapter 5

X-ray scattering from proton-heated matter

A second set of experiments were performed using a similar x-ray scattering technique to measure ionization in proton-heated matter using the laser-driven proton production mechanism described in Section 2.4. Because protons deposit energy volumetrically, this method of heating samples decouples temperature effects from pressure-induced ionization. Further, while isochoric heating has been implemented using laser drivers [42, 44], the energy deposition is limited to the optical skin depth of the sample. MeV protons deposit energy tens of microns into a typical solid, producing a sufficiently large to measure scattered x-rays from. Finally, since the protons are stopped by the electrons in the target, their energy deposition is nearly immediate and completely into the electron subsystem. Thus, proton-heating is a viable tool for studying electron-ion thermal relaxation [17].

Here we use x-ray scattering to measure the free electron population in two target materials, boron (B) and boron-nitride (BN). We find that for identical thermal conditions, ionization varies significantly between the two, a fact that is attributed to persistent band gaps at high temperature.

5.1 Experiment configuration

The experiments were performed at the Titan laser facility at LLNL using the configuration illustrated in Figure 5.1. Titans short pulse beam was generally used at a 10 ps pulse length, although test shots at 5 ps showed no difference in observables. The

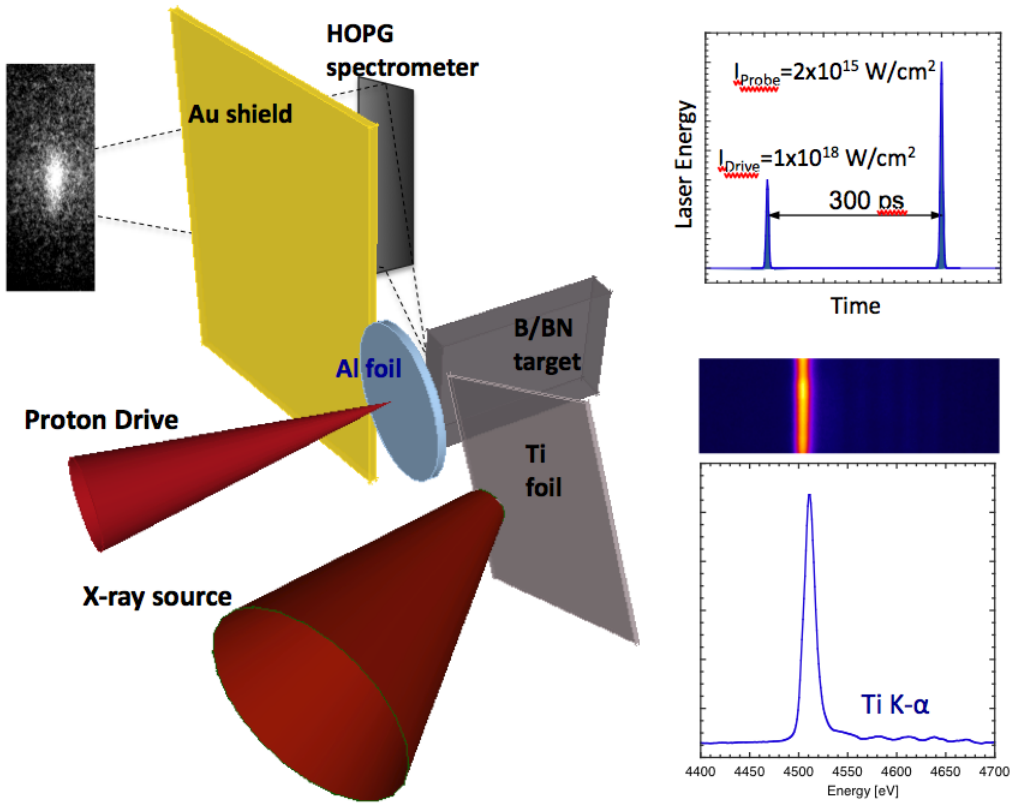

Figure 5.1: A schematic of the beam and target configuration in the proton-heating experiments. Also shown are illustrations of the relative timing of heater and source beams and the Titanium K-α spectrum.

beam was split to produce two beams in a pump-probe configuration, as described in Chapter 3. The proton source beam carried 60 J and was focused to a 40 μm Gaussian spot on a 10 μm thick Aluminum foil; this produced nominal intensities of 1×10^{18} W/cm^2. This pulse drove an intense TNSA proton beam through from the rear surface of the foil towards the target sample centered 200 μm downstream of the aluminum. The second beam was delayed by 300 ps relative to the heater pulse. It was focused to a 300 μm spot on a Titanium foil, creating a burst of K-α radiation at 4510 eV.

X-rays scattered by the target were collected with a cylindrically curved 70 x 25

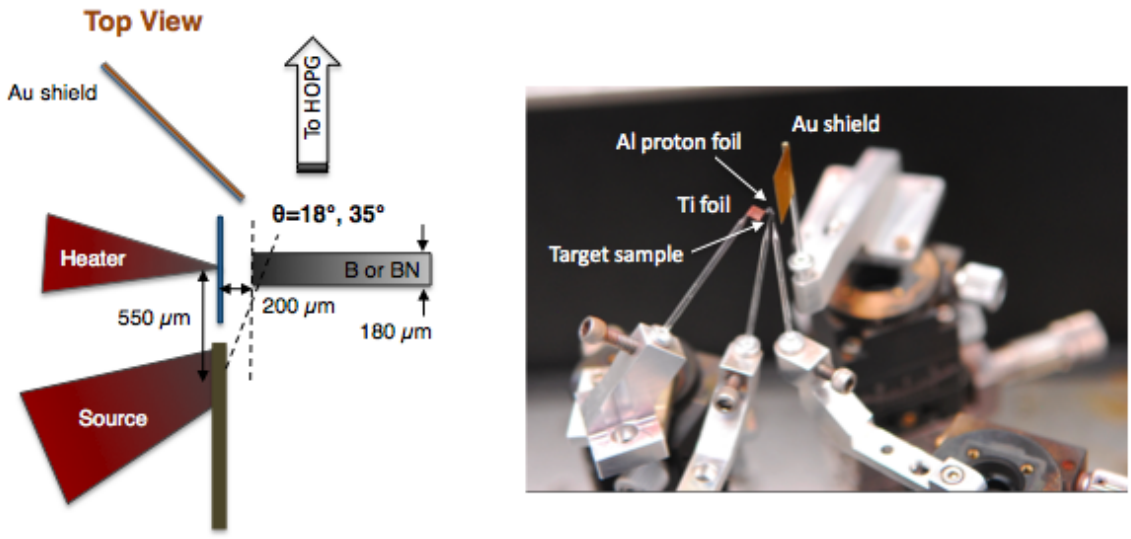

Figure 5.2: Target details. Left: A two dimensional schematic of the target arrangement with relative dimensions. Right: A fully assembled target showing the relationship between target elements and positioners.

mm^2 highly oriented pyrolitic graphite (HOPG) crystal spectrometer focused in a von Hamos configuration onto a Fujifilm MS-type imaging plate. The direct line of sight between the detector and the intense proton and x-ray sources was blocked with a 50 μm thick gold shield coated with a CH film to minimize emission induced by stray light and high energy particles. The arrangement of target elements and dimensions is shown in Figure 5.2 along with a photograph of an assembled target. The target consisted of proton source foil, x-ray source foil, B or BN sample and Au x-ray shield. Each element was mounted on a 6 degree of freedom translation stage allowing the target elements to be brought to the appropriate distances and angles while still allowing for variation during experiments.

The titanium K-α line has previously been characterized for x-ray scattering experiments [103, 14], so we have not performed the same level of calibration as we did in Silicon. However, we monitored the x-ray source intensity over the course of the experiment to ensure stable performance and found a conversion efficiency of laser into

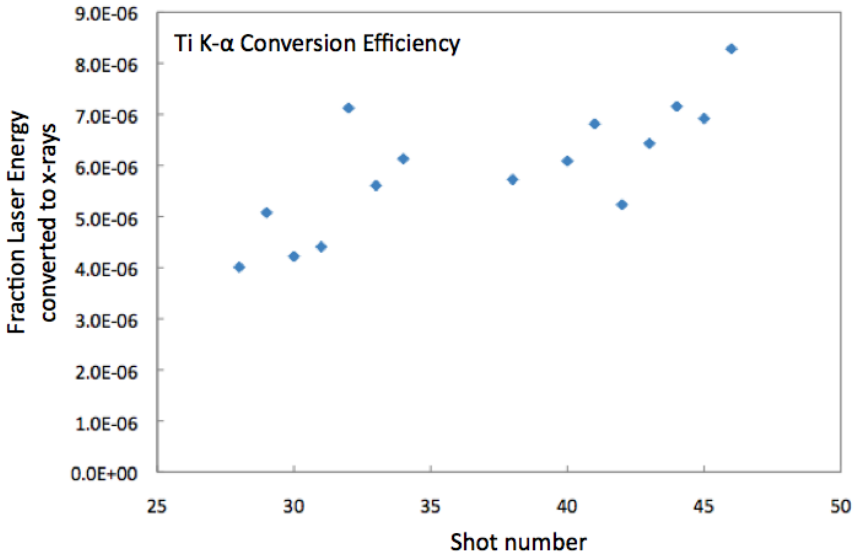

Figure 5.3: The conversion efficiency of the laser into the Ti K-α line over the course of the experiment.

the x-ray line of about 6×10^{-6} over the course of the study. This is about a factor of 2 less than reported previously, since less effort was made ot optimize the source for peak x-ray production. Nevertheless, we produce sufficient photons for a robust scattering signal. The conversion efficiency for the data-taking shots of the experiment is shown in Figure 5.3.

5.2 Target Characterization

The proton beam was characterized by placing radiochromic film (RCF) [104] and the magnetic proton spectrometer downstream of the proton foil. We measured a broad proton energy spectrum reaching past 5 MeV on axis, shown in Figure 5.4. By placing a wire mesh 1 mm downstream from the proton foil and imaging onto the RCF (shown as an inset in the figure), we measured the protons to be emitted in a 60 cone.

This proton spectrum is used as an input to the radiation-hydrodynamic package LASNEX [75]. Using well-known cold stopping power values for the targets we can compute the plasma parameters of the sample at probe time. The protons have char-

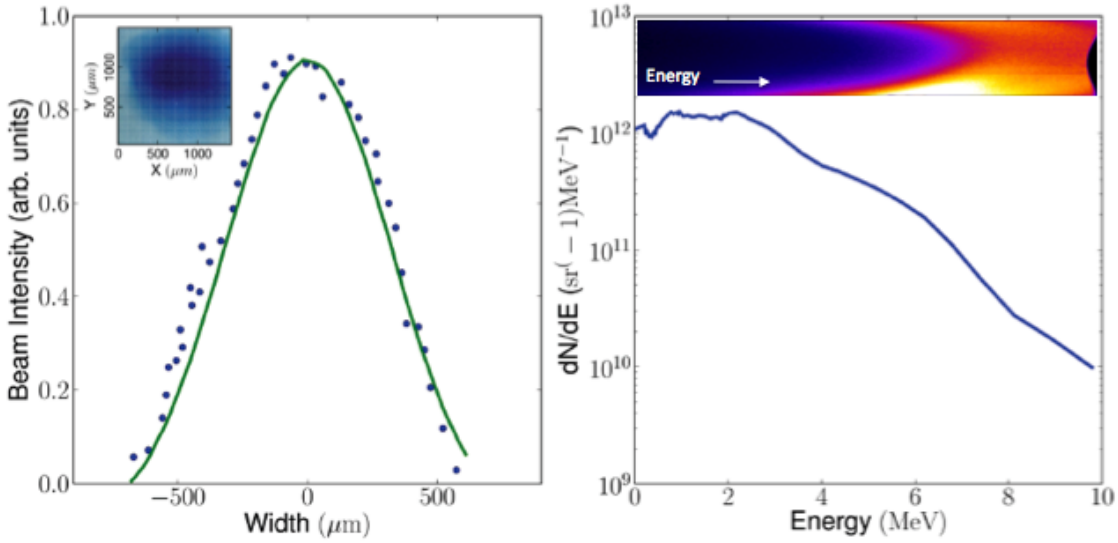

Figure 5.4: Measured proton characteristics. Left: Proton emission as a function of space, determined from imaging a wire grid onto radiochromic film. RCF exposure showing the grid image is shown in the inset. Right: A proton spectrum taken with the magnetic proton spectrometer.

acteristic ranges of about 20 μm in the target. Simulations show a peak temperature of 18 eV at this depth, dropping exponentially to 9 eV at 100 μm into the target. The front of the target is also somewhat cooler since only the low energy tail deposits energy there; while the front surface blowoff plasma is cooler than the bulk target, but is much lower density and thus contributes a negligible amount to the scattering signal.

LASNEX calculations of target temperature as a function of proton penetration depth are shown in Figure 5.5. In fact, two electron temperature profiles were calculated. A beam composed only of protons produced peak temperatures of 12 eV. Including carbon ions from hydrocarbon contamination on the proton foil results in higher temperatures.

An x-ray scattering spectrum taken at 18° is shown in the second panel of the same figure. This scattering angle results in a plasmon shift of about 12 eV, sufficiently small to observe detailed balance at temperatures in excess of 10 eV. The best fit shown is for 19 eV, but the error bars of ±5 eV are large here due to the low intensity of the upshifted plasmon feature. Nevertheless, this observation confirms that the target is

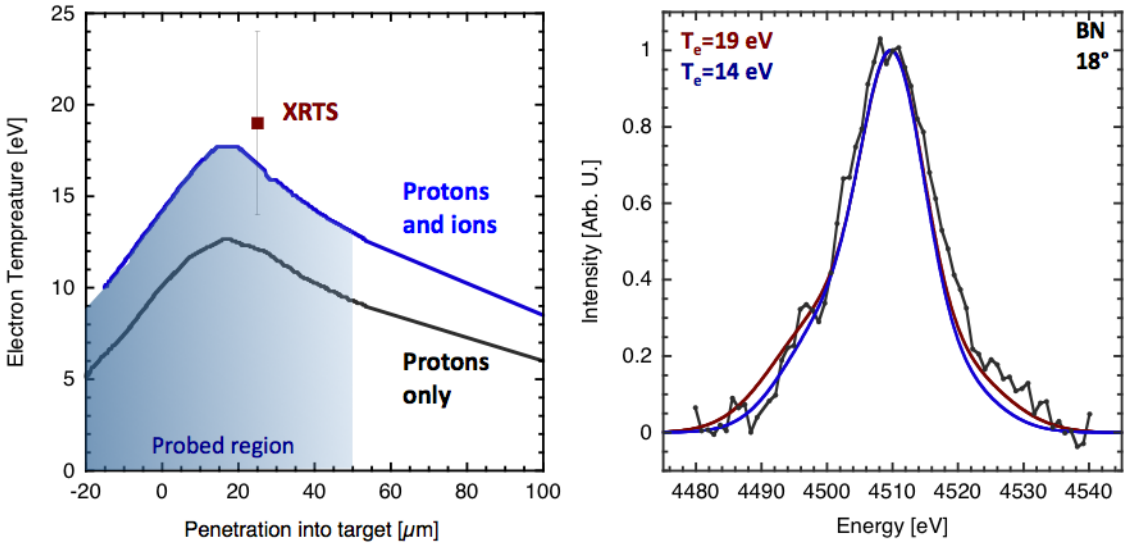

Figure 5.5: Proton heated BN temperature. Left: LASNEX simulations of the target temperature as a function of depth in the target. Right: Measured 18° x-ray scattering spectrum showing the upshifted plasmon due to detailed balance. A best fit of the ratio of inelastic features gives an electron temperature of 19 eV.

quite hot; we take an average target temperature across the probed region of 16 eV for the analysis of ionization. The lower temperature portion of the target does not contribute to the scattered signal because of the relatively high opacity of the target to 4.5 keV x-rays. The longer path length of x-rays scattering from deeper in the target results in higher absorption.

The target self-opacity is tested by placing a gold shield in front of the first 50 μm of the target. When this hot portion of the target is blocked, the detailed balance measurement disappears completely, leaving only residual elastic scattering from the cold part of the target. This is illustrated in Figure 5.6, where the elastic scattering components of each signal have been normalized. Since the analysis of ionization is based solely on the inelastic portion of the spectrum, the relative intensity of the ion scattering feature plays no role in the interpretation of the data.

The photometrics of this measurement can be calculated following the equation in

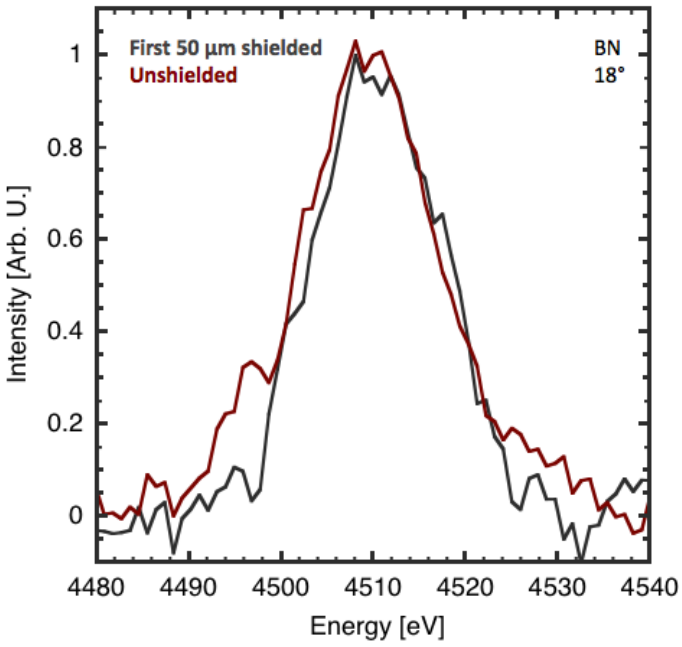

Figure 5.6: Scattering measurements taken from a fully unshielded target and one with the first 50 μm of the target blocked. The scattering diagnostic is only sensitive to the front portion of the target thanks to x-ray absorption deeper in the sample.

4.1. The target and detector occupy solid angles of $\Omega_{Tar} = 2\times10^{-2}$ and $\Omega_{Det} = 2\times10^{-5}$ respectively. This means that about 6×10^4 photons are expected at the detector, producing an estimated 0.1-0.2 PSL at the focus of the crystal on the image plate. This is consistent with the observed signal in scattering shots.

Calculations were also performed of the average target ionization. As seen in Figure 5.7, the predicted ionization using a Thomas-Fermi model, a plasma physics standard for dense matter, varies depending on the target material. Nitrogen, a higher Z element, has a stronger potential and thus a lower degree of ionization at a given temperature. However, in a plasma this is predicted to have an effect of only about 10% on the overall ionization.

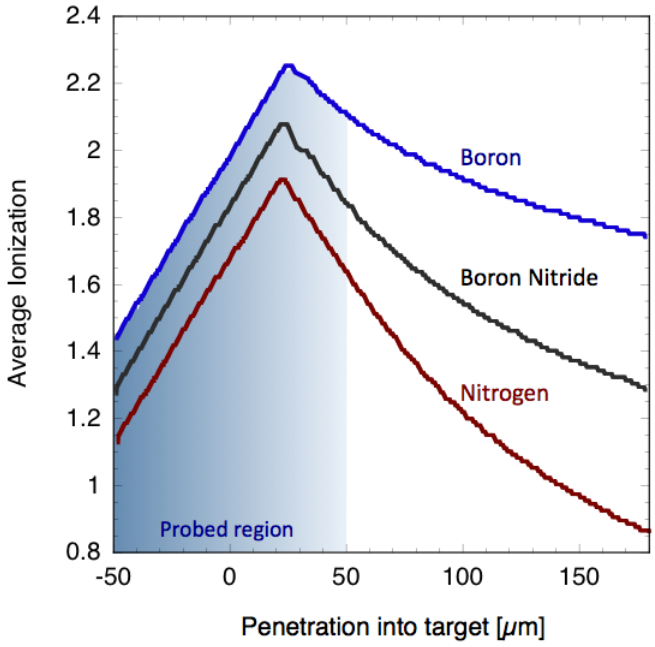

Figure 5.7: LASNEX simulations of ionization in all three relevant target elements. Ionization drops slightly for higher Z material because of the increase in ionization potential.

5.3 Ionization measurements

To determine the ionization of the two targets more accurately, x-ray spectra were recorded at a larger 35° angle for both B and BN targets under ambient and high-temperature conditions. Figure 5.8 shows characteristic observations for each target together with synthetic spectra computed for a range of free electron densities. Because models of ion structure at small k-values and warm, dense conditions vary widely [67], in determining the ionization we evaluate only the inelastic portion of the spectrum, whose spectral position is sensitive to electron density. The elastic portion of the spectrum is fit with a Gaussian the width of the instrument function of the spectrometer; the inelastic portion is broadened with the same function.

Unheated B exhibits no inelastic feature, lacking a significant population of electrons in the conduction band. Under heated conditions, a strong plasmon resonance is observed at a red-shift of 23.8 eV, consistent with an average ionization of Z=3±0.8.

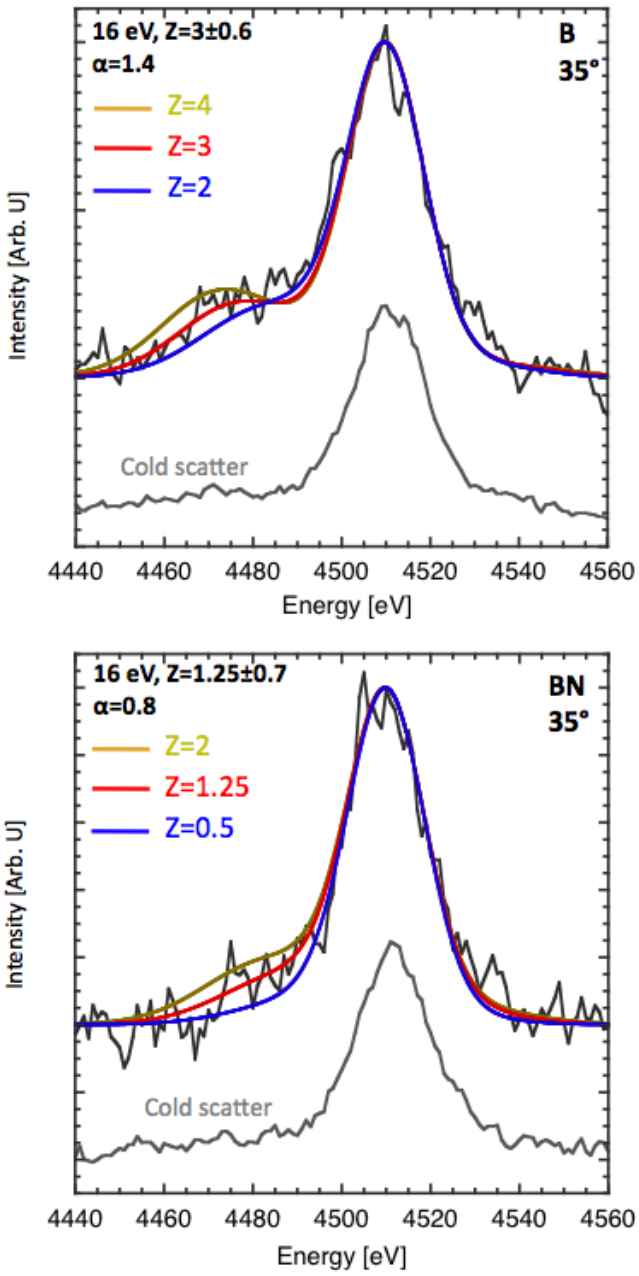

Figure 5.8: X-ray scattering from hot and cold B and BN targets. While a dispersed plasmon is visible in B, very little inelastic signal is apparent in hot BN due to its low ionization.

BN, an insulator, also has a lone elastic peak under ambient conditions. However, at high temperature, we observe a very weak inelastic signal. Fitting of this feature indicates an average ionization of Z=1.3±0.6. In this case the electron density is sufficiently low that the plasma screening length extends beyond the scale lengths probed by our x-ray probe; the scattering parameter becomes α=0.8, and plasmon oscillations are no longer apparent at all. Nevertheless, an upper bound can be put on ionization because of the very narrow width of the Compton feature and low intensity of the inelastic scattering wing. Note that here no significant bound-free signal is observed since the Compton energy in a forward scattering geometry is minimal.

Drastic differences in ionization in samples at similar conditions are unexpected within ideal plasma theory, given the similar ionization potentials in B and N. However, the presence of significant gaps in the BN density of states (DoS) at high temperature can lead to lower electron populations in the conduction band. We performed simulations of the electron structure of B and BN using a finite-temperature extension of the MECCA implementation of the KKR-CPA approach to electron structure calculations [78] and the Purgatorio average-atom plasma code [76]. We determined the average free electron population per ion within these physical picture codes by integrating the Fermi populated DoS at positive eigenvalues. Although there is ambiguity in the definition of ionization in such theoretical treatments, Glenzer et al have shown measured ionization values with x-ray scattering that agree with or exceed those produced with physical picture models [10].

In Figure 5.9, the 16 eV density of states (DoS) is shown for both target materials using two computational approaches. Purgatorio, solving the Dirac equation for a fictional average atom imbedded in a background plasma, accurately treats plasma effects like continuum lowering, but includes no ionic correlation effects. Nevertheless, it accurately predicts an ionization degree of Z=3 in hot boron, seen in the smooth DoS curve. MECCA, predicting a value of Z=2.6, also falls within the error bar of the x-ray scattering measurement. This is not surprising as boron, heated from its semi-metallic ground state, metalizes easily at high temperature.

Boron Nitride, in contrast, has a 6 eV band gap in the ground state. Under heated conditions, Purgatorio predicts an average degree of ionization Z>3, but here MECCA predicts Z=2.1 in calculations that treat the ions in thermal equilibrium with the electrons. For these, the calculated DoS still exhibits significant band gaps at high temperature that inhibit the population of the conduction band. This effect is more pronounced still in calculations using 16 eV electrons in a crystal in the ground-state lattice configuration, where it calculates Z=1.2 in close agreement with measurement.

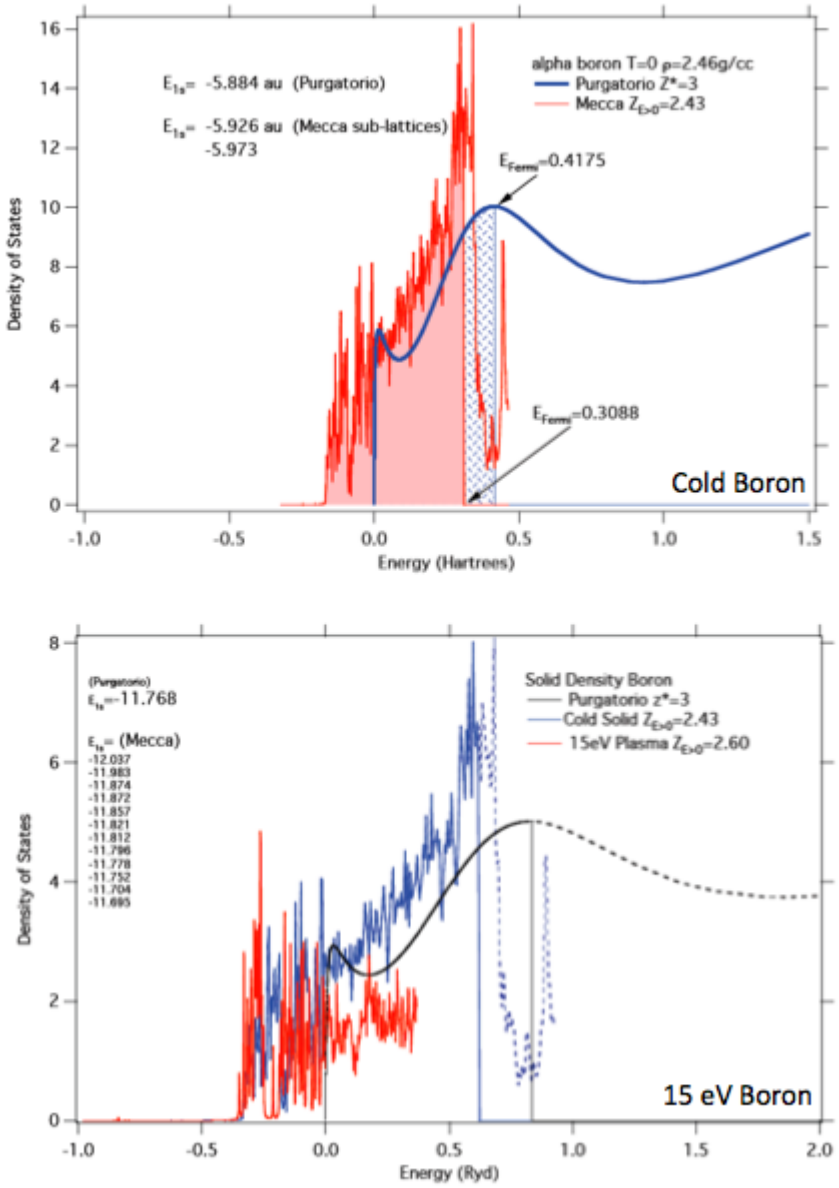

Figure 5.9: Density of states computed for Boron using the plasma code Purgatorio and the condensed matter model MECCA under ambient conditions and at 16 eV. Each calculation produces a similar ionization state within the error bars of our x-ray scattering measurement.

That is, ionizations in agreement with the scattering measurements are produced in simulations that include the ion configuration closest to the ground state. The source of low ionization in this case is the band gap that persists thanks to ion symmetry; at this temperature the Fermi-population of electrons above the gap in the conduction band is much lower than in the case of highly ionized B. This difference suggests that long-range ionic structure still plays a role in BN with electron temperatures far above the melt point.

A temperature in excess of 15 eV is well above the thermal melt point of both targets, approximately 2349 K for B and 3246 K for BN. Thus, the BN targets would be expected to be a disordered liquid in thermal equilibrium. Two obvious explanations exist for why that may not be an accurate picture. If the electron-ion equilibration time is sufficiently slow, then it is possible that the ion lattice is not yet melted. In this case, calculations for a hot electron population of a cold lattice would be an appropriate approximation. There is some evidence for very low electron-phonon coupling in carbon [45], for example, leading to long equilibration times in proton-heated samples [17]. However, these studies were performed at significantly lower temperatures than the present data. The electron-phonon scattering processes that drive equilibration have not been studied at such energy densities.

Completely understanding this system will require more measurements and robust calculations. A central current challenge is that the experiment is at the limit of tractability for MD-DFT schemes because of its relatively high temperature. Because the Fermi distribution function of the electrons spreads out at high temperatures, including many fractionally occupied electron bands requires a great deal of computational power. Nevertheless, calculations are currently being attempted.

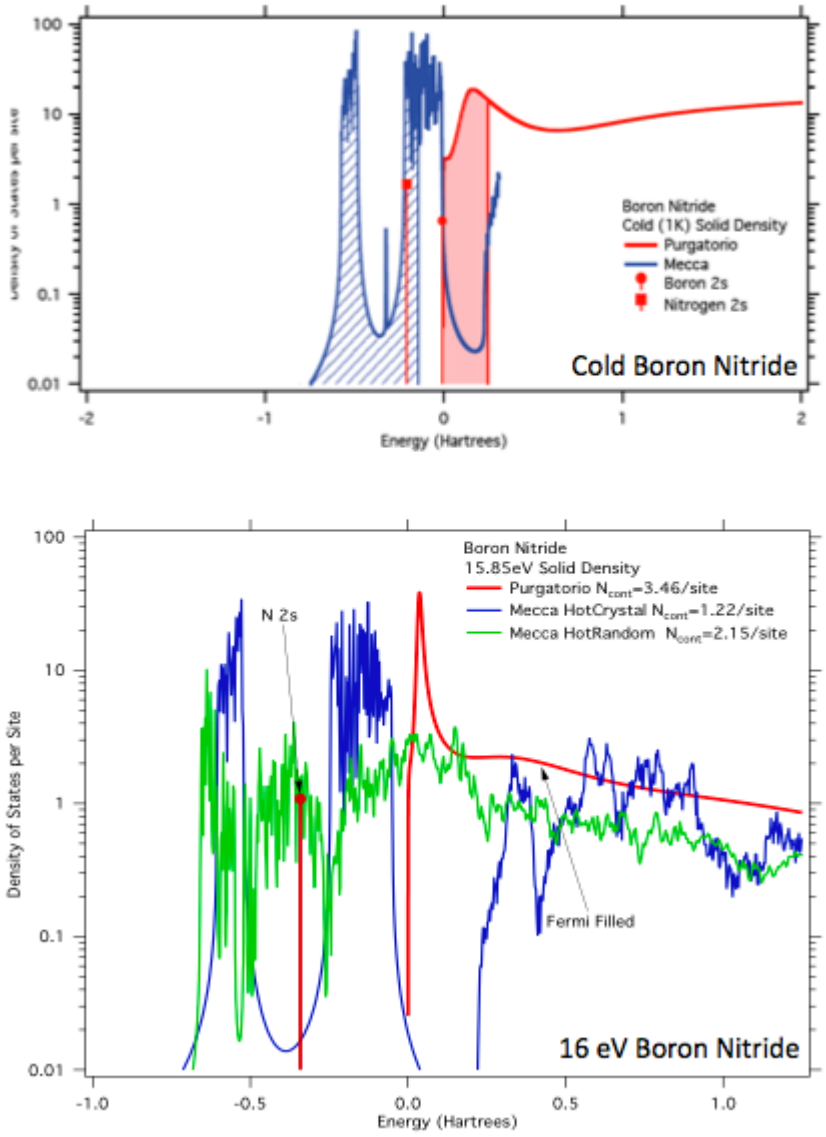

Figure 5.10: Density of states computed for Boron using the plasma code Purgatorio and the condensed matter model MECCA under ambient conditions and at 16 eV. Each calculation produces a similar ionization state within the error bars of our x-ray scattering measurement.

Chapter 6

Conclusion

In this dissertation, spectrally resolved x-ray scattering has been demonstrated for the first time in two important types of systems in the warm, dense matter regime. In shock-compressed hydrogen, a plasmon resonance has been observed at the onset of pressure-induced ionization. The presence of free electrons has been measured using collective scattering at compressions of 3.2; lower compression measurements showing no free electron oscillations suggest that the onset of ionization occurs rather sharply near $\rho/\rho_0 = 3$. By performing simultaneous velocity interferometry, pressure and mass density along the principal Hugoniot were determined independent of scattering models, providing an important additional constraint on hydrodynamic simulations. Additional backscattering measurements confirmed the ionization measurements and were also consistent with density-functional-theoretic simulations of the electron temperature. Calculations using the best models currently available shows very good agreement between measured ionization and predicted molecular dissociation, suggesting that these two processes are very closely linked.

The direct observation of ionization provides a new basis for comparison to theory, which in single-shock experiments has thus far been limited mostly to direct velocity and optical reflectivity measurements. Physical picture calculations like MD-DFT appear to offer the best basis for understanding fractionally ionized hydrogen; however, the challenge of extracting a free electron population from partially delocalized electron wavefunctions remains difficult. The physics of this process are illustrated with preliminary calculations of the dynamic conductivity of deuterium compressed to the conditions measured in Chapter 4 seen in Figure 6.1 using the Kubo-Greenwood approach. The conductivity in these plots peaks between 10 and 15 eV on the horizontal

axis; a true plasma with free electrons would be expected to have a prominent Drude (DC) peak at 0 eV. The lack of such a feature suggests that ionization is fairly modest at these pressures. On the other hand, the AC feature is consistent with the presence of some delocalized electrons playing a role in electrical transport. In short, this is an excellent example of warm, dense matter: the electrons are neither tightly bound or completely free. Since the conductivity of the system is closely related to the electron response function and thus the x-ray scattering spectrum, one direction of ongoing research is simulating x-ray spectra directly with DFT methods to better constrain the conductivity by comparing to a measured scattering signal.

Spectrally resolved x-ray scattering has also been observed for the first time in proton-heated targets. Detailed balance in electron plasma oscillations has been measured and found to agree well with hydrodynamic calculations of proton deposition. The observation of plasmon dispersion in Boron and Boron Nitride heated to similar conditions showed drastic differences in free electron populations. This result, which cannot be explained by available conventional plasma models, has been interpreted as evidence that sufficient long-range ion correlations in 16 eV BN exist to retain band structure several hundred picoseconds after heating. This surprising explanation has been bolstered by electron structure simulations using the KKR formalism extended to high temperature materials, which show a persistent band gap in BN that continues to frustrate ionization at high temperature.

Both experiments probe matter at the threshold of ionization. This presents a challenge to simulation not only because it requires a heavy computational load but also because it is difficult to even define average ionization in this regime. Nevertheless, advances in simulation capability in this regime will greatly improve on current understanding of the behavior of WDM. A central feature of D_2 at moderate compression is pressure-induced molecular dissociation. The measurements shown in Chapter 4 suggest that dissociation and ionization are closely related, nearly simultaneous events. A clearer theoretical understanding of these processes will improve equation of state models in the most critical pressure region, guided by clear measurements of both ionization and dissociated fraction.

The measurements in proton-heated matter are challenging to model for a different reason: the temperature is high enough to make a typical band structure calculation extremely expensive, but most higher temperature approximations discard interactions that appear to play an important role in inhibiting ionization. Observing the effects of band structure at these conditions provides both a motivation and a benchmark for pushing simulation capabilities to these temperatures; indeed, collaborators are

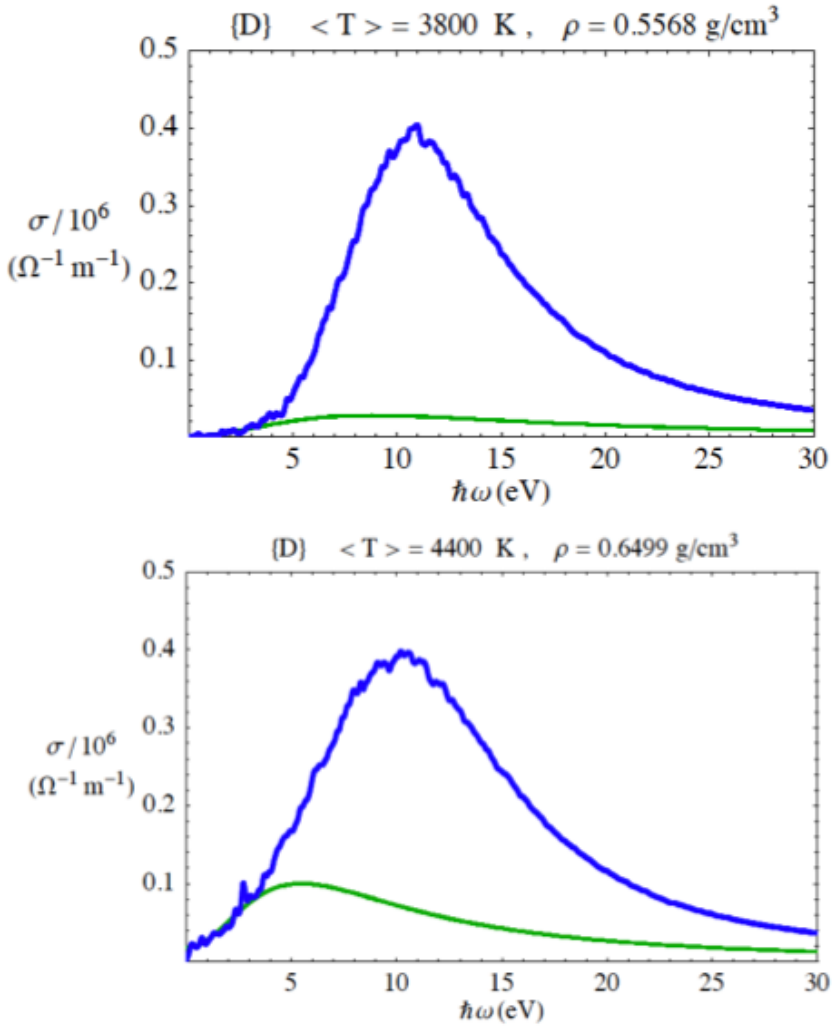

Figure 6.1: Kubo-Greenwood calculations of dynamic conductivities for two values of compression along the principal deuterium Hugoniot showing partially delocalized electron behavior. Courtesy M. Desjarlais.

currently working on molecular dynamics calculations of the conditions measured in Chapter 5 to compare to both these measurements and calculations using other methods. This progress will help to answer open questions about electron equilibration and lattice dynamics and more generally about the structure of electrons and ions in warm material.

These experiments can be improved and extended in several ways. Shock compression studies are inherently limited at the Janus laser, where peak drive pressure is about 4×10^{13} W/cm^2 over a few nanoseconds, insufficient pressure to fully ionize deuterium. The next logical step would be to field a similar forward scattering experiment at a higher energy facility like the Omega laser at LLE, where intensities an order of magnitude higher and sustained pulse lengths are available. X-ray backscattering from cryogenic deuterium was demonstrated at Omega contemporaneously with the work presented in this dissertation [105], but at a proof-of-principle level. Tracking plasmon oscillations as a function of drive pressure from the onset of ionization to fully stripped and dissociated would provide a robust picture of ionization over the full range of most theoretical uncertainty. However, it could be bolstered by simultaneous backscattering, VISAR and even pyrometry measurements. Combined, these diagnostics would provide accurate knowledge of plasma temperature and mass density in addition to ionization state. Such a study would determine not just the Hugoniot variables but off-Hugoniot values like ionization and temperature across a wide range of pressures, providing a basis to constrain theory at the most uncertain points.

The proton heating experiments raise questions about material specific band structure at high temperature. It would be instructive to perform similar measurements in a series of materials of varying ground state band gaps, tracking changing ionization with x-ray scattering. By varying the intensity of the proton drive beam, one could map out possible temperature threshold effects.

However, perhaps the most valuable extension of the x-ray scattering diagnostic is not using a laser-pumped x-ray source at all. Fourth-generation x-ray sources like Linac Coherent Light Source (LCLS) at Stanford offer the potential of higher resolution, higher signal-to-noise experiments at the Materials under Extreme Conditions (MEC) end station. The LCLS pulse offers 10^{12} photons in a pulse of nominally 100 fs duration. It is also highly directional without the broadband noise associated with laser-plasma interactions. With better temporal and energy resolution, it will be possible to powerfully extend the experiments presented here. In particular, deuterium has a molecular resonance in addition to the electron-plasmon one, visible in synchrotron spectra. A sufficiently high-resolution experiment should thus be able to track both

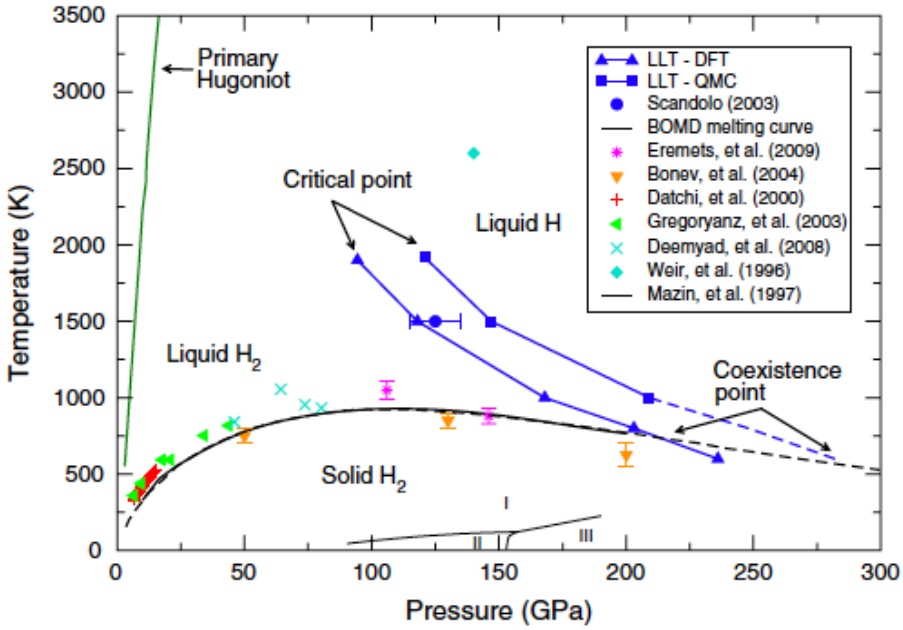

Figure 6.2: The phase diagram of hydrogen from [36] showing experiments and calculations at high pressure. A structural liquid-liquid phase transition could be observed using a very similar scattering technique to the one demonstrated in Chapter 4.

the onset of ionization through the appearance and shift of plasmon and of dissociation through the disappearance and shift of the molecular resonance. More interesting still is the possibility of performing off-Hugoniot measurements, something that can be achieved with drive laser pulse shaping or precompression with diamond anvil cells [106]. This could be a powerful platform for exploring hypothesized phase transitions in hydrogen, particularly the liquid-liquid transition above 100 GPa, shown in Figure 6.2. In particular, by performing multiple angle scattering measurements, it is possible to directly measure the ion correlation functions, providing compelling evidence of the presence or lack of a structural phase transition.

The flexibility and power of a free-electron laser would also allow precise timing control over an isochoric heating experiment. Precise timing increments could be measured from sub-picosecond to hundreds of picoseconds after heating. This would make it possible to completely map out the heating and dynamics of the sample as a function of time. Moreover, both Bragg diffraction and multiple angles of inelastic scattering

could be measured from the sample; this would make it possible to directly observe changes in ion configuration and correlate those changes to free electron population. Combined, this information could provide a very robust basic for comparison with theory. Indeed, while spectrally resolved x-ray scattering is a rather new diagnostic tool in dynamically heated targets, ever improving x-ray sources make it a very attractive method in the ongoing effort to understand material properties under extreme conditions.

Bibliography

[1] A. Ng, Warm dense matter and idealized slab plasma. *29th IEEE International Conference on Plasma Science* (2002).

[2] G. Chabrier *et al.*, Dense plasmas in astrophysics: from giant planets to neutron stars. *J. Phys. A: Math. Gen.* **39**, 4411 (2006).

[3] S. H. Glenzer *et al.*, X-ray Thomson scattering in high energy density plasmas. *Rev. Mod. Phys.* **81**, 1625 (2009).

[4] A. H. Compton, A Quantum Theory of the Scattering of X-rays by Light Elements. *Phys Rev.* **21**, 483 (1923).

[5] J. W. M. Du Mond, Compton Modified Line Structure and its Relation to the Electron Theory of Solid Bodies. *Phys Rev.* **33**, 643 (1929).

[6] W. Schulke, *Electron Dynamics by Inelastic X-ray Scattering* (Oxford University Press, USA, 2007).

[7] Center for X-ray Optics and Advanced Light Source, Lawrence Berkeley National Laboratory, *X-ray Data Booklet* (http://cxro.lbl.gov/x-ray-data-booklet, 2009).

[8] O. L. Landen *et al.*, Dense matter characterization by x-ray Thomson scattering. *J. Quant. Spec. Rad.* **71**, 465 (2001).

[9] DOE Office of Science and NNSA, *Basic Research Needs for High Energy Density Laboratory Physics.* (2010).

[10] S. H. Glenzer *et al.*, Demonstration of Spectrally Resolved X-ray Scattering in Dense Plasmas. *Phys. Rev. Lett.* **90**, 175002 (2003).

[11] H. J. Lee *et al.*, X-Ray Thomson-Scattering Measurements of Density and Temperature in Shock-Compressed Beryllium. *Phys. Rev. Lett.* **102**, 115001 (2009).

[12] O. L. Landen *et al.*, Dense matter characterization by x-ray Thomson scattering. *J. Quant. Spec. Rad.* **71**, 465 (2001).

[13] S. H. Glenzer *et al.*, Observations of plasmons in warm dense matter. *Phys. Rev. Lett.* **98**, 056002 (2007).

[14] A. L. Kritcher *et al.*, Ultrafast X-ray Thomson Scattering of Shock-Compressed Matter. *Science* **322**, 69 (2008).

[15] P. Neumayer *et al.*, Plasmons in Strongly Coupled Shock-Compressed Matter. *Phys. Rev. Lett.* **105**, 075003 (2010).

[16] A. Pelka *et al.*, Ultrafast Melting of Carbon Induced by Intense Proton Beams. *Phys. Rev. Lett.* **105**, 265701 (2010).

[17] T. White *et al.*, Observation of inhibited electron-ion coupling in strongly heated graphite. *submitted to Science* (2012).

[18] E. Wigner and H. B. Huntington, On the Possibility of a Metallic Modification of Hydrogen. *J. Chem. Phys.* **3**, 764 (1935).

[19] N. Nettelman *et al.*, Ab initio equation of state data for hydrogen, helium, and water and the internal structure of Jupiter. *Astrophys. J.* **683**, 1217 (2008).

[20] C. S. Zha *et al.*, Synchrotron Infrared Measurements of Dense Hydrogen to 360 GPa. *Phys. Rev. Lett.* **108**, 146402 (2012).

[21] P. Loubeyre *et al.*, Optical studies of solid hydrogen to 320 GPa and evidence for black hydrogen. *Nature* **416**, 613 (2002).

[22] M. I. Eremets and I. A. Troyan, Conductive dense hydrogen. *Nature Materials* **10**, 927 (2011).

[23] W. J. Nellis *et al.*, Metallization and Electrical Conductivity of Hydrogen in Jupiter. *Science* **273**, 936 (1996).

[24] P. M. Celliers *et al.*, Accurate measurement of laser-driven shock trajectories with velocity interferometry. *Appl. Phys. Lett.* **73**, 1320 (1998).

[25] G. W. Collins *et al.*, Measurements of the equation of state of deuterium at the fluid insulator-metal transition. *Science* **84**, 5564 (2000).

[26] P. M. Celliers *et al.*, Shock-induced transformation of liquid deuterium into a metallic fluid. *Phys. Rev. Lett.* **281**, 1178 (1998).

[27] M. D. Knudson *et al.*, Equation of State Measurements in Liquid Deuterium to 70 GPa. *Phys. Rev. Lett.* **87**, 225501 (2001).

[28] M. D. Knudson *et al.*, Principal Hugoniot, reverberating wave, and mechanical reshock measurements of liquid deuterium to 400 GPa using plate impact techniques. *Phys. Rev. B.* **69**, 144209 (2004).

[29] D. G. Hicks *et al.*, Laser-driven single shock compression of fluid deuterium from 45 to 220 GPa. *Phys. Rev. B.* **79**, 014112 (2009).

[30] H. B. Niemann *et al.*, The Galileo Probe Mass Spectrometer: Composition of Jupiter's Atmosphere. *Science* **272**, 846 (1996).

[31] B. Holst *et al.*, Equation of State for Dense Hydrogen and Plasma Phase Transition. *Contrib. Plasma. Phys.* **47**, 368 (2007).

[32] M. Ross, Linear-mixing model for shock-compressed liquid deuterium. *Phys. Rev. B.* **58**, 669 (1998).

[33] G. Kerley, Sandia National Laboratory, Technical Report No. SAND2003-3613 (2003).

[34] M. A. Morales *et al.*, Equation of state of metallic hydrogen from coupled electron-ion Monte Carlo simulations. *Phys. Rev. E.* **81**, 021202 (2010).

[35] B. Holst *et al.*, Thermophysical properties of warm dense hydrogen using quantum molecular dynamics simulations. *Phys. Rev. B.* **77**, 184201 (2008).

[36] M. A. Morales *et al.*, Evidence for a first-order liquid-liquid transition in high-pressure hydrogen from ab initio simulations. *Proc. Nat. Acad. Science* **107**, 12799 (2010).

[37] R. A. Snavely *et al.*, Intense high-energy proton beams from petawatt-laser irradiation of solids. *Phys. Rev. Lett.* **85**, 2945 (2000).

[38] T. Bartal *et al.*, Focusing of short-pulse high-intensity laser-accelerated proton beams. *Nature Physics* **8**, 139 (2012).

[39] J. Fuchs *et al.*, Laser-driven proton scaling laws and new paths towards energy increase. *Nature Physics* **2**, 48 (2006).

[40] P. K. Patel *et al.*, Isochoric Heating of Solid-Density Matter with an Ultrafast Proton Beam. *Phys. Rev. Lett.* **91**, 125004 (2003).

[41] T. Ao *et al.*, Optical properties in nonequilibrium phase transitions. *Phys. Rev. Lett.* **96**, 055001 (2006).

[42] B. I. Cho *et al.*, Electronic Structure of Warm Dense Copper Studied by Ultrafast X-Ray Absorption Spectroscopy. *Phys. Rev. Lett.* **106**, 167601 (2011).

[43] K. Widmann *et al.*, Single-state measurement of electrical conductivity of warm dense gold. *Phys. Rev. Lett.* **92**, 125002 (2004).

[44] Y. Ping *et al.*, Broadband Dielectric Function of NonequilibriumWarm Dense Gold. *Phys. Rev. Lett.* **96**, 255003 (2006).

[45] C. S. Leem *et al.*, Effect of Linear Density of States on the Quasiparticle Dynamics and Small Electron-Phonon Coupling in Graphite. *Phys. Rev. Lett.* **100**, 016802 (2008).

[46] D. Attwood, *Soft X-rays and Extreme Ultraviolet Radiation: Principles and Applications* (Cambridge University Press, 2007).

[47] D. Bohm and E. P. Gross, Theory of plasma oscillations. *Phys. Rev.* **75**, 1851 (1949).

[48] R. Thiele *et al.*, Plasmon resonance in warm dense matter. *Phys. Rev. E.* **78**, 026411 (2008).

[49] V. L. Ginsburg, *Propagation of electromagnetic waves in plasma* (Gordon and Breach, New York, 1961).

[50] S. C. Wilks and W. L. Kruer. Absorption of ultrashort, ultra-intense laser light by solids and overdense plasmas. *IEEE. J. Quant. Elec.* **33**, 1954 (1997).

[51] J. Lindl *et al.*, The physics basis for ignition using indirect-drive targets on the National Ignition Facility. *Phys. Plasmas* **11**, 339 (2004).

[52] P. Gibbon and A. R. Bell, Collisionless absorption in sharp-edged plasmas. *Phys. Rev. Lett.* **68**, 1535 (1992).

[53] W. Kruer *et al.*, J × B heating by very intense laser light. *Phys. Fluids* **28**, 430 (1985).

[54] K. G. Estabrook *et al.*, Two-dimensional relativistic simulations of resonance absorption. *Phys. Fluids* **18**, 1151 (1975).

[55] J. Chihara, Difference in x-ray scattering between metallic and non-metallic liquids due to conduction electrons. *J. Phys. F: Met. Phys.* **17**, 295 (1987).

[56] J. Chihara, Interaction of photons with plasmas and liquid metals - photoabsorption and scattering. *J. Phys. Cond. Mat* **12**, 231 (2000).

[57] G. Gregori *et al.*, Theoretical Model of x-ray scattering as a dense matter probe. *Phys. Rev. E.* **90**, 175002 (2003).

[58] D. Pines and P. Nozieres, *The Theory of Quantum Liquids* (Benjamin, New York, 1966).

[59] G. Gregori *et al.*, Derivation of the static structure factor in strongly coupled non-equilibrium plasmas for X-ray scattering studies. *High. En. Den. Phys.* **3**, 99 (2007).

[60] N. D. Mermin, Lindhard Dielectric Function in the Relaxation-Time Approximation. *Phys. Rev. B.* **1**, 2362 (1970).

[61] C. Fortmann *et al.*, Influence of local-field corrections on Thomson scattering in collision-dominated two-component plasmas. *Phys. Rev. E.* **81**, 026405 (2010).

[62] T. Döppner *et al.*, Temperature measurement through detailed balance in x-ray Thomson scattering. *High En. Den. Phys.* **5**, 182 (2009).

[63] K. Wunsch *et al.*, Ion structure in warm dense matter: Benchmarking solutions of hypernetted-chain equations by first-principle simulations. *Phys. Rev. E.* **79**, 010201 (2009).

[64] K. Wunsch *et al.*, Structure of strongly coupled multicomponent plasmas. *Phys. Rev. E.* **77**, 056404 (2008).

[65] H. B. Singh and A. Holz, Structure factor of liquid alkali metals. *Phys. Rev. A* **28**, 1108 (1983).

[66] E. Garcia Saiz *et al.*, Probing warm dense lithium by inelastic x-ray scattering. *Nature Physics* **4**, 940 (2008).

[67] D. O. Gericke *et al.*, Screening of ionic cores in partially ionized plasmas within linear response. *Phys. Rev. E.* **81**, 065401 (2010).

[68] P. Eisenberger and P. M. Platzman, Compton scattering of x-rays from bound electrons. *Phys. Rev. A.* **2**, 415 (1970).

[69] J. C. Stewart and K. D. Pyatt, Lowering of ionization potentials in plasmas. *Astrophys. J.* **144**, 1203 (1966).

[70] D. Salzmann *et al.*, Comparison between average-atom and detailed-configuration-type calculations of the photoionization cross section of hot and dense aluminum plasmas. *Phys. Rev. A.* **32**, 3627 (1985).

[71] S. Sahoo *et al.*, Compton scatter profiles for warm dense matter. *Phys. Rev. E.* **77**, 046402 (2008).

[72] B. A. Mattern *et al.*, Real-space Green's function calculations of Compton profiles. *Phys. Rev. B.* **85**, 115135 (2012).

[73] R. P. Drake, *High-Energy-Density Physics: Fundamentals, Inertial Fusion, and Experimental Astrophysics* (Springer-Verlag, Berlin Heidelberg, 2006).

Soft X-rays and Extreme Ultraviolet Radiation: Principles and Applications (Cambridge University Press, 2007).

[74] NIST PSTAR Database. (http://physics.nist.gov/PhysRefData/Star/Text/PSTAR.html, 2005).

[75] G. B. Zimmerman and W. L. Kruer, The LASNEX simulation code. *Comm. Plasma Phys. Cont. Fus.* **2**, 51 (1975).

[76] B. Wilson, *et al.*, Purgatorio - a new implementation of the Inferno algorithm. *J. Quant. Spec. Rad. Trans.* **99**, 658 (2006).

[77] W. R. Johnson *et al.*, Optical properties of plasmas based on an average-atom model. *J. Quant. Spect. Rad.* **99**, 327 (2006).

[78] D. D. Johnson *et al.*, A Fast Method for Calculating the Electronic Structure of Random Alloys. *Phys. Rev. B.* **30**, 5508 (1984).

[79] S. I. Zabinsky *et al.*, Multiple-scattering calculations of x-ray absorption spectra. *Rev. Sci. Inst.* **52**, 2995 (1995).

[80] W. Kohn and L. J. Sham, Self-Consistent Equations Including Exchange and Correlation Effects. *Phys. Rev.* **140**, A1133 (1965).

[81] N. D. Mermin, Thermal properties of the inhomogeneous electron gas. *Phys. Rev.* **137**, A1441 (1965).

[82] R. Car and M. Parrinello, Unified approach for molecular dynamics and density-functional-theory. *Phys. Rev. Lett.* **55**, 2471 (1985).

[83] R. Kubo *et al.*, Statistical-mechanical theory of irreversible processes. I. General theory and simple applications to magnetic and conduction problems. *J. Phys. Soc. Jpn.* **12**, 570 (1957).

[84] J. A. Greenwood and J. B. P. Williamson, Electrical Conduction in solids. II. Theory of temperature-dependent conductors. *Proc. R. Soc. London* **246**, 13 (1958).

[85] S. M. Dixit *et al.*, Designing fully continuous phase screens for tailoring focal-plane irradiance profiles. *Opt. Lett.* **21**, 1715 (1996).

[86] J. Collier *et al.*, Evaluation of an ultrabroadband highgain amplification technique for chirped pulse amplification facilities. *Appl. Opt.* **38**, 7486 (1999).

[87] H. S. Park *et al.*, High energy Kα radiography using high-intensity, short-pulse lasers. *Phys. Plasmas* **13**, 056309 (2006).

[88] C. Reich *et al.*, Yield optimization and time structure of femtosecond laser plasma k alpha sources. *Phys. Rev. Lett.* **84**, 4846 (2000).

[89] A. Pak *et al.*, X-ray line measurements with high efficiency Bragg crystals. *Rev. Sci. Inst.* **75**, 3747 (2004).

[90] M. S. Del Rio *et al.*, Focusing properties of mosaic crystals. *Proc. SPIE* **3448**, 246 (1998).

[91] G. Ice *et al.*, Mosaic crystal x-ray spectrometer to resolve inelastic background from anomalous scattering experiments. *Nuc. Inst. & Methods* **A291** (1990).

[92] Harvard Center for Astrophysics: Atomic and Molecular Physics Databases. (http://www.cfa.harvard.edu/ampcgi/kelly.pl, 2009).

[93] A.L. Meadowcroft *et al.*, Evaluation of the sensitivity and fading characteristics of an image plate system for x-ray diagnostics. *Rev. Sci. Inst.* **79**, 113102 (2008).

[94] H. Chen *et al.*, An imaging proton spectrometer for short-pulse laser plasma experiments. *Rev. Sci. Inst.* **81**, 10D314 (2010).

[95] L. M. Barker and R. E. Hollenbach, Laser interferometer for measuring high velocities of any reflecting surface. *J. Appl. Phys.* **43**, 4669 (1972).

[96] P. M. Celliers *et al.*, Line-imaging velocimeter for shock diagnostics at the OMEGA laser facility. *Rev. Sci. Inst.* **75**, 4916 (2004).

[97] D. K. Spaulding *et al.*, New optical diagnostics for equation of state experiments on the Janus laser. *AIP Conf. Proc.* **955**, 1071 (2007).

[98] W. Lorenzen *et al.*, First-order liquid-liquid phase transition in dense hydrogen. *Phys. Rev. B.* **82**, 195107 (2010).

[99] M. K. Urry *et al.*, X-ray probe development for collective scattering measurements in dense plasmas. *J. Quant. Spec. Rad.* **99**, 636 (2006).

[100] R. M. More *et al.*, A new quotidian equation of state for hot dense matter. *Phys. Fluids* **31**, 3059 (1988).

[101] M. M. Marinak *et al.*, Three-dimensional simulations of Nova high growth factor capsule implosion experiments. *Phys. Plasmas* **3**, 2070 (1996).

[102] M. P. Desjarlais, Density-funcitonal calculations of the liquid deuterium Hugoniot, reshock, and reverberation timing. *Phys. Rev. B.* **68**, 064204 (2003).

[103] A. Kritcher *et al.*. K-alpha conversion efficiency measurements for X-ray scattering in inertial confinement fusion plasmas. *High. En. Den. Phys.* **3**, 156 (2007).

[104] F. Nurnberg *et al.*, Radiochromic film imaging spectroscopy of laser-accelerated proton beams. *Rev. Sci. Inst.* **80**, 03330 (2009).

[105] S. P. Regan *et al.*, Inelastic X-Ray Scattering from Shocked Liquid Deuterium. *submitted to Phys. Rev. Lett.* (2012).

[106] P. Loubeyre *et al.*, Coupling static and dynamic compressions: first measurements in dense hydrogen. *High. Press. Res.* **24**, 25 (2004).